

QUANTUM THEORY OF CONDITIONAL PHONON STATES IN A
DUAL-PUMPED RAMAN OPTICAL FREQUENCY COMB

by

ERIN MONDLOCH

A DISSERTATION

Presented to the Department of Physics
and the Graduate School of the University of Oregon
in partial fulfillment of the requirements
for the degree of
Doctor of Philosophy

March 2017

DISSERTATION APPROVAL PAGE

Student: Erin Mondloch

Title: Quantum Theory of Conditional Phonon States in a Dual-Pumped Raman Optical Frequency Comb

This dissertation has been accepted and approved in partial fulfillment of the requirements for the Doctor of Philosophy degree in the Department of Physics by:

Daniel Steck	Chair
Michael Raymer	Advisor
Raghuv eer Parthasarathy	Core Member
Andrew H. Marcus	Institutional Representative

and

Scott L. Pratt	Dean of the Graduate School
----------------	-----------------------------

Original approval signatures are on file with the University of Oregon Graduate School.

Degree awarded March 2017

© 2017 Erin Mondloch

DISSERTATION ABSTRACT

Erin Mondloch

Doctor of Philosophy

Department of Physics

March 2017

Title: Quantum Theory of Conditional Phonon States in a Dual-Pumped Raman Optical Frequency Comb

In this work, we theoretically and numerically investigate nonclassical phonon states created in the collective vibration of a Raman medium by the generation of a dual-pumped Raman optical frequency comb in an optical cavity. This frequency comb is generated by cascaded Raman scattering driven by two phase-locked pump lasers that are separated in frequency by three times the Raman phonon frequency. We characterize the variety of conditioned phonon states that are created when the number of photons in all optical frequency modes except the pump modes are measured. Almost all of these conditioned phonon states are extremely well approximated as three-phonon-squeezed states or Schrödinger-cat states, depending on the outcomes of the photon number measurements. We show how the combinations of first-, second-, and third-order Raman scattering that correspond to each set of measured photon numbers determine the fidelity of the conditioned phonon state with model three-phonon-squeezed states and Schrödinger-cat states. All of the conditioned phonon states demonstrate preferential growth of the phonon mode along three directions in phase space. That is, there are three preferred phase values that the phonon state takes on as a result of Raman scattering. We show that the combination of Raman processes that produces a given set of measured photon numbers always

produces phonons in multiples of three. In the quantum number-state representation, these multiples of three are responsible for the threefold phase-space symmetry seen in the conditioned phonon states.

With a semiclassical model, we show how this three-phase preference can also be understood in light of phase correlations that are known to spontaneously arise in single-pumped Raman frequency combs. Additionally, our semiclassical model predicts that the optical modes also grow preferentially along three phases, suggesting that the dual-pumped Raman optical frequency comb is partially phase-stabilized.

CURRICULUM VITAE

NAME OF AUTHOR: Erin Mondloch

GRADUATE AND UNDERGRADUATE SCHOOLS ATTENDED:

University of Oregon, Eugene, Oregon
University of Montana, Missoula, Montana

DEGREES AWARDED:

Doctor of Philosophy, Physics, 2017, University of Oregon
Master of Science, Physics, 2009, University of Oregon
Bachelor of Arts, Physics and Applied Mathematics, 2008, University of Montana

AREAS OF SPECIAL INTEREST:

Numerical Modeling
Quantum Optics

PROFESSIONAL EXPERIENCE:

Graduate Research Assistant, University of Oregon, 2008-2017
Graduate Teaching Assistant, University of Oregon, 2008

GRANTS, AWARDS AND HONORS:

Outstanding Graduating Senior Award, Department of Physics and Astronomy
and Department of Mathematical Sciences, University of Montana, 2008

PUBLICATIONS:

- K. E. Lynch-Klarup, E. Mondloch, M. G. Raymer, D. Arrestier, F. Gerome, and F. Benabid, "Supercritical xenon-filled hollow-core photonic bandgap fiber," *Opt. Express* 21, 13726-13732 (2013)
- K. E. Lynch-Klarup, E. Mondloch, M. G. Raymer, F. Benabid, F. Gerome, and D. Arrestier, "Supercritical-Xenon-Filled Photonic Crystal Fiber as a Raman-Free Nonlinear Optical Medium," in *Frontiers in Optics 2012/Laser Science XXVIII*, (Optical Society of America, 2012), paper FM4I.2.
- E. Mondloch, M. G. Raymer, and F. Benabid, "Spontaneous Phase Locking in Dual-Pumped Raman Frequency Comb Generation," in *Frontiers in Optics 2012/Laser Science XXVIII*, (Optical Society of America, 2012), paper FM4I.3.
- C. Wu, E. Mondloch, M. G. Raymer, Y. Wang, F. Couny, and F. Benabid, "Spontaneous Phase Correlations in Raman Optical Frequency Comb Generation," in *Frontiers in Optics 2010/Laser Science XXVI*, (Optical Society of America, 2010), paper FTuL2.
- C. Wu, E. Mondloch, M. G. Raymer, Y. Wang, F. Couny, and F. Benabid, "Spontaneous Phase Anti-correlations in Raman Optical Frequency Comb Generation," in *Conference on Lasers and Electro-Optics 2010*, (Optical Society of America, 2010), paper QTuA5.

ACKNOWLEDGEMENTS

I thank Steven van Enk and Jeff Cina for sharing their crucial insight on this research. Their observations pointed this project in its most interesting directions. I also thank Dan Steck, Craig Rasmussen, Erik Keever, and Jonathan Mackrory for suggestions on approaching the numerical challenges of this work. My labmates Chunbai Wu, Dash Vitullo, Roger Smith, Kyle Klarup, and Dileep Reddy have provided useful and interesting input over the evolution of this project, and I thank them as well.

I am grateful to Raghu Parthasarathy, Andy Marcus, and Dan Steck for serving on my dissertation committee. Their advice and encouragement played a significant role in the completion of this work. I especially thank Michael Raymer, my advisor, for his mentorship and support. I am fortunate to have learned so much from him about quantum optics and scientific research, and I am very thankful for his kindness and generosity as an advisor.

TABLE OF CONTENTS

Chapter	Page
I. INTRODUCTION	1
II. GENERALIZED SQUEEZED STATES AND SCHRÖDINGER-CAT STATES	11
2.1. Fock states	11
2.2. Squeezed vacuum states	13
2.3. Generalized squeezed states	17
2.4. Schrödinger cat states	18
2.5. Fidelity between kitten states and squeezed states	23
III. QUANTUM THEORY OF CONDITIONED PHONON STATES	28
3.1. Description of the dual-pumped Raman frequency comb	28
3.2. Time evolution from the vacuum state	34
3.3. Conditioning on photon number measurements	37
3.4. Characterizing the conditioned phonon states	43
3.5. Effects of varied pump amplitudes	67
IV. SEMICLASSICAL THEORY	79
4.1. Semiclassical Maxwell-Bloch equations	79
4.2. Semiclassical results	83
4.3. Interpretation in context of spontaneous phase correlations	85
V. CONCLUSION	89
APPENDICES	
A. WIGNER FUNCTION DERIVATION	93
A.1. Complex amplitudes C_N	94
A.2. Real amplitudes $C_N = C_N^*$	96

Chapter	Page
B. PROOFS OF CONDITIONED STATE SYMMETRY	99
B.1. Rotational invariance of Hamiltonian and state	99
B.2. Invariance of conditioned phonon states	100
B.3. Phase-space symmetry of conditioned phonon states	103
C. NUMERICAL METHODS	105
C.1. Numerical methods: quantum theory	105
C.2. Numerical methods: semiclassical theory	107
REFERENCES CITED	109

LIST OF FIGURES

Figure	Page
1.1. Energy-level diagram of a Raman optical frequency comb produced by one pump laser	3
1.2. Energy-level diagram of a Raman optical frequency comb produced by two phase-locked pump lasers at $j = 0$ and $j = 3$	5
1.3. Histogram representing the vacuum state of the phonon mode in phase space	7
1.4. Histogram representing the phase-space distribution of the phonon mode after comb generation	8
2.1. Example Fock state Wigner distributions	13
2.2. Vacuum state Wigner distributions	14
2.3. Wigner distribution of the squeezed vacuum state	15
2.4. Wigner distribution of the squeezed single-phonon Fock state	16
2.5. Wigner distribution of the three-phonon-squeezed vacuum state	19
2.6. Wigner distribution of the three-phonon-squeezed single-phonon Fock state	20
2.7. Wigner distribution of the two-component cat state	22
2.8. Wigner distribution of the three-component cat state	23
2.9. Wigner distribution of the three-component cat state with $\alpha = 1$, $\alpha = 2$, and $\alpha = 3$	24
3.1. Dual-pumped Raman optical frequency comb spectrum	29
3.2. Photon- and phonon-number probability distributions for dual-pumped Raman comb	35
3.3. Wigner distribution for the phonon mode of the dual-pumped Raman comb with photon modes traced out	36
3.4. Illustration of first-, second-, and third-order scattering	40

Figure	Page
3.5. Optimal cat-state fidelity of all conditioned phonon states	48
3.6. Optimal squeezed-state fidelity of all conditioned phonon states	49
3.7. Optimal squeezed-state fidelity vs optimal cat-state fidelity of all 6558 conditioned phonon states	50
3.8. Optimal cat-state amplitude and squeezing gain for states that have high amplitude with both cat and squeezed states	51
3.9. Optimal cat-state amplitude of conditioned phonon states having high fidelity with both cat states and squeezed states	52
3.10. Optimal squeezed-state gain of conditioned phonon states having high fidelity with both cat states and squeezed states	53
3.11. Optimal cat-state amplitude of conditioned phonon states having high fidelity with cat states only	54
3.12. Optimal squeezed-state gain of conditioned phonon states having high fidelity with squeezed states only	55
3.13. Maximal cat-state fidelity and squeezed-state fidelity for conditioned phonon states that do not have at least 0.99 fidelity with either type of state	56
3.14. Dependence of cat-state fidelity and squeezed-state fidelity on total photon number and red-anti-Stokes photon number for intermediate conditioned phonon states where $\Delta_{SAS} = 3$	57
3.15. Ratio between second and first number state amplitudes in the three varieties of three-component cat states	61
3.16. Wigner distributions for some example conditioned phonon states	65
3.17. Canonical phase probability distributions for some example conditioned phonon states	66
3.18. Wigner distribution and canonical phase probability distribution for the conditioned phonon state corresponding to 14 photons in each optical mode	67
3.19. Probability distributions of photon and phonon number at time $t =$ 0.015 with pump amplitudes $A_0 = A_3 = 20$	68
3.20. Probability distributions of photon and phonon number at time $t =$ 0.015 with pump amplitudes $A_0 = 20, A_3 = 60$	69

Figure	Page
3.21. Probability distributions of photon and phonon number at time $t = 0.015$ with pump amplitudes $A_0 = 60, A_3 = 20$	70
3.22. Cat-state fidelity for conditioned phonon states with different pump amplitudes, and cat-state amplitudes for states with high cat-state fidelity	72
3.23. Wigner distribution for the phonon state conditioned on measuring three photons in each optical mode, with $A_0 = A_3 = 60$	73
3.24. Wigner distribution for the phonon state conditioned on measuring three photons in each optical mode, with $A_0 = A_3 = 20$	73
3.25. Wigner distribution for the phonon state conditioned on measuring three photons in each optical mode, with $A_0 = 20, A_3 = 60$	74
3.26. Wigner distribution for the phonon state conditioned on measuring three photons in each optical mode, with $A_0 = 60, A_3 = 20$	74
3.27. Wigner distributions for an arbitrary subset of conditioned phonon states (part 1)	75
3.28. Wigner distributions for an arbitrary subset of conditioned phonon states (part 2)	76
3.29. Wigner distributions for an arbitrary subset of conditioned phonon states (part 3)	77
3.30. Wigner distributions for an arbitrary subset of conditioned phonon states (part 4)	78
4.1. Semiclassical phase-space distributions at $t = 0.015$	84
4.2. Semiclassical phase-space distributions at $t = 0.045$	84
4.3. Semiclassical phase-space distributions at $t = 0.070$	85

LIST OF TABLES

Table	Page
3.1. Probabilities of obtaining phonon cat states from dual-pumped combs with different pump amplitudes	71

CHAPTER I

INTRODUCTION

A practical quantum communication network is likely to encompass the transfer of quantum information from light to matter [1]. A common example is writing information from an incoming photon into an atomic ensemble or mechanical mode for storage, as well as reading that information with an outgoing photon to transmit elsewhere in the network. Making quantum light-matter interactions feasible requires the ability to create and control nonclassical states in material systems, a research goal that has been pursued in systems ranging from optomechanical cavities [2] to room-temperature bulk diamond [3], [4]. In this dissertation, we describe theoretical and numerical research into a technique of creating nonclassical states in the collective vibration of a Raman-active system.

In many ways, phonons can be understood by analogy to photons. A photon is a quantization of electromagnetic modes of light, and a phonon is a quantization of vibrational modes of matter. Like photons, phonons are bosons. This fact entails many similarities between the mathematical descriptions of phonons and photons, such as obeying the same commutation relation. Phonons can be approximated as harmonic oscillators and represented as number states. It must be noted that many specific systems of phonons are not conveniently described in these terms due to large anharmonic corrections, dissipation, and damping [5]. The harmonic oscillator description can, however, be useful for systems in which there are relatively few modes to which the phonons can couple. An important example is the collective excitation of a single vibrational mode of a medium through Raman scattering.

When photons are incident on matter that has vibrational degrees of freedom, it is possible for energy to transfer from the electromagnetic mode to the vibrational mode or vice versa. This inelastic scattering process is known as Raman scattering. In a quantum theory of Raman scattering, the energy transfer is modeled as the annihilation of the original photon and the creation of a phonon and a new photon at a lower frequency, or the annihilation of the original photon and a phonon and the creation of a new photon at a higher frequency. The former process is called Stokes scattering and the latter process anti-Stokes scattering, and the new lower-frequency photon is called a Stokes photon and the new higher-frequency photon is called an anti-Stokes photon. The original photon generally comes from a laser pulse referred to as the pump pulse, and so the original photon may be called the pump photon. The Stokes photon frequency is equal to the pump frequency minus the phonon frequency, and the anti-Stokes photon frequency is equal to the pump frequency plus the phonon frequency. The phonon frequency is determined by the polarizability of the Raman medium. Raman scattering occurs off-resonance from intermediate states, allowing some freedom in choosing the pump frequency.

Subsequently, the Stokes and anti-Stokes photons can scatter from the phonon mode excited in the first interaction to create second-order Stokes or anti-Stokes photons. The second-order Stokes mode frequency is equal to the pump frequency minus twice the phonon frequency, and the second-order anti-Stokes mode frequency is the pump frequency plus twice the phonon frequency. Third-, fourth-, and even higher-order processes are possible. The resulting spectrum is a set of relatively narrow spectral components separated from one another by the phonon frequency [6]. It is, in fact, a frequency comb [7]. An energy-level diagram illustrating the Raman optical frequency comb is shown in Figure 1.1. The excited state $|e\rangle$ and ground state

$|g\rangle$ shown in the diagram are excited and ground states of the collective vibrational mode. The creation of a phonon raises the mode from the ground state to the excited state. Each spectral component in Figure 1.1 is labeled by an integer showing the scattering order, with negative integers indicating Stokes scattering, positive integers indicating anti-Stokes scattering, and 0 indicating the pump. Only a single vibrational degree of freedom is considered for the collective vibrational mode—the one with the highest Raman scattering cross-section¹.

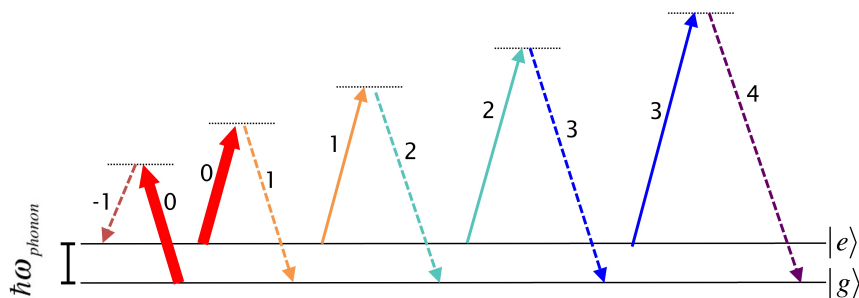


FIGURE 1.1. Energy-level diagram of a Raman optical frequency comb produced by one pump laser. The optical modes are labeled by integers j , the order of the mode. The pump is at the zeroth order, $j = 0$.

At short times, each scattering event is independent and spontaneous, in the sense that it is seeded by the vacuum rather than by real photons. Given enough time and gain, however, the spontaneous initiation of the field can build up into stimulated scattering, in which spontaneously scattered Stokes photons stimulate the scattering of identical photons at that frequency. In the transient (short-pulse), high-gain regime, the initial fluctuations are filtered by the narrow (few GHz) linewidth of the scattering process and the field in each mode is left with a well-defined phase [6], [8], [9]. The phase in each mode is related to the collective phase of the

¹Depending on the polarization of the incoming light, the dominant mode could actually be a rotational mode, but for convenience we refer to the mode as always vibrational.

vibrational excitation created by the scattering, which we will denote as ϕ_{phonon} . In particular, the phase of the j th-order optical mode is approximated by [6], [10]

$$\theta_j \approx \theta_0 + j\phi_{phonon} \quad (1.1)$$

where again, the 0th-order mode is the pump. Despite being initiated by spontaneous scattering from vacuum fluctuations, each mode builds up preferentially with the phase that satisfies the correlation in Equation 1.1, because this condition leads to the fastest growth rate of the stimulated and coherent scattering. Due to the spontaneous initiation, however, the phonon mode phase ϕ_{phonon} is random. From one pump laser shot to the next, the phonon phase takes a new value from a uniform random distribution between 0 and 2π [11], [12]. The phase on one shot is independent from the phase of the previous shot, provided the time between laser shots is much longer than the dephasing time of the medium². As a result, even though the optical mode phases are correlated with each other, the actual value of each of those phases is uniform random on each shot.

Our new idea for creating nonclassical states of the optical and phonon modes is to use not just one pump laser but two. The second laser is added at the k th anti-Stokes frequency and its optical phase is locked to that of the first pump. Because the two pump frequencies are separated by $k\omega_{phonon}$, the frequency comb created by the first pump overlaps with the comb created by the second pump. For example, suppose the second pump frequency is equal to the third-anti-Stokes frequency created by the first pump, as illustrated in Figure 1.2. Then the mode that is populated by first-

²Molecular coherence can persist in the medium for many times the dephasing time of the medium. For instance, in [13], correlations were detected in subsequent Stokes pulses even after nearly nine times the collisional dephasing time of the hydrogen gas medium. In the present discussion we assume that the time between pump pulses is long enough that no coherence persists and each shot of the laser constitutes a completely independent trial.

order Stokes scattering from the second pump is also populated by second-order anti-Stokes scattering from the first pump. Photons from both pumps can spontaneously scatter into their shared optical modes through various combinations of Stokes and anti-Stokes scattering from the same phonon mode.

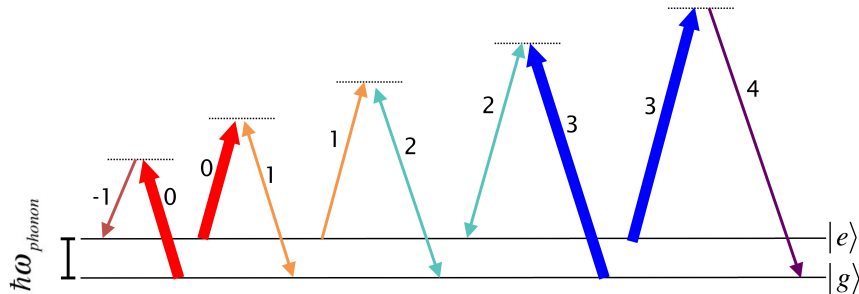


FIGURE 1.2. Energy-level diagram of a Raman optical frequency comb produced by two phase-locked pump lasers at $j = 0$ and $j = 3$.

If the second pump laser is at the frequency of the k th-order anti-Stokes mode, then photons from the second pump will stimulate scattering into the k th mode, and photons that are scattered into that mode from other modes are likely to have the same phase as the second-pump photons. As a result, the phase of the k th mode is still well-defined and fixed by the phase of the second pump laser. Because the other optical modes are produced by scattering from both the first pump in the 0th mode and the second pump in the k th mode, they grow with the phase preference

$$\theta_j \approx \theta_0 + j\phi_{phonon} \quad (1.2)$$

as before, but also with phase preference

$$\theta_j \approx \theta_k + (j - k)\phi_{phonon}. \quad (1.3)$$

Because the phase of each mode is approximately well-defined, the phases expressed by Equations 1.2 and 1.3 must agree within integer multiples³ of 2π . That agreement is possible only for certain values of the phonon phase:

$$\begin{aligned}\theta_0 + j\phi_{phonon} &\approx \theta_k + (j - k)\phi_{phonon} + 2\pi M \\ \rightarrow \phi_{phonon} &\approx \frac{1}{k}(\theta_k - \theta_0) + \frac{2\pi M}{k}\end{aligned}\tag{1.4}$$

That is, when the dual-pumped Raman comb is created by two phase-locked pump lasers at frequencies Ω and $\Omega + k\omega_{phonon}$, the phonon and optical modes grow preferentially at k discrete values evenly distributed between 0 and 2π . When $k = 1$, the two pumps drive the medium at the phonon frequency. This process can be well-described classically and has been used to create phase-stable frequency combs [14], [15], [16].

When $k > 1$, the second pump does not inject any coherence into the medium and does not seed the initial scattering processes. In that case, the phase correlations truly arise spontaneously. Our study is the first to consider the quantum dynamics and statistics of this regime. We find that an entire family of exotic quantum states arises in this case.

The differences in the phonon phase between the single-pumped comb and the dual-pumped comb can be illustrated with semiclassical phase-space diagrams. For this example we choose $k = 3$, that is, the frequency difference between the two pumps is $3\omega_{phonon}$. The axes of these diagrams are the real and imaginary components of the complex amplitude of the phonon mode. The phonon mode after a single shot from

³Thanks to Jeff Cina for pointing out the integer multiples of 2π .

the pump laser(s) can be plotted as a single point on this diagram. The ensemble of amplitudes measured after many independent shots creates a histogram in phase space illustrating the overall phase tendencies of the system. More details on the creation of these phase-space diagrams from the semiclassical Raman comb model are given in Chapter IV.

Figure 1.3 shows, as a reference point, the phonon mode in vacuum. The distribution is a Gaussian centered at the origin with unit variance. This is the initial state of the phonon mode, before the comb generation has begun.

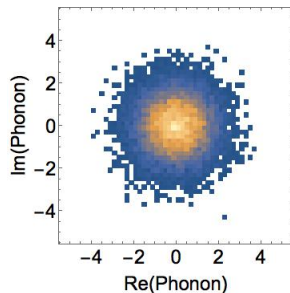


FIGURE 1.3. Histogram representing the vacuum state of the phonon mode in phase space. Brighter colors indicate more data points on a linear scale.

The phase-space distribution of the phonon mode after single-pumped and dual-pumped comb generation is represented by the histograms in Figure 1.4. The single-pumped phonon is a Gaussian distribution centered at the origin. Any phase between 0 and 2π appears equally probable in the single-pumped comb. But in the dual-pumped comb, the phonon mode has developed a three-phase preference. The strongest of the measured phonon amplitudes all lie near $\pi/2$, $\pi/2 + 2\pi/3$, and $\pi/2 - 2\pi/3$, indicating that the phonon mode tends to grow preferentially along these phases. These correspond to the three values of the phonon phase predicted by Equation 1.4 with $k = 3$.

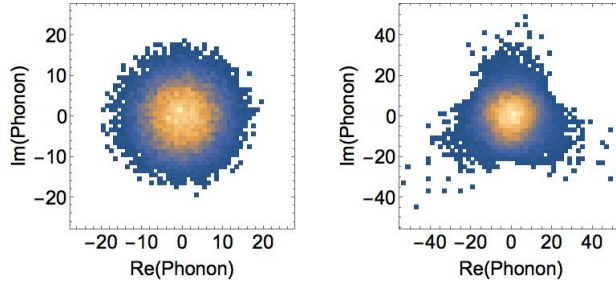


FIGURE 1.4. Histogram representing the phase-space distribution of the phonon mode after comb generation. Left: phonon mode after single-pumped comb generation. Right: phonon mode after dual-pumped comb generation. Brighter colors indicate more data points on a linear scale.

The phonon mode produced by single-pumped Raman comb generation resembles the vacuum state distribution (though the variance is greater). The dual-pumped Raman mode, on the other hand, resembles the phase-space distribution of three-phonon squeezed vacuum. Three-phonon-squeezed vacuum is a superposition of the vacuum state and the three-phonon number state, with smaller contributions from the six-phonon state, the nine-phonon state, and so on. Three-phonon-squeezed vacuum (or more generally, three-boson-squeezed vacuum) is produced by triple-phonon generating processes. This can be understood as a generalized version of the production of ordinary squeezed vacuum during the creation of photon pairs, as in spontaneous parametric downconversion [17], [18]. The similarity between the phase-space distributions of the dual-pumped Raman comb phonon mode and the generalized squeezed vacuum state suggests that at the few-phonon level, the dual-pumped comb produces interesting and potentially useful phonon quantum states. A numerical exploration of the quantum state of the phonon mode in the dual-pumped Raman frequency comb is the subject of this dissertation.

The dissertation is organized as follows:

- In Chapter II, we give an overview of several types of phonon (or photon) quantum states. We begin by introducing the concept of a phonon number state, and build on this concept to explore generalized squeezed states and Schrödinger-cat states, emphasizing that generalized squeezed states and cat states are specific types of number-state superpositions.
- In Chapter III, we describe some of the numerical predictions of a quantum model of the dual-pumped Raman optical frequency comb in an optical cavity. Specifically, we focus on the conditioned phonon states that can be produced by measuring the number of photons in each optical mode. Depending on the photon numbers measured, the conditioned phonon state can be a generalized squeezed state, a Schrödinger-cat state, or an “intermediate” state that does not strongly resemble either type of state. We examine the predictions that can be made about the phonon state based on the measured photon numbers, and offer interpretations of the physics behind them.
- In Chapter IV, we show a numerical toy model of a semiclassical treatment of the dual-pumped comb. While the stability properties of this model are not fully explored, the model does suggest that signatures of the quantum states achieved at low phonon- and photon-numbers could be detectable at higher numbers, and that information may be transferred from the phonon state to the optical modes. The role of the phonon state in partially phase-locking the Raman frequency comb spectral components is also explored.
- In Chapter V, we summarize the dissertation’s main results and conclude by briefly discussing prospects for future work.

- Appendices A and B contain lengthy proofs of results used in Chapters II and III.
- Appendix C contains details on the numerical techniques used to obtain the results discussed in Chapters III and IV.

CHAPTER II

GENERALIZED SQUEEZED STATES AND SCHRÖDINGER-CAT STATES

In this chapter we review generalized squeezed states and Schrödinger cat states. An understanding of these types of nonclassical boson states is essential to interpreting the results of the quantum theoretical work presented in Chapter III. Many of these states are most commonly known as photon states, but they are applicable to bosons in general, such as the phonons discussed in Chapter I and the remainder of the dissertation. While the technical issues involved in experimentally creating, measuring, and using phonons can be very different from those that feature in photonic experiments, the fundamental theory discussed here is identical.

2.1. Fock states

A Fock state has a well-defined number of phonons and is naturally expressed in the number basis (also known as the Fock basis). A Fock state $|\psi\rangle = |n\rangle$ is defined as the eigenstate of the number operator \hat{n} :

$$\hat{n}|n\rangle = n|n\rangle \tag{2.1}$$

Because of the uncertainty relation between phonon number and phase, a Fock state has no phase dependence; that is, it has a uniform phase distribution. (A measurement of the phase of a Fock state would have infinite uncertainty.)

It is illuminating to study the Wigner quasiprobability distribution of the Fock state, which visualizes the state's phase-space behavior. Here we consider the phase space defined by the Q and P quadratures. For a photon state, Q and P represent

the real and imaginary components of the electric field, respectively. They are often interpreted as analogues to the position and momentum of a quantum harmonic oscillator. For a phonon state, Q actually is the average of the position coordinates of all the collectively vibrating molecules, and P is the average of their momenta. For a pure phonon (or photon) state with quadrature representation $\langle Q|\psi\rangle = \psi(Q)$, the Wigner distribution is defined by [19]

$$W(Q, P) = \frac{1}{2\pi} \int_{-\infty}^{\infty} dQ' \exp(-iPQ') \psi(Q + Q'/2) \psi^*(Q - Q'/2). \quad (2.2)$$

In the quadrature basis (Q, P) , the number state $|n\rangle$ is represented by [20]

$$\langle n|Q\rangle = \psi_n(Q) = \frac{1}{\sqrt{2^n n! \sqrt{2\pi}}} \exp\left(-\frac{Q^2}{4}\right) H_n\left(\frac{Q}{\sqrt{2}}\right) \quad (2.3)$$

and its Wigner distribution is given by [20]

$$W(Q, P) = \frac{2}{\pi} (-1)^n \exp(-2(Q^2 + P^2)) L_n(4(Q^2 + P^2)) \quad (2.4)$$

where $L_n(x)$ is the Laguerre polynomial. The Wigner distribution for the Fock states $|1\rangle$ and $|2\rangle$ are illustrated in Figure 2.1.

The vacuum state is also easily expressed in the number basis and can be thought of as a zero-phonon Fock state. The Wigner distribution for the vacuum state $|vac\rangle = |0\rangle$ is illustrated in Figure 2.2. As indicated in Equation 2.3, the vacuum state is a Gaussian distribution centered at the origin.

Except for the vacuum state, all Fock states have some negative regions in their Wigner distributions. The negativity is an indication that Fock states are nonclassical states. Of course the entire concept of a Fock state depends on the concept of a quantum of light, so the nonclassicality is unsurprising.

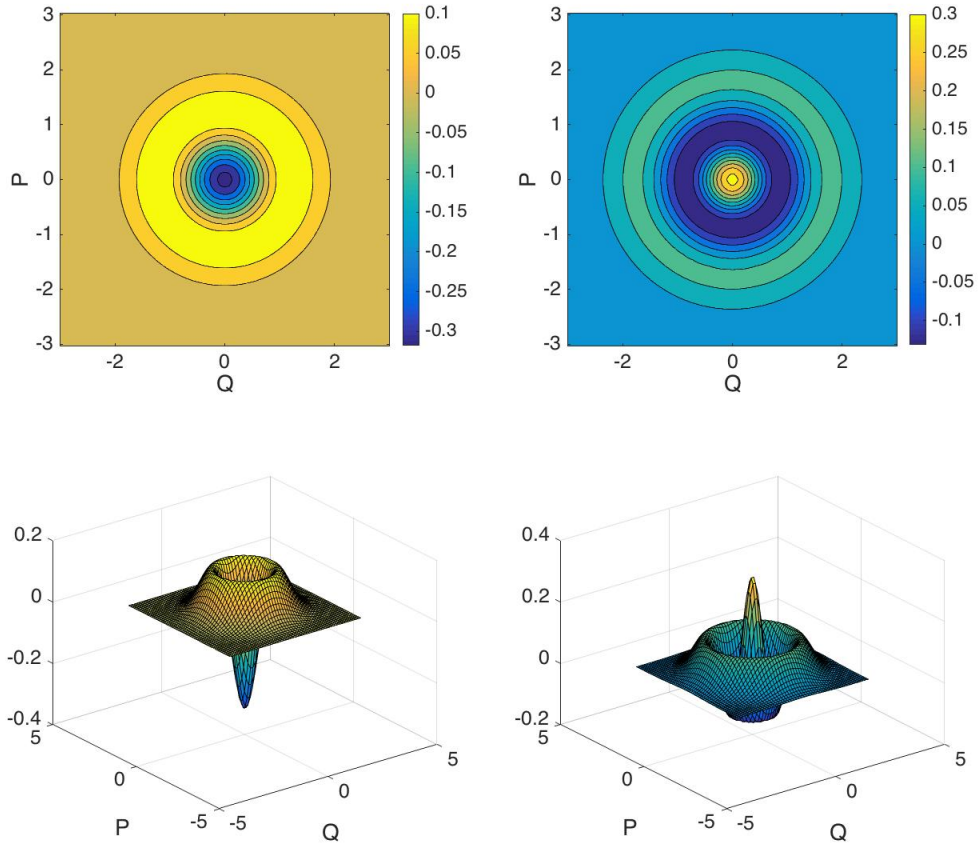


FIGURE 2.1. Example Fock state Wigner distributions. The Fock state $|1\rangle$ Wigner distribution is shown on the bottom left, with a corresponding contour plot in the top left. The Fock state $|2\rangle$ is shown on the bottom right, with a contour plot in the top right. Both distributions are invariant under phase rotations, as is true for all Fock states.

2.2. Squeezed vacuum states

The action of the squeezing operator on the vacuum state produces one of the most famous nonclassical states, the squeezed vacuum state. The squeezing operator has the form [20]

$$S(\zeta) = \exp\left[\frac{1}{2}(\zeta^* \hat{a}^2 - \zeta \hat{a}^{\dagger 2})\right] \quad (2.5)$$

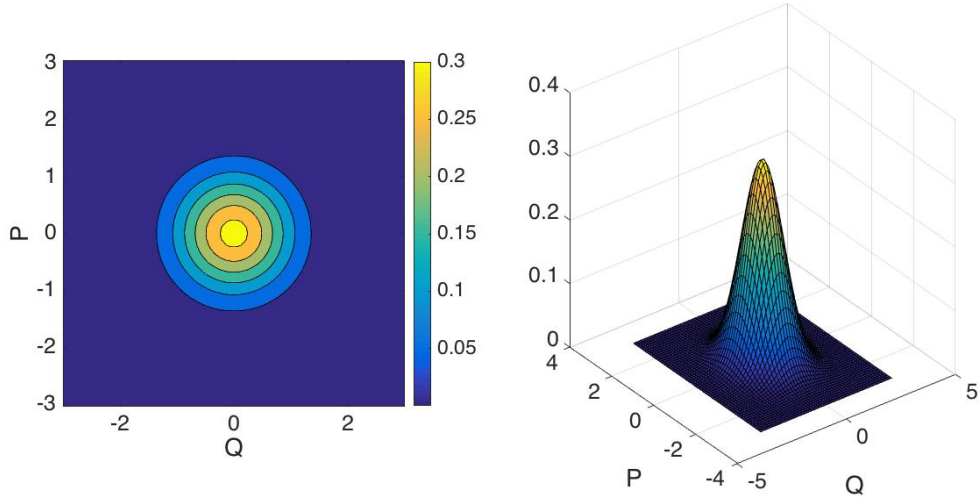


FIGURE 2.2. Vacuum state Wigner distributions. Left: contour plot of $W(Q, P)$. Right: 3D plot of $W(Q, P)$

When the squeezing operator acts on the vacuum state $|0\rangle$, it produces a superposition of number states in multiples of two:

$$S(\zeta)|0\rangle = C_0|0\rangle + C_2|2\rangle + C_4|4\rangle + \dots \quad (2.6)$$

where C_n is the complex amplitude of the state $|n\rangle$. In practice, when squeezed vacuum is created the vacuum amplitude C_0 is largest. The multiples of two in the number state superposition can be anticipated by considering that the squeezing operator is composed of the creation operator $\hat{a}^{\dagger 2}$ and its adjoint. In fact, one straightforward method to experimentally create optical squeezed vacuum is degenerate spontaneous parametric downconversion [18]. The interaction Hamiltonian for this process under the parametric approximation (in which the pump is treated as a constant classical field) is [21]

$$H = i\kappa A \hat{a}^{\dagger 2} - iA^* \kappa^* \hat{a}^2, \quad (2.7)$$

where A is the amplitude of the pump field and κ is a coupling constant. The time evolution operator corresponding to this Hamiltonian is equivalent to the squeezing operator of Equation 2.5, with the squeezing parameter ζ incorporating the pump amplitude and coupling constant.

In phase space, the squeezed vacuum state is an elliptical two-dimensional Gaussian with minor axes along the phases 0 and π . It looks like the result of literally “squeezing” the vacuum state phase-space distribution from Figure 2.2 along one axis (or phase), resulting in “anti-squeezing” along the other. The Wigner distribution for an example squeezed vacuum state is shown in Figure 2.3. (Calculating the Wigner distribution for a superposition of number states is discussed in Appendix A.)

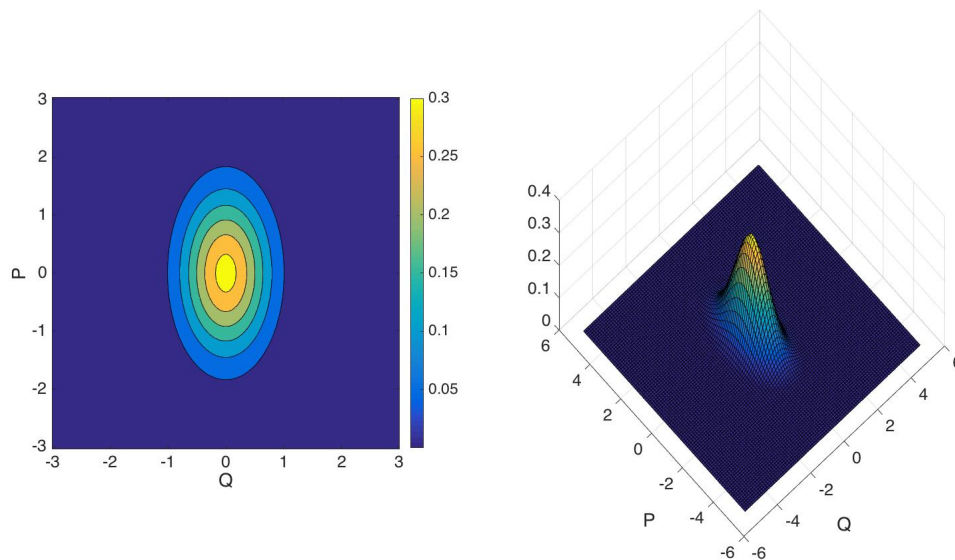


FIGURE 2.3. Wigner distribution of the squeezed vacuum state generated by the Hamiltonian in Equation 2.7 with $\kappa A = 10$ and $t = 0.015$. Left: contour plot of $W(Q, P)$. Right: 3D plot of $W(Q, P)$

The squeezing operator can be applied to any state, not just to the vacuum state. Figure 2.4 shows the Wigner distribution of a squeezed single-phonon state, that is,

a single-phonon state to which the squeezing operator has been applied. Comparing this distribution to the one shown for the single-phonon Fock state in 2.1, we see again that squeezing the state distorts it along the phases 0 and π .

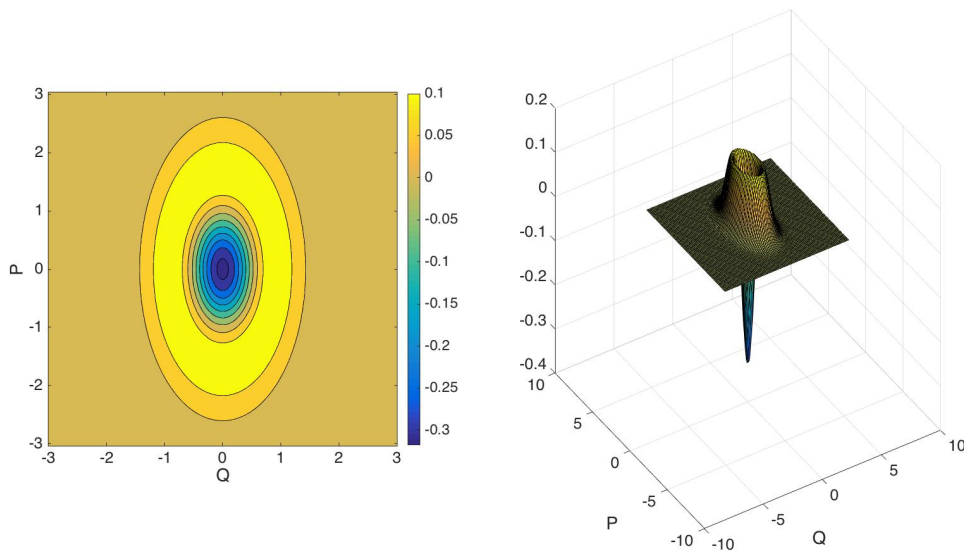


FIGURE 2.4. Wigner distribution of the squeezed single-phonon Fock state generated by the Hamiltonian in Equation 2.7 with $\kappa A = 10$ and $t = 0.015$. Left: contour plot of $W(Q, P)$. Right: 3D plot of $W(Q, P)$

Squeezed vacuum and squeezed states in general are perhaps best known for the fact that the fluctuations in one quadrature are reduced below the shot-noise limit. In the Wigner distribution in Figure 2.3, the reduction in fluctuation in the Q quadrature manifests as the decreased width of the distribution along the Q -axis relative to the vacuum-state distribution in Figure 2.2. The reduced fluctuations correspond to a reduced uncertainty in a measurement of the squeezed quadrature, which can be useful for applications such as precision spectroscopy [22] and gravitational wave interferometry [23]. In this dissertation, however, we will not focus on this feature of squeezed states. We instead move on to discuss generalized squeezed states.

2.3. Generalized squeezed states

Generalized squeezed states are so named because they generalize the squeezed-state Hamiltonian in Equation 2.7 to powers of k in the creation operator \hat{a}^\dagger :

$$H = i\kappa A \hat{a}^{\dagger k} - iA^* \kappa^* \hat{a}^k \quad (2.8)$$

where any $k \geq 3$ corresponds to generalized squeezing [24]. When discussing generalized squeezing, the case $k = 2$ as described in the previous section is usually called “ordinary squeezing” or “two-phonon squeezing” to prevent confusion.

The treatment of generalized squeezing is mathematically more difficult than ordinary squeezing and has been the source of some dispute in the literature. Initially Fisher, Nieto, and Sandberg studied the vacuum-state expectation value of the time evolution operator $U_k(t)$ corresponding to Hamiltonians of the form Equation 2.8:

$$\begin{aligned} \langle 0|U_k(t)|0\rangle &= 1 - |z_k|^2 \frac{k!}{2!} + |z_k|^4 \frac{1}{4!} [(k!)^2 + (2k)!] \\ &\quad - |z_k|^6 \frac{1}{6!} [(k!)^3 + 2k!(2k)! + \frac{1}{k!} [(2k)!]^2 + (3k)!] \\ &\quad + \dots + (-1)^n |z_k|^{2n} \frac{1}{(2n)!} C_n + \dots \end{aligned} \quad (2.9)$$

(where the constant z_k incorporates the parametric pump amplitude and any coupling constants). They found that this expectation value does not converge for any finite time when $k > 2$, and concluded that generalized squeezing is impossible [24]. Braunstein and McLachlan, however, were able to use Padé approximants [25] to analytically continue [26] the Taylor series expansion in 2.9 and numerically compute the evolution of the generalized squeezed states for $k = 3, 4$ for short times [17].

Hillery later pointed out [27] that the entire problem could be avoided by quantizing the pump (i.e., by not using the parametric approximation). Additionally, quantizing the pump prevents the mean phonon number from diverging [27], a problem that arises at finite time and relatively short time under the parametric approximation [27], [28]. Nevertheless, the parametric pump approximation can be useful for short times.

Interestingly, the generalized squeeze operator—or equivalently, the k -phonon generation or absorption operator for $k \geq 3$ —cannot lead to sub-shot-noise fluctuations when acting on the vacuum [17], [29]. That is, it is not squeezed in the ordinary sense of two-phonon vacuum. In other respects, however, multiphonon-squeezed vacuum is arguably more interesting than two-phonon-squeezed vacuum. As shown by Banaszek and Knight, the three-phonon-squeezed vacuum produced in three-phonon down conversion displays negativity in its Wigner distribution, which results from interference in phase space and is generally regarded as a signature of nonclassicality [30]. A three-phonon-squeezed vacuum state Wigner distribution is shown in Figure 2.5. Figure 2.6 shows the Wigner distribution of a three-phonon-squeezed single-phonon state¹. These two examples were computed numerically by methods described in Appendix C.

2.4. Schrödinger cat states

A Schrödinger cat state is a coherent superposition of macroscopically distinguishable states [31]. The name comes from one of the most famous thought experiments in physics, proposed by Erwin Schrödinger in 1935 to illustrate the contradiction between the indeterminacy expressed by quantum superpositions and the determinacy of the observed macroscopic world. The hypothetical experiment

¹That is, the state that is produced when the time-evolution operator corresponding to Equation 2.8 with $k = 3$ acts on the single-phonon state $|1\rangle$.

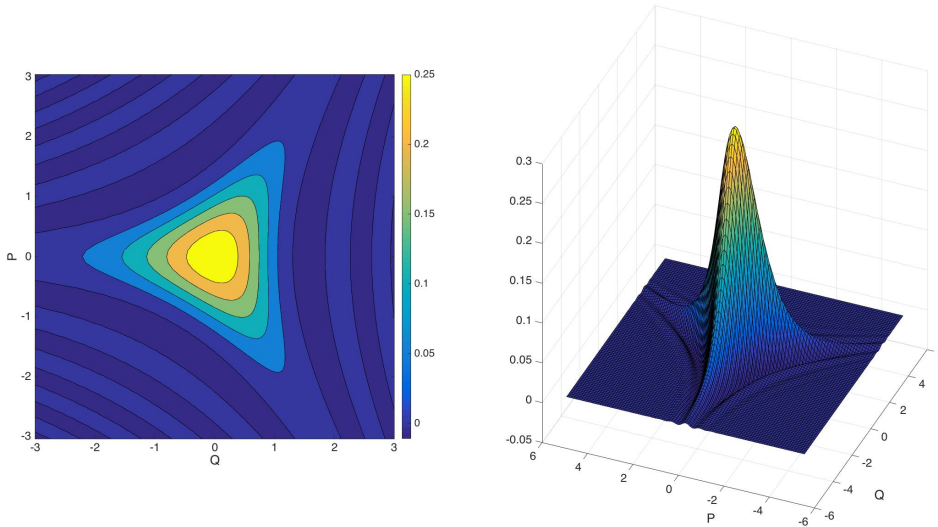


FIGURE 2.5. Wigner distribution of the three-phonon-squeezed vacuum state generated by the Hamiltonian in Equation 2.8 with $k = 3$, with parameters $\kappa A = 20$ and $t = 0.005$. Left: contour plot of $W(Q, P)$. Right: 3D plot of $W(Q, P)$. The interference fringes between the “arms” of the distribution take negative values, showing the three-phonon-squeezed vacuum to be a distinctly nonclassical state.

stars a cat who is trapped in a steel chamber with a canister of deadly poisonous gas. Also in the chamber is a small amount of radioactive substance, chosen such that there is a 50% chance that at least one atom will decay over the course of an hour, and also a Geiger counter connected to an apparatus that will smash the canister and release the poison if and only if it detects a decay [32]. Schrödinger reasoned that after an hour, the wave function of the system would be in an equal superposition of “atom decayed and cat dead” and “atom not decayed and cat alive.” Because it seems ludicrous to describe the cat subsystem as some combination of alive and dead, Schrödinger argued that the premise—that the atomic system could also be described as a superposition of incompatible states—was also untenable. As we know, quantum superpositions have indeed proven to be a useful way to model the microscopic world.

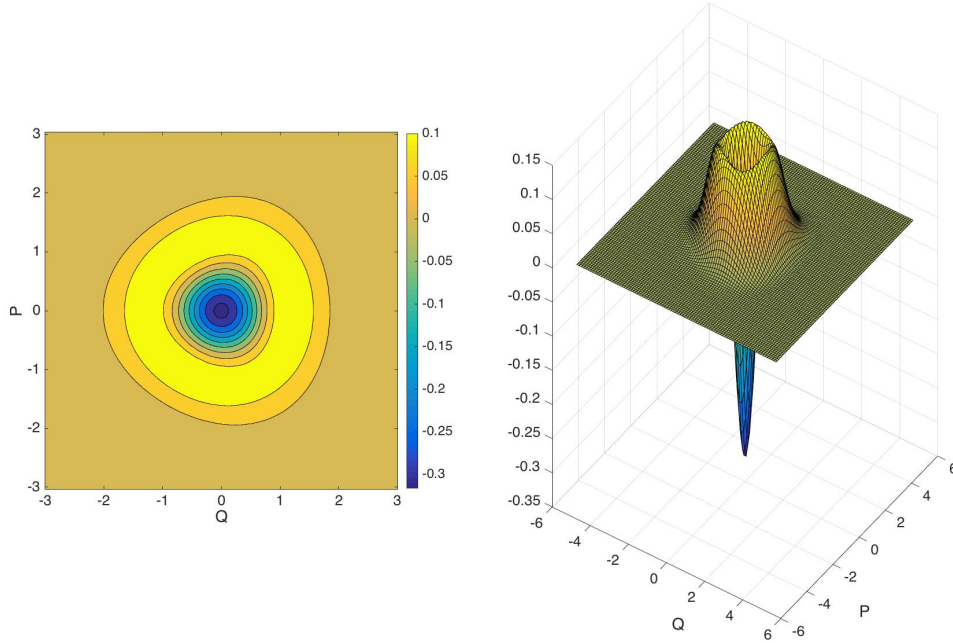


FIGURE 2.6. Wigner distribution of the three-phonon-squeezed single-phonon Fock state generated by the Hamiltonian in Equation 2.8 with $k = 3$, with parameters $\kappa A = 20$ and $t = 0.0005$. Left: contour plot of $W(Q, P)$. Right: 3D plot of $W(Q, P)$. The 3D plot shows some oscillations in the amplitude of the distribution at its maximum. This is a real effect and not an artifact.

Moreover, superpositions of macroscopically observable objects have been achieved in both optical and atomic systems [33], [34], [35], [36].

Creating an optical cat state requires a superposition of macroscopically detectable states of light. Coherent states are a natural choice of states [37], as they are generally considered the quantum states that most closely match classical waves [20]. A coherent state is defined by [20], [38]

$$|\alpha\rangle = \exp(-|\alpha|^2/2) \sum_{n=0}^{\infty} \frac{\alpha^n}{\sqrt{n!}} |n\rangle \quad (2.10)$$

The complex parameter α is the amplitude of the coherent state. When $\alpha = 0$, the coherent state has zero amplitude and is identically the vacuum state. In fact, a coherent amplitude with nonzero amplitude is simply a displacement of the vacuum state away from the phase-space origin [38].

The most common example of an optical cat state is an equal superposition of two relatively large-amplitude coherent states that are phase-shifted from each other by π :

$$|\psi\rangle = \frac{\exp(-|\alpha|^2/2)}{\sqrt{2}} \left(\sum_{n=0}^{\infty} \frac{\alpha^n}{\sqrt{n!}} |n\rangle + \sum_{n=0}^{\infty} \frac{\alpha^n \exp(in\pi)}{\sqrt{n!}} |n\rangle \right) \quad (2.11)$$

In analogy with Schrödinger’s thought experiment, one of these coherent states represents the cat being alive and the opposite-phase coherent state represents the cat being dead. A classical measurement of optical phase would result in the outcome π or 0 , which are readily distinguishable.

A Wigner distribution for the cat state of Equation 2.11 with amplitude $\alpha = 3$ is shown in Figure 2.7. The two Gaussian distributions that lie on the Q -axis are the “alive” and “dead” states, and the fringes between them indicate that the superposition is a coherent (nonclassical) superposition, rather than an incoherent (classical) statistical mixture.

It is not strictly necessary that the two component states be separated in phase by exactly π . They simply need to be far enough away in phase space that the two Gaussian distributions do not overlap significantly. Having opposite phases makes it easier to reduce this overlap and is therefore very common.

Superpositions of three or more coherent states can form a cat state as well. A three-component cat state with maximum phase shift $\pm 2\pi/3$ between the coherent states is

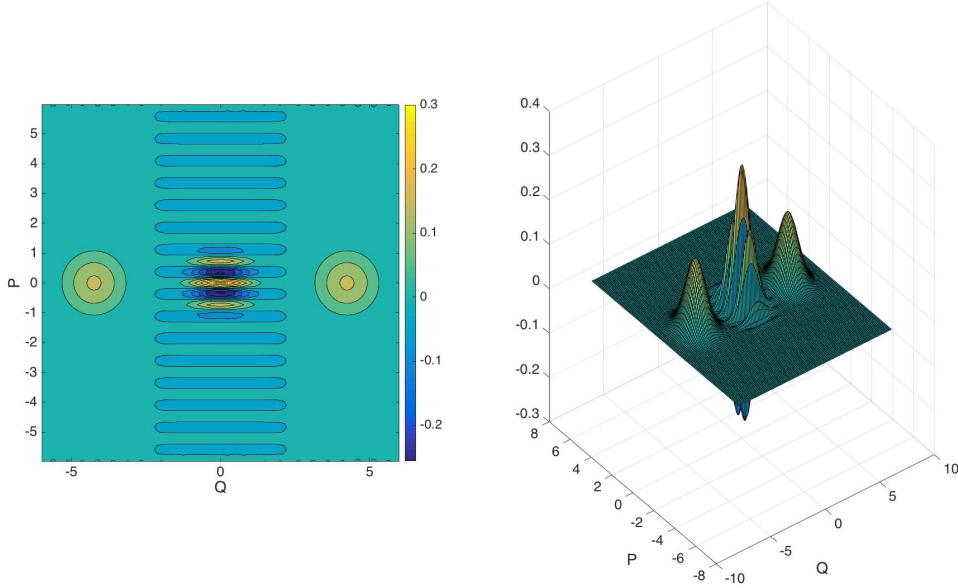


FIGURE 2.7. Wigner distribution of the optical two-component Schrödinger cat state in Equation 2.11, with $\alpha = 3$. Left: contour plot of $W(Q, P)$. Right: 3D plot of $W(Q, P)$.

$$\begin{aligned}
 |\psi\rangle &= \frac{\exp(-|\alpha|^2/2)}{\sqrt{3}} \sum_{n=0}^{\infty} \frac{\alpha^n}{\sqrt{n!}} |n\rangle \\
 &+ \frac{\exp(-|\alpha|^2/2)}{\sqrt{3}} \sum_{n=0}^{\infty} \frac{\alpha^n \exp(in2\pi/3)}{\sqrt{n!}} |n\rangle \\
 &+ \frac{\exp(-|\alpha|^2/2)}{\sqrt{3}} \sum_{n=0}^{\infty} \frac{\alpha^n \exp(-in2\pi/3)}{\sqrt{n!}} |n\rangle
 \end{aligned} \tag{2.12}$$

The Wigner distribution for an example three-component cat state is shown in Figure 2.8. Such states have been created in the microwave regime by Schoelkopf [36].

In the two- and three-component cat states shown in Figures 2.7 and 2.8, the component coherent states have relatively high amplitudes α and are thus well-separated in phase space and highly-distinguishable. If the coherent state amplitudes

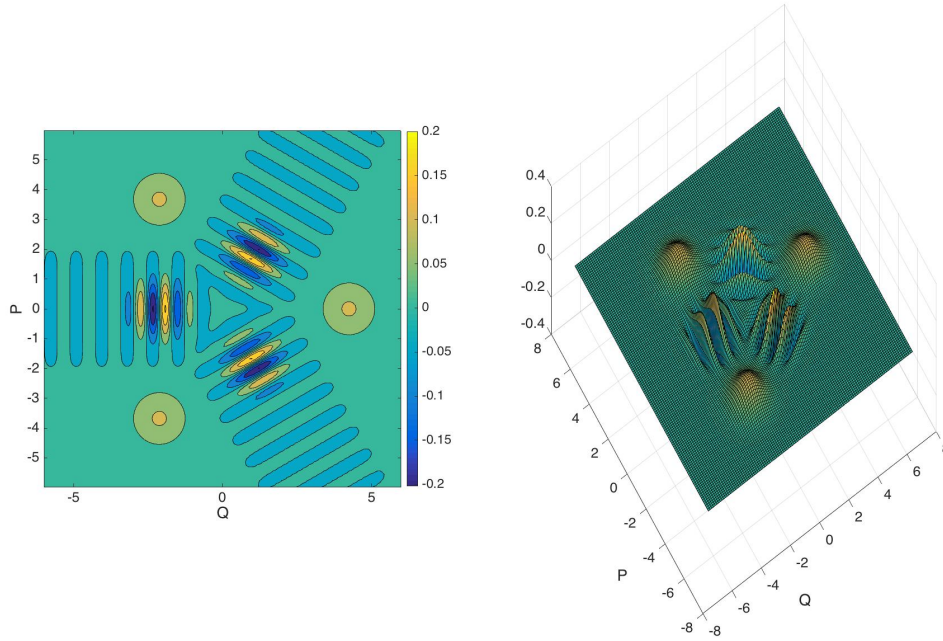


FIGURE 2.8. Wigner distribution of the three-component optical Schrödinger cat state in Equation 2.12, with $\alpha = 3$. Left: contour plot of $W(Q, P)$. Right: 3D plot of $W(Q, P)$.

are too small, the component states will overlap significantly. In that case, the component states are not easily distinguishable and the label “cat state” does not really apply. A superposition of coherent states with small amplitudes ($|\alpha| \lesssim 1.5$ [35]) is, in a strained analogy, sometimes called a “kitten state” [39], [40], [41].

2.5. Fidelity between kitten states and squeezed states

Figure 2.9 shows the Wigner distributions for three-component cat states with different values of α . The higher-amplitude cat states have almost no overlap, whereas in the lower-amplitude cat states the component coherent states overlap so much they look like one state with a triangular shape.

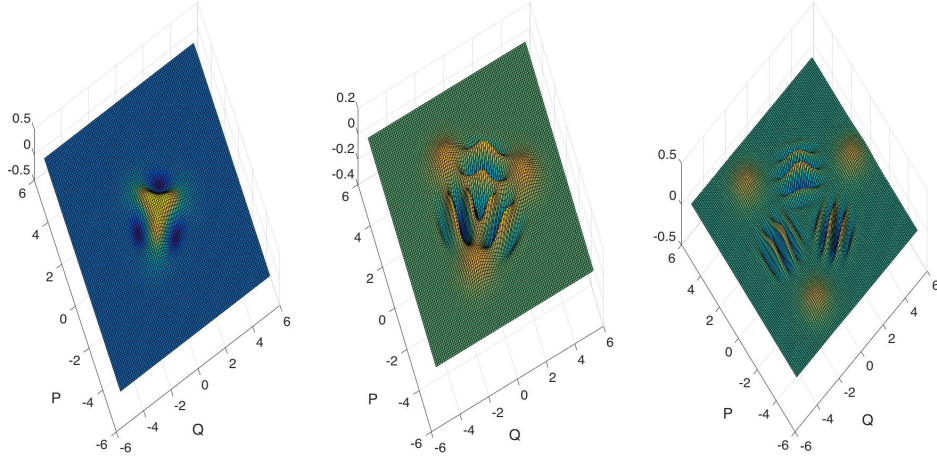


FIGURE 2.9. Wigner distribution of the three-component state in Equation 2.12, with $\alpha = 1$ (left), $\alpha = 2$ (center), and $\alpha = 3$ (right). The leftmost state (with $\alpha = 1$) is usually called a kitten state rather than a cat state, because the amplitude is so low that the three coherent states overlap with each other significantly. It resembles a three-phonon squeezed vacuum state, as shown in Figure 2.5

In fact, the three-component kitten state strongly resembles the three-phonon squeezed vacuum state defined in Equation 2.8 for $k = 3$ and illustrated by the Wigner distribution in Figure 2.5. As established previously, the generalized squeezing Hamiltonian in Equation 2.8 also describes k -phonon generation. In the case of triple phonon generation ($k = 3$), the state produced when this Hamiltonian acts on the vacuum is

$$|\psi\rangle = \sum_{n=0}^{\infty} C_n |3n\rangle. \quad (2.13)$$

That is, the resulting state is a superposition of phonon number states that are all multiples of three. The fact that the Hamiltonian is composed of cubic powers of the creation and annihilation operator suggests this result. In Appendix B, we prove rigorously that it follows from the threefold rotational symmetry of the Hamiltonian. We also show in Appendix B that the phase-space distribution of such

a state is threefold symmetric. The remarkable correspondence between the rotational symmetry of the Hamiltonian and the number-basis representation of the state will also help to explain the predictions of the quantum model of the dual-pumped Raman frequency comb discussed in Chapter III.

From Equation 2.12 we can also show that a cat (or kitten) state made of equal-amplitude coherent states must contain only multiple-of-three phonon states:

$$\begin{aligned}
|\psi\rangle &= \frac{\exp(-|\alpha|^2/2)}{\sqrt{3}} \sum_{n=0}^{\infty} \frac{\alpha^n}{\sqrt{n!}} |n\rangle \\
&+ \frac{\exp(-|\alpha|^2/2)}{\sqrt{3}} \sum_{n=0}^{\infty} \frac{\alpha^n \exp(in2\pi/3)}{\sqrt{n!}} |n\rangle \\
&+ \frac{\exp(-|\alpha|^2/2)}{\sqrt{3}} \sum_{n=0}^{\infty} \frac{\alpha^n \exp(-in2\pi/3)}{\sqrt{n!}} |n\rangle \\
&= \frac{\exp(-|\alpha|^2/2)}{\sqrt{3}} \sum_{n=0}^{\infty} \frac{\alpha^n (1 + \exp(in2\pi/3) + \exp(-in2\pi/3))}{\sqrt{n!}} |n\rangle \\
&= \frac{\exp(-|\alpha|^2/2)}{\sqrt{3}} \sum_{n=0}^{\infty} \frac{\alpha^n (1 + 2 \cos(2\pi n/3))}{\sqrt{n!}} |n\rangle.
\end{aligned} \tag{2.14}$$

The quantity $1 + 2 \cos(2\pi n/3)$ is equal to zero unless $n = 0, 3, 6, \dots, 3k$, where k is a nonnegative integer. Shifting the phases of the three component coherent states relative to each other by $2\pi/3$ does not change the threefold symmetry of the superposition in phase space, but does change the number states in the superposition:

$$\begin{aligned}
|\psi\rangle &= \frac{\exp(-|\alpha|^2/2)}{\sqrt{3}} \sum_{n=0}^{\infty} \frac{\alpha^n}{\sqrt{n!}} |n\rangle \\
&+ \exp(\pm i2\pi/3) \frac{\exp(-|\alpha|^2/2)}{\sqrt{3}} \sum_{n=0}^{\infty} \frac{\alpha^n \exp(in2\pi/3)}{\sqrt{n!}} |n\rangle \\
&+ \exp(\mp i2\pi/3) \frac{\exp(-|\alpha|^2/2)}{\sqrt{3}} \sum_{n=0}^{\infty} \frac{\alpha^n \exp(-in2\pi/3)}{\sqrt{n!}} |n\rangle \\
&= \frac{\exp(-|\alpha|^2/2)}{\sqrt{3}} \sum_{n=0}^{\infty} \frac{\alpha^n (1 + \exp(in2\pi/3 \pm i2\pi/3) + \exp(-in2\pi/3 \mp i2\pi/3))}{\sqrt{n!}} |n\rangle,
\end{aligned} \tag{2.15}$$

where now either $n + 1 = 0, 3, 6, \dots, 3k$ or $n - 1 = 0, 3, 6, \dots, 3k$. So the three-component cat state can be a superposition of $n = 0, 3, 6, \dots, 3k$ or of $n = 1, 4, 7, \dots, 3k + 1$ or of $n = 2, 5, 8, \dots, 3k + 2$. These three types of three-component cat states are a generalization of the better-known odd and even two-component cat states, where the even cat state is defined in Equation 2.11 and the odd cat state is produced by shifting one of the two coherent states in the even cat state by π [42].

Therefore the three-component equal-amplitude cat state has nonzero amplitude only for number states that come in multiples of three, just like the three-phonon squeezed vacuum state. The similarity between these two states (for given values of the parameters κAt and α) can be quantified as the fidelity:

$$F = |\langle \psi_{3ph} | \psi_{3cat} \rangle|^2. \tag{2.16}$$

The fidelity is a scalar between 0 and 1 [43]. Two identical states have unit fidelity, and orthogonal states have zero fidelity.

The fidelity between the kitten state shown in Figure 2.9 (where $\alpha = 1$) and the three-phonon squeezed vacuum shown in Figure 2.5 ($-\kappa A = 20^2$ and $t = 0.005$) is $\approx 87.3\%$. The kitten state with amplitude $\alpha \approx 0.4$ most closely matches the three-phonon squeezed vacuum. With that amplitude the fidelity is $> 99.99958\%$.

²The negative sign indicates a phase rotation of the pump relative to the example in Figure 2.5, which was performed in order to achieve the same overall phase as the kitten state for this example.

CHAPTER III

QUANTUM THEORY OF CONDITIONED PHONON STATES

In this chapter we present numerical results from a simulation of a dual-pumped Raman optical frequency comb. Details on the numerical methods used are in Appendix C.

3.1. Description of the dual-pumped Raman frequency comb

We model an optical frequency comb created by two strong optical fields (called pump fields) incident on a medium with a single Raman-active mode. The interaction occurs inside an optical cavity (that is, with no pulse propagation). A key feature of our model is that the pump fields are phase-locked together and are separated in frequency by three times the Raman phonon frequency. As a result of this frequency separation, the anti-Stokes sideband created by the low-frequency (red) pump and the Stokes sideband created by the high-frequency (blue) pump are separated in frequency by one Raman shift. Therefore Raman scattering between those two sidebands is possible and is mediated by the same phonon mode that couples to Raman scattering directly from the pumps.

The cavity supports six optical modes altogether, ranging from the mode populated by Stokes scattering from the red pump to the mode populated by anti-Stokes scattering from the blue pump. Two of these optical modes are occupied by the strong pump fields. The other four are initially in the vacuum state. In order of increasing frequency, those four modes will be called the red-Stokes, the red-anti-Stokes, the blue-Stokes, and the blue-anti-Stokes modes. The spectrum is illustrated in Figure 3.1.

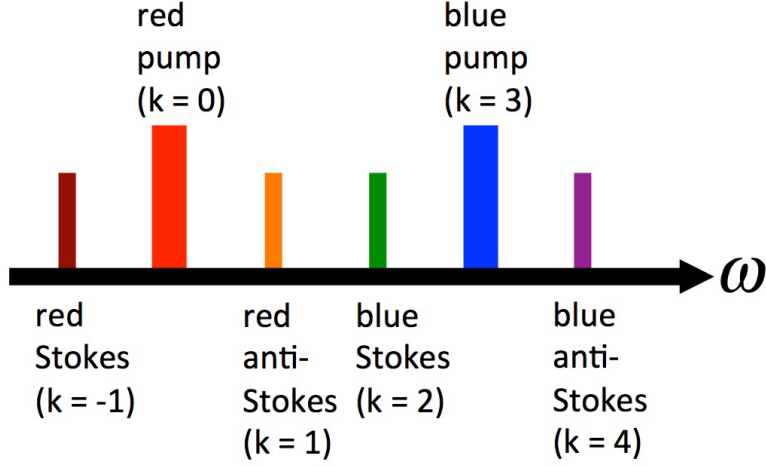


FIGURE 3.1. Dual-pumped Raman optical frequency comb spectrum.

In this model, we assume there is no dephasing of the Raman phonon mode by, for example, collisions. We also assume that the cavity decay time is much longer than the interaction time following the steady-state pumps being suddenly switched on. Therefore we neglect all decoherence processes and treat the time evolution as unitary, leading to pure-state evolution. While this scenario is idealized compared to realistic experiments, it allows us to solve the quantum evolution equation essentially exactly by numerical means, leading to a new family of state-generating processes that have not been predicted or studied previously.

In mathematics it is convenient to label each optical mode by an integer specifying its separation in frequency from the red pump. That is, mode k has frequency $\Omega_{\text{red pump}} + k\omega_{\text{phonon}}$. We arbitrarily choose a numbering scheme where $k = 0$ corresponds to the red pump, $k = -1$ corresponds to the red-Stokes mode, and $k = 1, 2, 3, 4$ corresponds to the red-anti-Stokes, the blue-Stokes, the blue pump, and the blue-anti-Stokes modes respectively.

Raman scattering in the dual-pumped Raman medium is described by the following interaction Hamiltonian:

$$\begin{aligned}
H = & -ib^\dagger a_{-1}^\dagger A_0 - ib^\dagger A_0^\dagger a_1 - ib^\dagger a_1^\dagger a_2 - ib^\dagger a_2^\dagger A_3 - ib^\dagger A_3^\dagger a_4 \\
& + iba_{-1} A_0^\dagger + ibA_0 a_1^\dagger + iba_1 a_2^\dagger + iba_2 A_3^\dagger + ibA_3 a_4^\dagger,
\end{aligned} \tag{3.1}$$

where b is a boson annihilation operator for the phonon mode and a_k is a boson annihilation operator for the k th optical mode. The strong pump field operators are denoted A_0 and A_3 , using capital letters to distinguish them from the weak signal fields. Later we will take the pump fields to be in strong coherent states (with zero phase), so they can be treated as classical fields. Before making that approximation, we will consider some symmetry properties of the Hamiltonian in order to gain insight about the nature of the states expected to be generated by it. Each term in the Hamiltonian represents scattering of a photon from one mode to an adjacent mode, accompanied by either the creation of a phonon (when the photon scatters into a lower-frequency mode) or the destruction of a phonon (when the photon scatters into a higher-frequency mode). These processes are Stokes and anti-Stokes scattering respectively. Because the medium is in a cavity, there is no pulse propagation and therefore no spatial dependence in the Hamiltonian. We have assumed that any coupling coefficient between the phonon mode and an optical mode or between two optical modes can be treated as identical for each term in this Hamiltonian. In this case the coupling coefficient can be treated as an overall scaling factor, or absorbed into the time t in the time-evolution operator $\exp(-iHt)$. We therefore do not write the coupling coefficient explicitly in the Hamiltonian. Finally, we ignore cavity dispersion, which otherwise would detune the optical mode frequencies from the ideal comb frequencies that are separated by exactly the phonon frequency.

3.1.1. Rotational symmetry of the dual-pumped Raman comb Hamiltonian

The effect of the two strong pumps fixing the phases of the $k = 0$ and $k = 3$ modes is significant, because it determines the rotational symmetry of the Hamiltonian. Specifically, if the pump phases are not fixed, then the Hamiltonian is invariant under the global phase-space rotation $R(\phi) = \exp(-i\phi\hat{N}) \exp(-i \sum_k k\phi\hat{n}_k)$ for any value of ϕ . But if the two pump phases are fixed, then the Hamiltonian is invariant under $R(\phi)$ only for certain values of ϕ . We prove this now.

3.1.11. Proof of invariance of the Hamiltonian under $R(\phi)$ with fixed or unfixed pump phases

The global phase-space rotation $R(\phi)$ rotates the creation and annihilation operators of the Hamiltonian in this way¹:

$$\begin{aligned} a_k &\rightarrow a_k \exp(ik\phi) \\ a_k^\dagger &\rightarrow a_k^\dagger \exp(-ik\phi) \\ A_k &\rightarrow A_k \exp(ik\phi) \\ A_k^\dagger &\rightarrow A_k^\dagger \exp(-ik\phi) \\ b &\rightarrow b \exp(i\phi) \\ b^\dagger &\rightarrow b^\dagger \exp(-i\phi) \end{aligned} \tag{3.2}$$

¹Thanks to Steven van Enk for pointing out this symmetry.

In order to illustrate the impact of this symmetry, we first show the rotational invariance of the Hamiltonian under $R(\phi)$ *without* fixing the pump phases, and then show how the symmetry changes when the pump phases *are* fixed.

If the pump phases are *not* fixed, then the transformation defined in Equations 3.2 rotates the Hamiltonian in this way:

$$\begin{aligned}
H &= -b^\dagger \exp(-i\phi)a_{-1}^\dagger \exp(-i(-1)\phi)A_0 \exp(i0\phi) \\
&- ib^\dagger \exp(-i\phi)A_0^\dagger \exp(-i0\phi)a_1 \exp(i1\phi) \\
&- ib^\dagger \exp(-i\phi)a_1^\dagger \exp(-i1\phi)a_2 \exp(i2\phi) - ib^\dagger \exp(-i\phi)a_2^\dagger \exp(-i2\phi)A_3 \exp(i3\phi) \\
&- ib^\dagger \exp(-i\phi)A_3^\dagger \exp(-i3\phi)a_4 \exp(i4\phi) + ib \exp(i\phi)a_{-1} \exp(i(-1)\phi)A_0^\dagger \exp(-i0\phi) \\
&+ ib \exp(i\phi)A_0 \exp(i0\phi)a_1^\dagger \exp(-i1\phi) + ib \exp(i\phi)a_1 \exp(i1\phi)a_2^\dagger \exp(-i2\phi) \\
&+ ib \exp(i\phi)a_2 \exp(i2\phi)A_3^\dagger \exp(-i3\phi) + ib \exp(i\phi)A_3 \exp(i3\phi)a_4^\dagger \exp(-i4\phi) \\
&= H.
\end{aligned} \tag{3.3}$$

In other words, if the pump phases are not fixed, then the Hamiltonian in Equation 3.1 is invariant under the rotation $R(\phi)$ for any value of ϕ . More generally, even for a comb with more sidebands than we are considering here, every term in the Hamiltonian is of the form $ba_k a_{k+1}^\dagger$ (or the adjoint), and under $R(\phi)$,

$$ba_k a_{k+1}^\dagger \rightarrow b \exp(i\phi)a_k \exp(ik\phi)a_{k+1}^\dagger \exp(-i(k+1)\phi) = ba_k a_{k+1}^\dagger. \tag{3.4}$$

That is, no matter the value of ϕ , each term is unchanged.

But now suppose that instead the two pump modes located at $k = j$ and $k = m$ are treated as coherent fields with *fixed* phases ϕ_j and ϕ_m . Then under the rotation

$R(\phi)$, every term in the Hamiltonian that does not include the two pump fields is unchanged, and the terms that do include the pump fields transform as follows:

$$\begin{aligned} bA_{pump\ j}a_{j+1}^\dagger &\rightarrow b \exp(i\phi)A_{pump\ j} \exp(i\theta_{pump\ j})a_{j+1}^\dagger \exp(-i(j+1)\phi) \\ ba_{j-1}A_{pump\ j}^\dagger &\rightarrow b \exp(i\phi)a_{j-1} \exp(i(j-1)\phi)A_j^\dagger \exp(-i\theta_{pump\ j}) \end{aligned} \quad (3.5)$$

The terms involving the other pump, $A_{pump\ m}$, transform in the same way. Because the terms in the Hamiltonian that do not include the two pump fields have no overall phase shift, the Hamiltonian is invariant only when the phase shifts predicted by Equations 3.5 are zero or integer multiples of 2π . In other words, the Hamiltonian is invariant when

$$\begin{aligned} \theta_{pump\ j} - j\phi &= \theta_{pump\ m} - m\phi = 2\pi N \\ \rightarrow \phi &= \frac{1}{m-j}(\theta_{pump\ m} - \theta_{pump\ j}) + \frac{2\pi N}{m-j}. \end{aligned} \quad (3.6)$$

The Hamiltonian with fixed pump phases is invariant under the rotation $R(\phi)$ only when ϕ takes on certain values. The number of possible values this phase can take is determined by $m-j$, where $(m-j)\omega_{phonon}$ is the frequency difference between the two pumps. The possible values are discrete and evenly distributed between 0 and 2π . As shown in Equation 3.6, the values of ϕ that lead to invariance of the Hamiltonian depend on the phase difference between the two pumps. Without loss of generality, we set the phases of the pump fields A_0 and A_3 to zero. As a result, the Hamiltonian has the same form when rotated (or, equivalently, phase-shifted) by $\phi = 0$, $\phi = 2\pi/3$, and $\phi = -2\pi/3$.

Note that the threefold symmetry results from the pump phases being fixed, but does not depend on the assumption that the pumps are non-depleting fields. For example, we could treat the pumps as coherent states with evolving amplitudes but fixed phase and obtain the same result.

3.2. Time evolution from the vacuum state

In all of the following, we model the pumps A_0 and A_3 as undepleted classical fields with zero phase.

The Hamiltonian determines the evolution of the state of the system from its initial state:

$$|\psi(t)\rangle = \exp(-iHt)|\psi(t=0)\rangle. \quad (3.7)$$

The initial condition $|\psi(t=0)\rangle$ is taken to be the vacuum state $|0\rangle$ in all five modes. Under the non-depleting pump approximation, Equation 3.7 is valid only for small times t . In this limit, however, there is potential to observe interesting few-phonon or few-photon states.

Numerically solving Equation 3.7 is a technical challenge due to the size of the Hamiltonian matrix. At the time and pump amplitudes considered here, it is necessary to model up to 25 photons or phonons in each of the five modes. The resulting Hamiltonian matrix has more than 10^{14} elements, of which over 10^8 are nonzero. Details of our numerical methods are given in Appendix C. We numerically solve Equation 3.7 to produce the state of the system $|\psi(t)\rangle$ as a superposition of number states of the five modes:

$$|\psi(t)\rangle = \sum_{Nn_{-1}n_1n_2n_4} C_{Nn_{-1}n_1n_2n_4}(t)|N, n_{-1}, n_1, n_2, n_4\rangle, \quad (3.8)$$

where N is the number of phonons and n_{-1}, n_1, n_2, n_4 are the number of photons in each optical mode.

Probability distributions for the phonon number and the photon number in each mode are shown in Figure 3.2 for pump amplitudes $A_0 = A_3 = 60$ (corresponding to $60^2 = 3600$ photons in each pump mode) and $t = 0.015$.

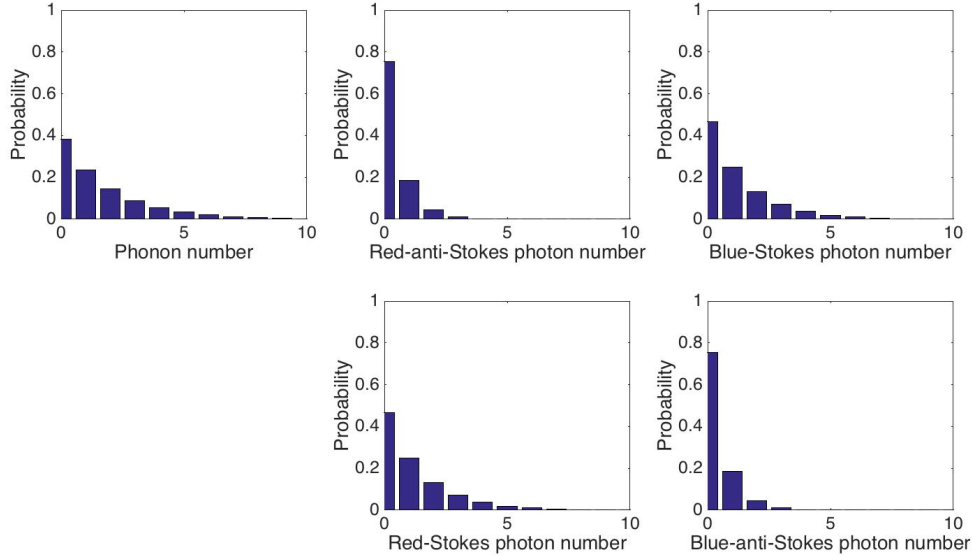


FIGURE 3.2. Photon- and phonon-number probability distributions for dual-pumped Raman comb for $A_0 = A_3 = 60$ and $t = 0.015$. In principle the probability distribution continues into infinitely high photon (or phonon) numbers.

In Figure 3.3 we show the unconditioned Wigner distribution of the phonon mode of this state with the photon modes removed by a partial trace. In this case the phonon mode is in a mixed state. To compute this Wigner distribution, we neglected all components of the superposition with more than six photons in any mode. There is only a 0.0212 probability that a photon number measurement would

find more than six photons in any mode, so this Wigner distribution should be a good approximation to the true one. By eye the Wigner distribution appears to be completely independent of phase. But in fact the distribution does show a slight three-phase preference. To detect this three-phase preference, we define a curve of constant $W(Q, P)$ (here $W(Q, P) = 0.01$) and plot the distance of that curve from the (Q, P) -plane origin. That plot, shown on the right in Figure 3.3, has three maxima separated by approximately $2\pi/3$. The maxima indicate a very slight preferential growth of the phonon mode along those three angles. This result is consistent with our expectations based on the semiclassical modeling and experimental results reviewed in Chapter I.

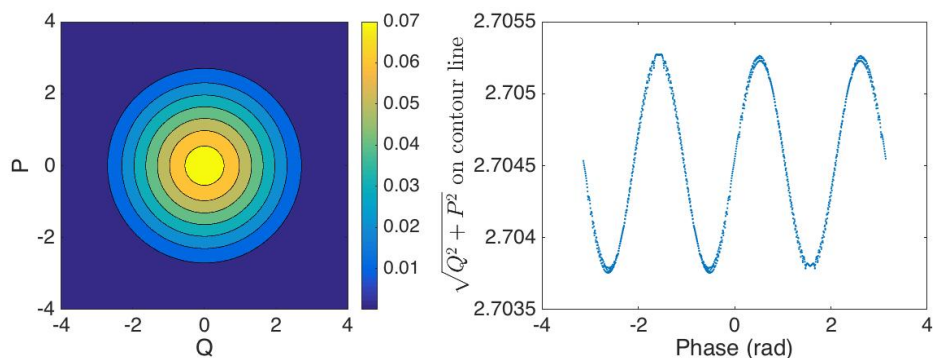


FIGURE 3.3. Left: Wigner distribution for the phonon mode of the dual-pumped Raman comb with $A_0 = A_3 = 60$ and $t = 0.015$, with photon modes traced out. Right: The distance from the phase-space origin of a line of constant $W(Q, P) = 0.01$ from the 2D projection of the Wigner distribution of the left.

The likely reason the three-phase preference of the phonon mode is so small is that the time at which the mode has been modeled is very short. The vacuum mode still dominates the phonon mode superposition. It is possible that at a longer time, the three-phase preference would become more obvious, but increasing the time of the simulation is numerically prohibitive.

A more interesting approach is to condition the phonon mode on measuring particular numbers of photons in the optical modes. By this method we can

circumvent the dominance of the vacuum mode and further explore the three-phase preference of the phonon mode. More significantly, conditioning on measured photon numbers creates a variety of interesting and potentially useful nonclassical pure states of the phonon mode. Additionally, we can gain insight into the dual-pumped Raman comb generation dynamics by characterizing the conditional phonon states based on the measured photon numbers that produced them. That characterization is the subject of the remainder of this chapter.

3.3. Conditioning on photon number measurements

We investigate the state of the phonon mode conditioned on measuring particular numbers of photons in each optical mode. The photon number measurements project the state from Eq 3.8 onto the appropriate photon number state for each mode, producing the conditioned phonon state

$$|\psi_{cond}(t)\rangle = \sum_N C_{N, n_{-1}^{meas} n_1^{meas} n_2^{meas} n_4^{meas}}(t) |N\rangle. \quad (3.9)$$

For simplicity we have omitted a normalization factor from Equation 3.9, leaving it unnormalized. Strictly speaking, the loss of information incurred by not quantizing the pump makes the conditional state a mixed state. However, because the pumps are strong and only lose a very small fraction of their photons in the short times we consider, the conditioned state is to excellent approximation pure and can be successfully treated as such.

For a given conditioning measurement outcome (that is, a given set of four photon numbers), we find by inspecting thousands of the possible states created by different choices of conditioning numbers that the conditioned phonon state is always a superposition of the series of number states given by

$$\sum_{m=0}^{\infty} |3m + j\rangle \tag{3.10}$$

$$j = [(n_{-1}^{meas} + n_2^{meas}) - (n_1^{meas} + n_4^{meas})] \pmod{3}.$$

That is, the number states in the superposition always occur in multiples of three, and they can be the sequence 0,3,6,... or 1,4,7,... or 2,5,8,... As shown in Appendix B, this remarkable result is a direct consequence of the threefold rotational symmetry of the Hamiltonian that we proved in Equations 3.2 - 3.6. The quantity $(n_{-1}^{meas} + n_2^{meas}) - (n_1^{meas} + n_4^{meas})$ is key to interpreting the results that follow. It corresponds to the difference between the number of photons in the optical modes that are Stokes-shifted from the pumps and the number of photons in the optical modes that are anti-Stokes-shifted from the pumps, as illustrated in Figure 3.1. We therefore define

$$\Delta_{SAS} \equiv (n_{-1}^{meas} + n_2^{meas}) - (n_1^{meas} + n_4^{meas}) \tag{3.11}$$

throughout the remainder of the dissertation. Then Equation 3.10 tells us that the value of j in the superposition of $|3m + j\rangle$ states equals one of the possible values of the quantity $\Delta_{SAS} \pmod{3}$. Specifically, the 0,3,6... state is produced when $\Delta_{SAS} \pmod{3} = 0$; the 1,4,7... state is produced when $\Delta_{SAS} \pmod{3} = 1$; and the 2,5,8... state is produced when $\Delta_{SAS} \pmod{3} = 2$. We can understand this pattern by considering the combinations of Raman scattering processes that could possibly contribute to a given photon number measurement via the procedure outlined below.

3.3.1. Classically counting Raman processes

There are effectively three types of Raman processes that can occur in the system defined by 3.1:

- **First-order scattering:** scattering a photon from a pump at frequency Ω_{pump} into an adjacent mode at $\Omega_{pump} \pm \omega_{phonon}$;
- **Second-order scattering:** scattering from a pump into an adjacent mode at $\Omega_{pump} \pm \omega_{phonon}$ and then out of that mode into the next mode at $\Omega_{pump} \pm 2\omega_{phonon}$;
- **Third-order scattering:** scattering from a pump into an adjacent mode, out of that mode and into the mode adjacent to that, and finally out of that mode and into the mode beyond that at $\Omega_{pump} \pm 3\omega_{phonon}$, which is the other pump.

We refer to these processes as first-order scattering, second-order scattering, and third-order scattering, respectively. (Note that these definitions are not equivalent to the usual definitions of first-, second-, and third-order scattering in general. We are defining the order of the scattering process by the frequency difference between the pump that originally lost the photon and the mode in which the surviving photon is created.)

Both Stokes and anti-Stokes first-order scattering can originate in either the red pump or the blue pump, but the only second- and third-order processes from the red pump are anti-Stokes processes, and the only second- and third-order processes from the blue pump are Stokes processes. (If our model included more modes beyond the blue-anti-Stokes mode and the red-Stokes mode, that would not be the case.) These processes are illustrated in Figure 3.4.

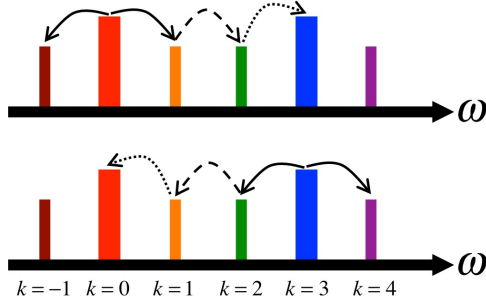


FIGURE 3.4. Illustration of first-, second-, and third-order scattering. Above: First- and higher-order processes originating from the red pump. The higher-order processes are all anti-Stokes processes. Below: First- and higher-order processes originating from the blue pump. The higher-pump order processes are all Stokes processes. Solid lines indicate first-order scattering, dashed lines indicate second-order scattering, and dotted lines indicate third-order scattering.

In a first-order process, the mode at frequency $\Omega_{pump} \pm \omega_{phonon}$ gains a photon. In a second-order process, the mode at $\Omega_{pump} \pm \omega_{phonon}$ has no net change in photon number, because it gains and then loses the photon from the pump. In a third-order process, none of the sidebands has a net change in photon number, because the photon scattered out of one pump and ended up in the other pump, and the pump is not quantized in this model. Second- and third-order Stokes processes create two and three phonons respectively, whereas second- and third-order anti-Stokes processes annihilate two and three phonons respectively. Because third-order scattering creates or annihilates three phonons with no net effect on the optical modes, it is very similar to the three-phonon-squeezing process corresponding to the Hamiltonian in Equation 2.8 in Chapter II (with $k = 3$).

Now consider the combinations of these processes that could produce the set of measured photon numbers $n_{-1}^{meas}, n_1^{meas}, n_2^{meas}, n_4^{meas}$.

First, suppose this observed photon combination was created by first-order scattering alone. These processes would have produced one phonon for every photon

in the red-Stokes mode and one for every photon in the blue-Stokes mode, because in this case each of those photons could only have been created by one Stokes scattering process. But it would have annihilated one phonon for every photon in the red-anti-Stokes mode and also for every photon in the blue-anti-Stokes mode, because each of those photons could only have been created by one anti-Stokes scattering process. So the net number of phonons created to generate this number of photons by first-order scattering alone is

$$N = (n_{-1}^{meas} + n_2^{meas}) - (n_1^{meas} + n_4^{meas}) = \Delta_{SAS}. \quad (3.12)$$

Now suppose that of the n_1^{meas} photons in the red-anti-Stokes mode, x of them were created by second-order Stokes scattering from the blue pump and $n_1^{meas} - x$ were created by first-order scattering, and all the other modes were populated by first-order scattering. Every photon created in the red-anti-Stokes mode via second-order Stokes scattering produces two phonons. Therefore the net number of phonons created by this set of processes is

$$N = (n_{-1}^{meas} + n_2^{meas}) - (n_1^{meas} - x + n_4^{meas}) + 2x = \Delta_{SAS} + 3x. \quad (3.13)$$

Next suppose there is also some second-order anti-Stokes scattering, so that of the n_2^{meas} photons in the blue-Stokes mode, y were created by second-order anti-Stokes scattering and $n_2^{meas} - y$ were created by first-order Stokes scattering. Then as a result of the first-order scattering and the second-order Stokes scattering and the second-order anti-Stokes scattering, the net number of phonons is

$$N = (n_{-1}^{meas} - y + n_2^{meas}) - (n_1^{meas} - x + n_4^{meas}) + 2x - 2y \quad (3.14)$$

$$N = \Delta_{SAS} + 3(x - y).$$

Finally we consider third-order scattering from pump to pump. This process either creates or annihilates three phonons without changing the net number of photons in each sideband. If j third-order Stokes processes and k third-order anti-Stokes processes occur as well, the net number of phonons is

$$N = \Delta_{SAS} + 3(x + j - y - k). \quad (3.15)$$

Combinations of processes where one process simply reverses another are ignored for this calculation, because that pair of processes results in no net change to the photon or phonon numbers. For instance, the possibility that a photon will scatter from the red pump to the red-Stokes mode and back again is ignored. Then any combination of processes can be expressed as a combination of the first-, second-, and third-order processes we have outlined here.

Thus we have shown that when the measured photon numbers are $n_{-1}^{meas}, n_1^{meas}, n_2^{meas}, n_4^{meas}$, the only possible phonon numbers are Δ_{SAS} plus numbers separated from it by multiples of three. This is consistent with the phonon number states $|3m + j\rangle$ in the conditioned phonon state found in Equation 3.10. Furthermore, the fact that third-order scattering processes can freely add or subtract three phonons without impacting the net photon numbers means that all nonnegative multiples of three are in principle possible for a given conditional phonon state. For example, by

this simple counting argument there should be no state for which $\Delta_{SAS} \pmod{3} = 1$ but the conditioned phonon state superposition does not contain $|7\rangle$.

Of course the counting argument is classical and would not account for quantum interference effects. For example, classically counting up the number of possible outcomes in a Hong-Ou-Mandel interference experiment [44] would lead to a completely inaccurate prediction. But in our case, simply counting up the processes does successfully predict and explain the pattern of number states that are observed in the numerical results.

3.4. Characterizing the conditioned phonon states

As described above, the conditioned phonon states are found numerically to all take the form

$$\sum_{m=0} |3m + (\Delta_{SAS} \pmod{3})\rangle. \quad (3.16)$$

As established in Chapter II, both three-phonon squeezed states and three-component cat states are superpositions of this form. Our numerical results indicate that depending on the measured photon numbers, most of the conditioned phonon states can be very well approximated by either a cat state or a three-phonon squeezed Fock state. In many cases the conditioned phonon state can be well-approximated by both a low-amplitude cat state (i.e., a kitten state) or a weakly three-phonon squeezed Fock state.

In this section, we characterize the conditioned phonon states in terms of their fidelities with cat states and three-phonon squeezed states. We first focus on the conditioned phonon states produced at a relatively long time and high pump power, $t = 0.015$ and $A_0 = A_3 = 60$, and later explore the effects of changing

these parameters. We consider conditioned phonon states produced by measuring a maximum of eight photons in each sideband. With higher photon numbers, too many of the conditioned phonon states have superposition amplitudes that are comparable to the numerical precision used. There are $9^4 = 6561$ conditioned phonon states that can be produced in that way, because there are four optical modes that can each have nine possible numbers of photons (counting zero). We omit three of them because their probability amplitudes are too low, leaving 6558 states to be characterized here. The probability of having more than eight photons in any optical mode at this time and pump power is $\approx 0.6\%$, so limiting our study to eight photons covers the conditioned phonon states that are produced the vast majority of the time.

In Figures 3.27, 3.28, 3.29, and 3.30, located at the end of this chapter, we show the Wigner distributions corresponding to a subset of these 6558 conditioned phonon states. Some of these Wigner distributions resemble the Wigner distributions of squeezed states, and others resemble the Wigner distributions of cat states. Note that all of these Wigner distributions show a three-phase preference, but for many of them this preference is too weak to see by eye.

Our purpose in exploring the extent to which the cat-state and squeezed-state fidelities of the conditioned phonon states can be predicted based on the measured photon numbers is twofold. First, these predictions would allow an experimentalist to, for example, select cat-like states and reject all others. Second, identifying the photon numbers that lead to high fidelities with different states will help us to understand the physical processes that produce the phonon state in the dual-pumped comb.

In the following discussion, the term “squeezing” is always used to mean “three-phonon-squeezing,” and the term “cat state” refers to a cat state of any amplitude—

including very small kitten states that are indistinguishable from certain squeezed states—unless otherwise specified.

3.4.1. Fidelity of conditioned phonon states with three-phonon squeezed states and with cat states

We are interested to what extent the numerically determined states found with particular photon number conditioning can be fit to various forms of model states. This will give further insight into the properties of the actual conditioned phonon states. We computed the fidelity of the conditioned phonon state with a range of different cat states and chose the maximum fidelity as an indicator of how much like a cat state the conditioned phonon state is. The range of different cat states used was obtained by varying the following:

- whether the cat state is composed of number states in the sequence $|0\rangle, |3\rangle, |6\rangle \dots, |1\rangle, |4\rangle, |7\rangle \dots$, or $|2\rangle, |5\rangle, |8\rangle \dots$;
- the overall phase shift of the cat state (it can be zero or π)²;
- the amplitude α of the component coherent states.

Similarly, the fidelity of the conditioned phonon state was computed with a range of different three-phonon squeezed states, and the maximum fidelity is chosen as the indicator of how well the three-phonon squeezed state approximates the conditioned phonon state. The three-phonon squeezed states are generated by the generalized squeezing Hamiltonian in Equation 2.8 in Chapter II with $k = 3$. Time evolution under this Hamiltonian is computed using Padé approximants to avoid the instabilities

²The conditioned phonon states are observed to sometimes have a π phase shift relative to each other in phase space

discussed in Chapter II. (More details about numerical methods are given in Appendix C.) The range of different three-phonon squeezed states was achieved by varying the following:

- the Fock state that undergoes the three-phonon-squeezing process;
- the phase of the three-phonon-squeezing pump (also either 0 or π);
- the three-phonon-squeezing gain, which is the product of the pump amplitude, the coupling coefficient, and the time.

For finding a best fit to a model state, the Fock state that undergoes three-phonon-squeezing was always chosen to be the highest-amplitude number state of the conditioned phonon state, as determined from the numerical solution to the dual-pumped Raman comb problem. For conditioned phonon states in which one amplitude is much higher than all the others, this choice of initial state clearly maximizes the fidelity between the actual state and the model state. For conditioned states in which two or more amplitudes are comparable, it is less clear which initial squeezed state would maximize the fidelity. However, testing with a few of these conditioned states using the second-highest-amplitude number state as the initial state showed that the fidelity obtained that way was consistently lower than the fidelity obtained using the highest-amplitude number state.

We find that the fidelity of the actual conditioned phonon state with a model cat state or a model squeezed state and the cat-state amplitude or squeezing gain of the highest-fidelity model state may depend on four variables parameters:

- Δ_{SAS} ;
- n_1 (the number of photons in the red-anti-Stokes mode);

- n_{total} (the total number of photons measured in all modes);
- n_{max} , where $|n_{max}\rangle$ is the number state in the conditioned phonon state superposition that has the highest amplitude.

Of these four variables, only the first three are directly calculable from the outcomes of the photon number measurements that conditioned the state. It would take an additional measurement to experimentally determine n_{max} . Nevertheless, we show the dependence of the fidelities, cat-state amplitude, and squeezed-state gain on n_{max} because it will help us to give a physical interpretation of the other three variables.

The optimized cat state fidelity for each conditioned phonon state at $t = 0.015$ and $A_0 = A_3 = 60$ is plotted in Figure 3.5 against Δ_{SAS} , n_1 , n_{total} , and n_{max} . There is one point on the plot for each conditioned phonon state. Some states have very similar values and overlap on the plot.

Cat-state fidelity depends strongly on Δ_{SAS} and n_{max} , and less strongly on n_{total} and n_1 . A given value of any of these parameters does not uniquely predict the cat-state fidelity. For instance, the set of states with $\Delta_{SAS} = 3$ encompasses a range of cat-state fidelities. There appears to be a transition between $\Delta_{SAS} = 2$ and $\Delta_{SAS} = 3$, where conditioned states on the lower side of that transition almost all have very high cat-state fidelities, and the cat-state fidelities possible on the higher side of the transition point decrease with increasing Δ_{SAS} . The same is true for n_{max} . Very low cat-state fidelities are possible at the middle of the n_{total} range, but high fidelities are possible for any value of n_{total} . High fidelities are also possible for any value of n_1 , but the minimum possible fidelity decreases as n_1 increases.

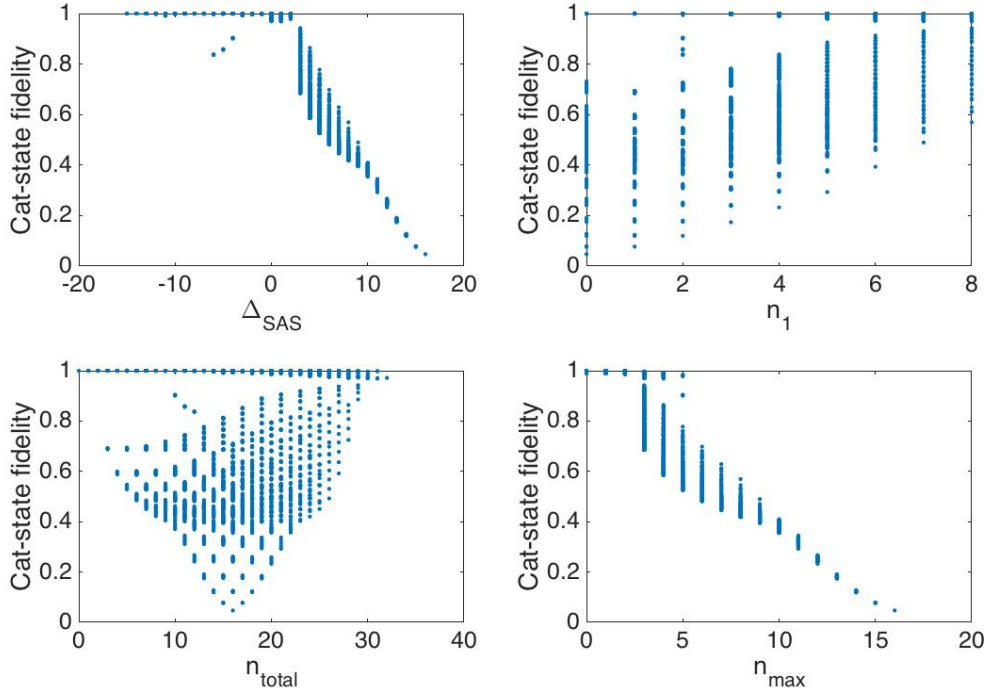


FIGURE 3.5. Optimal cat-state fidelity of all 6558 conditioned phonon states.

In Figure 3.6 we show the fidelity with the optimized model three-phonon squeezed state for each conditioned phonon state plotted against the same four parameters as in Figure 3.5.

Again, the squeezed-state fidelity depends most strongly on Δ_{SAS} and n_{max} . Whereas the cat-state fidelities appeared to decrease as Δ_{SAS} and n_{max} increased, the squeezed-state fidelities increase (at least for positive Δ_{SAS}). For negative values of Δ_{SAS} , however, the squeezed-state fidelities do not change monotonically. It appears that the minimum possible fidelity decreases as Δ_{SAS} becomes more negative, but is increased sharply every three values of Δ_{SAS} , with the net effect that the most negative values of Δ_{SAS} correspond to very high fidelities. There does appear to be a transition between $\Delta_{SAS} = 2, 3$ and $n_{max} = 2, 3$, but one could also interpret the data as showing that $n_{max} = 3, 4, 5$ do not follow the same pattern as the other values.

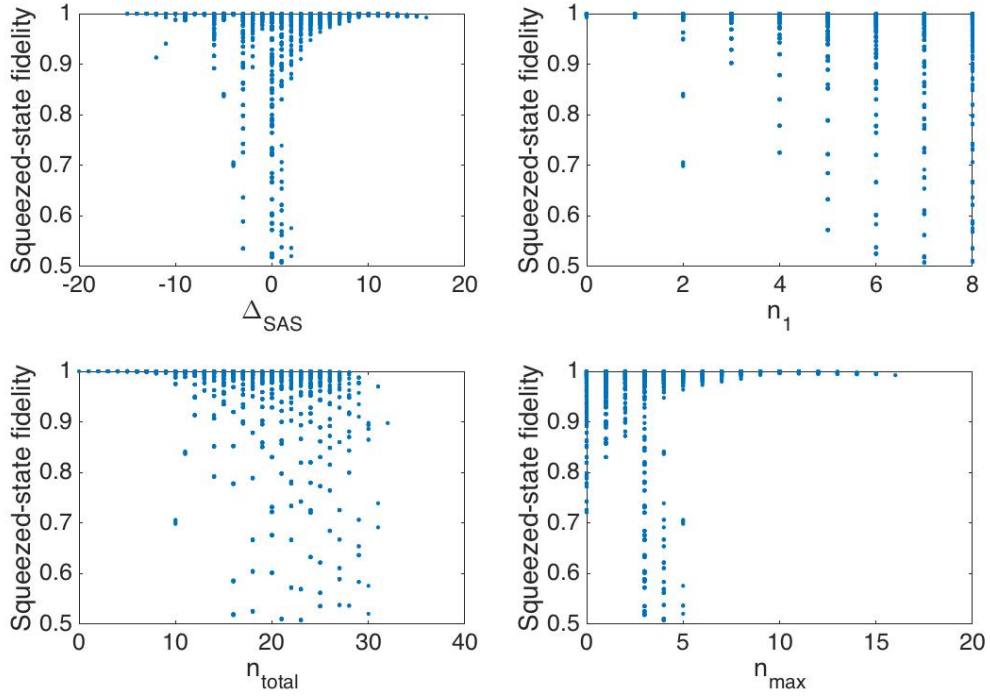


FIGURE 3.6. Optimal squeezed-state fidelity of all 6558 conditioned phonon states.

Roughly, we conclude that squeezed-state fidelity is greatest when Δ_{SAS} and n_{max} are greatest, and cat-state fidelity is greatest when $\Delta_{SAS} < 2$ and lowest when Δ_{SAS} and n_{max} are greatest.

As shown in Figure 3.7, we can divide the 6558 conditioned phonon states into four groups: those having high fidelity with both cat states and squeezed states, those having high fidelity with cat states but not squeezed states, those having high fidelity with squeezed states but not cat states, and those having high fidelity with neither. We now explore each of those categories.

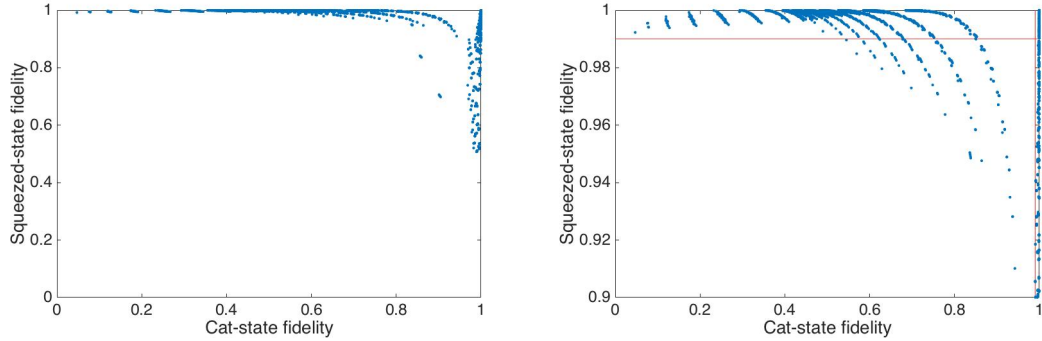


FIGURE 3.7. Optimal squeezed-state fidelity vs optimal cat-state fidelity of all 6558 conditioned phonon states. Left: the axes range from zero fidelity to unit fidelity. Right: we focus on the uppermost region of the vertical axis. The red lines mark 0.99 fidelity. The distinct curves correspond to constant Δ_{SAS} values.

3.4.2. Conditioned phonon states having high fidelity with both cat and squeezed states

More than half of the conditioned states (3389 of 6558) have high fidelity (over 0.99) with both cat and three-phonon squeezed states. For all conditioned states in this set, $n_{max} = 0, 1$ or 2 , and $\Delta_{SAS} = 0, 1, 2$ or $\Delta_{SAS} < 0$. For all these states, $n_{max} = \Delta_{SAS} \pmod{3}$.

As discussed previously, weakly squeezed $|0\rangle, |1\rangle$ and $|2\rangle$ states do indeed have high fidelity with low-amplitude cat states, simply because both types of state have near-unit amplitude in either $|0\rangle, |1\rangle$ and $|2\rangle$. Perhaps surprisingly, this set of conditioned states also includes states with substantial amplitude in more than one number state. These are conditioned states that are well-approximated by both a relatively strongly squeezed state and a not-too-low-amplitude cat state. Figure 3.8 shows a plot of each of these 3389 conditioned phonon states in terms of the amplitude of the cat state that best approximates it and the gain of the squeezed state that best approximates it.

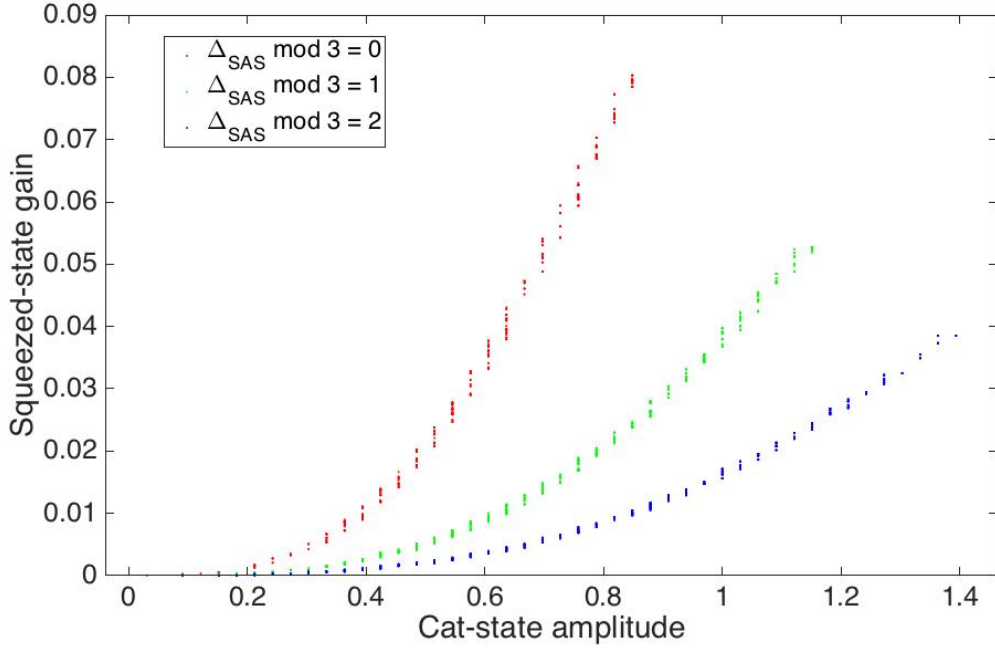


FIGURE 3.8. Optimal cat-state amplitude and squeezing gain for states that have high amplitude with both cat and squeezed states.

The larger the amplitude of the optimal cat state, the larger the gain of the optimal squeezed state. The optimal squeezing gain appears to initially grow exponentially with the optimal cat amplitude and then to grow linearly. In either regime, the rates of growth depend on Δ_{SAS} . The highest-amplitude cat state that has maximal fidelity with any conditioned state in this set is only $|\alpha| = 1.394$, which under the definition proposed by [35] qualifies as a kitten state, albeit a fairly large one. It is not possible to obtain a conditioned phonon state that has high fidelity with a bigger cat state and also with a three-phonon-squeezed state.

The four variables Δ_{SAS} , n_1 , n_{total} , and n_{max} do not strongly predict the squeezing gain or cat-state amplitude of the highest-fidelity cat and squeezed states in this regime. The highest squeezing gains are possible for $n_{max} = 0$, and the highest cat amplitudes are possible when $n_{total} \geq 16$. The dependence of the squeezing gain and

cat amplitude on Δ_{SAS} seems to be periodic in every three values of Δ_{SAS} . Figures 3.9 and 3.10 show the dependence of the cat-state amplitude and squeezed-state gain on these four variables.

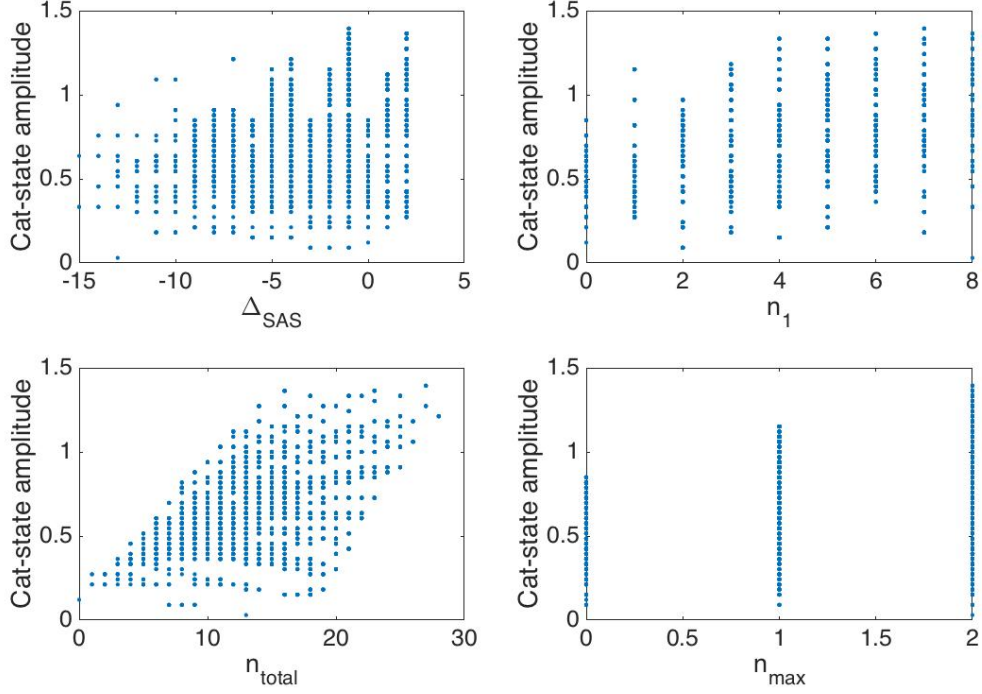


FIGURE 3.9. Optimal cat-state amplitude of conditioned phonon states having high fidelity with both cat states and squeezed states.

3.4.3. Conditioned phonon states having high fidelity with cat states only

Next we consider conditioned phonon states that have at least 0.99 fidelity with cat states but less than 0.99 fidelity with squeezed states. There are 912 conditioned phonon states that have over 0.99 fidelity with a cat state and less than 0.99 fidelity with a squeezed state. They all have $\Delta_{SAS} \leq 2$. For these states, it is not always

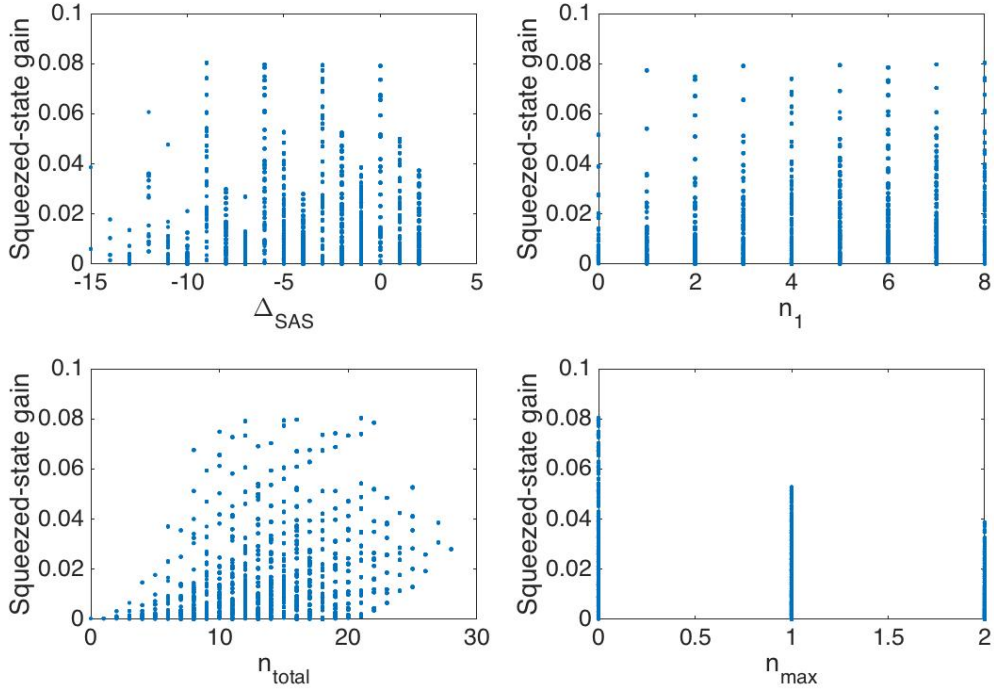


FIGURE 3.10. Optimal squeezed-state gain of conditioned phonon states having high fidelity with both cat states and squeezed states.

the case that $n_{max} = \Delta_{SAS} \pmod{3}$. In Figure 3.11 we plot the amplitude of the highest-fidelity cat state against Δ_{SAS} , n_1 , n_{total} , and n_{max} .

For any particular value of any one of the four variables, there is a range of cat-state amplitudes corresponding to high fidelity with that state. In some applications it may be desirable to obtain the highest-amplitude cat state possible. These would correspond to $\Delta_{SAS} = \pm 1, 2$ or to $n_{max} = 1, 2, 4$. States with these Δ_{SAS} and cat-state fidelity at least 0.99 and squeezed-state fidelity less than 0.99 are produced with probability 1.215×10^{-5} . Given a cat-like state with $\Delta_{SAS} = \pm 1, 2$, the probability that that state has a high amplitude ($|\alpha| \geq 1.5$)³ is 0.123. It appears there is no simple way to guarantee that the conditioned phonon state will be a high-amplitude cat state

³This is the threshold proposed in [35] for a true cat state, rather than a kitten state.

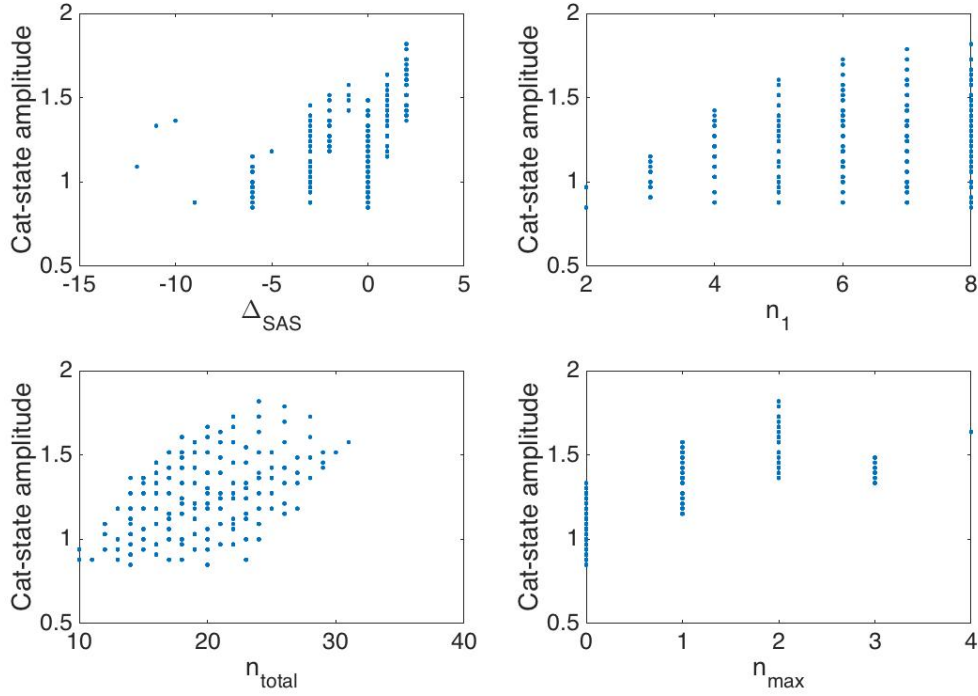


FIGURE 3.11. Optimal cat-state amplitude of conditioned phonon states having high fidelity with cat states only.

based only a single number like Δ_{SAS} . (In principle a device could be programmed to recognize the exact four-photon-number combinations that correspond to high-amplitude cat states, however.)

3.4.4. Conditioned phonon states having high fidelity with squeezed states only

There are 1944 conditioned phonon states that have over 0.99 fidelity with three-phonon-squeezed states and less than 0.99 fidelity with cat states. These states all have $\Delta_{SAS} \geq 3$ and $\Delta_{SAS} = n_{max}$. The squeezing gain corresponding to the highest-fidelity squeezed state for each conditioned state is plotted against Δ_{SAS} , n_1 , n_{total} , and n_{max} in Figure 3.12.

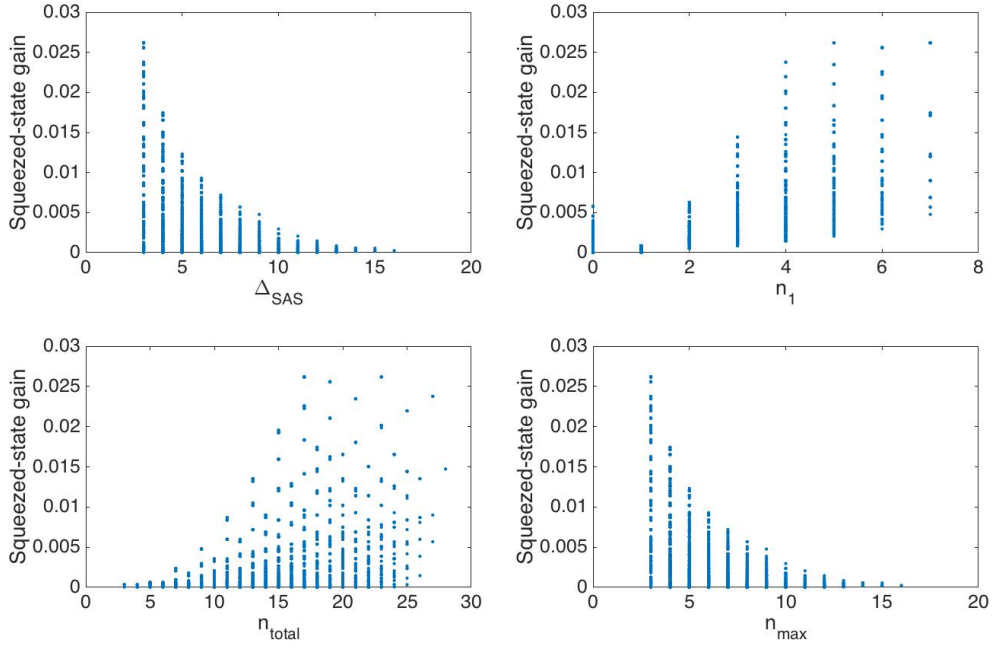


FIGURE 3.12. Optimal squeezed-state gain of conditioned phonon states having high fidelity with squeezed states only.

Again, there is no reliable way to use a single one of these four variables to guarantee a state with strong squeezing. If, on the other hand, the goal were to guarantee a Fock state, it would be easy to achieve. Very weakly squeezed states are extremely similar to Fock states (which correspond to zero squeezing gain), and a very small squeezing gain can be guaranteed by choosing a high Δ_{SAS} , a very low n_{total} , or $n_1 = 1$.

3.4.5. Conditioned states having high fidelity with neither cat or three-phonon-squeezed states

There are 313 states that do not have at least 0.99 fidelity with either cat states or three-phonon-squeezed states. They are represented in Figure 3.13, plotted against

their cat-state fidelity and their squeezed-state fidelity. As indicated in the legend, different shapes and colors indicate different values of Δ_{SAS} .

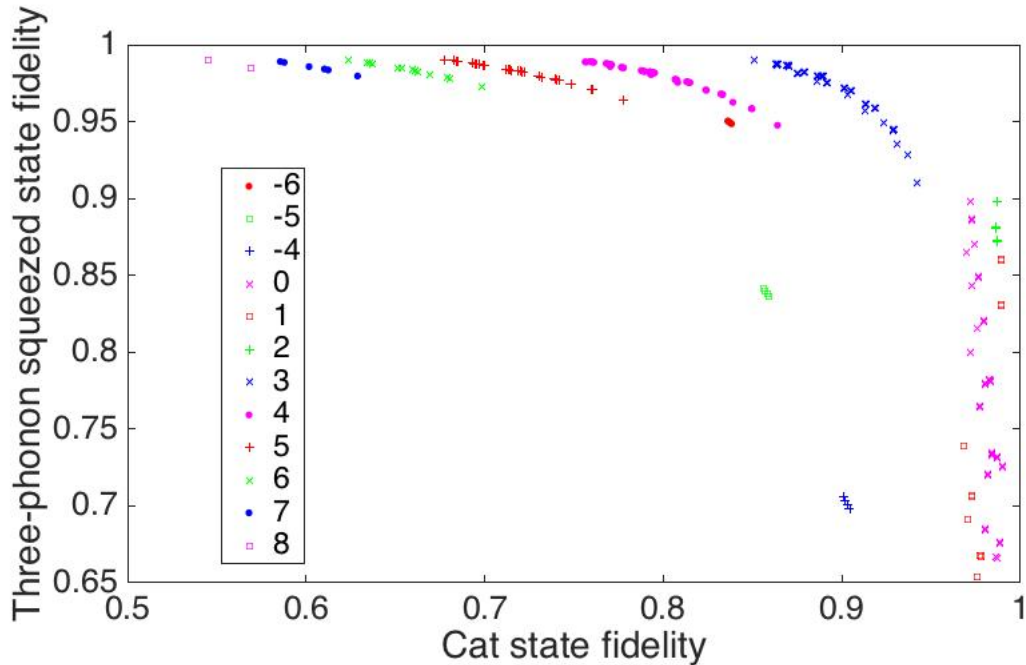


FIGURE 3.13. Maximal cat-state fidelity and squeezed-state fidelity for conditioned phonon states that do not have at least 0.99 fidelity with either type of state. The legend indicates different values of Δ_{SAS} .

Here we make some brief observations about these “intermediate” states.

- Not all possible values of Δ_{SAS} are found in the set of intermediate states. No Δ_{SAS} with absolute value greater than eight is here, and $\Delta_{SAS} = -1, -2, -3$ are also absent. The number of photons in each optical mode can range from 0 to 8, except for the red-anti-Stokes sideband, which has at least 2 photons for each intermediate state.
- The states for which $\Delta_{SAS} = 3, 4, 5, 6, 7, 8$ form distinct curves on the plot in Figure 3.13. The states for each Δ_{SAS} in this range cover a range of cat state fidelities and a smaller range of squeezed state fidelities. The cat-state fidelities

are lower for higher Δ_{SAS} , and the minimum squeezed state fidelity is higher Δ_{SAS} . As can be seen back on Figure 3.7, these figures continue into the 0.99 squeezed-state fidelity range, and the analogous curves for higher Δ_{SAS} are located entirely within that range. For a given value of Δ_{SAS} in this group, the cat- and squeezed-state fidelities are determined by the total photon number and the number of red-anti-Stokes photons, as shown for $\Delta_{SAS} = 3$ in Figure 3.14.

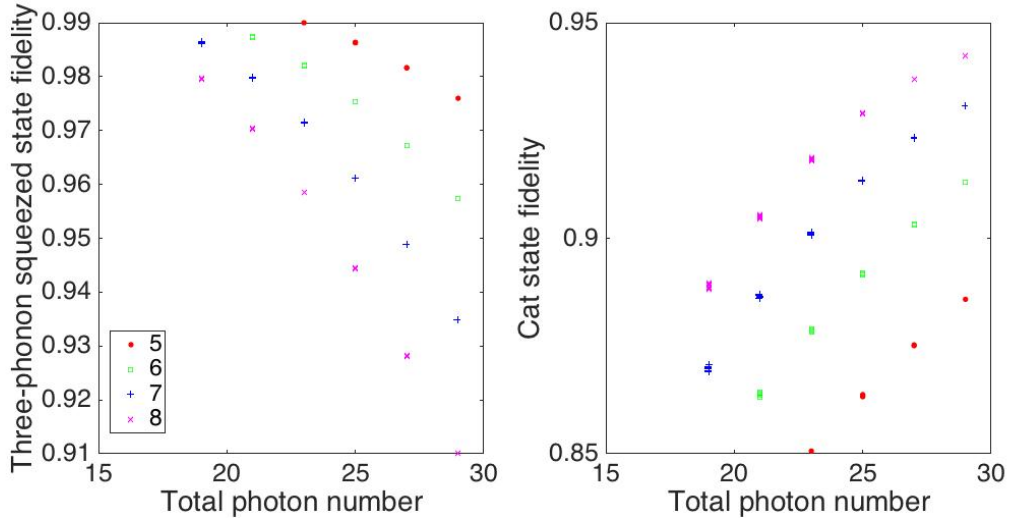


FIGURE 3.14. Dependence of cat-state fidelity and squeezed-state fidelity on total photon number and red-anti-Stokes photon number for intermediate conditioned phonon states where $\Delta_{SAS} = 3$. The legend indicates different values of n_1 .

- The states for which $\Delta_{SAS} = 0, 1, 2$ all have at least 0.95 cat-state fidelity. All but 18 of these 145 states have $n_{max} \neq \Delta_{SAS}$. The other 18 all have cat-state fidelity of at least 0.986. Some of these 145 states have a fairly low squeezed-state fidelity, as low as 0.65. Finally, there are several states with $\Delta_{SAS} = -4, -5, -6$. Each of those subsets are clustered together in Figure 3.13 with nearly the same cat- and squeezed-state fidelities. For all these states, the number of red-anti-Stokes photons n_1 is 2, the number of photons in the

two Stokes modes n_2 and n_{-1} is 0,1,2, or 3, and the number of photons in the blue-anti-Stokes mode n_4 is 5,6, or 7. These states are the only ones in the entire set of 6558 conditioned states with up to eight photons per mode that have $\Delta_{SAS} < -3$ and a highest-amplitude state greater than $|2\rangle$.

3.4.6. Interpretation of Δ_{SAS} and other parameters

As shown above, the number Δ_{SAS} appears to determine the range of model cat-state fidelities and squeezed-state fidelities that a given conditioned phonon state will have. Specifically, if a conditioned phonon state has $\Delta_{SAS} > 2$, then it very likely has high squeezed-state fidelity and low cat-state fidelity. (There is a small chance that it will be an intermediate state, in which case its squeezed-state fidelity can be as low as 0.90 but can approach 0.99.) A conditioned phonon state with $\Delta_{SAS} \leq 2$ almost always has high cat-state fidelity and probably has high squeezed-state fidelity as well. (Again, there is a relatively small number of intermediate states with these Δ_{SAS} as well.)

As discussed in the classical counting argument, no conditioned phonon state is identically a Fock state with amplitude all in one number state. They all have some amplitude in the number states corresponding to $\Delta_{SAS} + 3, 6, 9 \dots$ and $\Delta_{SAS} - 3, 6, 9 \dots$. The amplitude in these other states determines whether a conditioned phonon state has high fidelity with cat states, squeezed states, or both. It can be predicted by Δ_{SAS} to some extent—or more precisely, the conditioned phonon states with a particular value of Δ_{SAS} have a range of cat-state and squeezed-state fidelities. The reason is that the value of Δ_{SAS} provides some insight into the number of second- and third-order processes that are likely to have produced the measured photon numbers.

Third-order scattering is very much like three-phonon-squeezing, because it creates or annihilates three phonons with no net effect to the optical modes. A conditioned phonon state created by measuring photon numbers that were created exclusively by first-order scattering plus third-order scattering is therefore very similar to a squeezed state. In particular, if the phonon number state that would result from first-order scattering alone is $|k\rangle$, then the conditioned phonon state would have high fidelity with a squeezed $|k\rangle$ number state. The squeezed state has very high amplitude in the $|k\rangle$ state and much lower amplitude in $|k \pm 3, 6, 9 \dots\rangle$. When second-order scattering is possible as well, it changes the proportion of these amplitudes. Each of the n_1 photons in the red anti-Stokes mode could have been produced by second-order Stokes scattering rather than first-order anti-Stokes scattering. As described in the classical counting argument, a single second-order Stokes process contributes to the $|k + 3\rangle$ state amplitude rather than the $|k\rangle$ amplitude, and m second-order Stokes processes contribute to the $|k + 3m\rangle$ states. If the probability of one or more second-order Stokes processes is not very low, then the amplitude of $|k + 3\rangle$ will be disproportionately large relative to a squeezed state. The squeezed-state fidelity is thus lower. In some cases, the cat-state fidelity is higher, but in some cases, the cat-state fidelity is also low and the conditioned phonon state is one of the “intermediate” states described above. Specifically, if the highest-amplitude number state in the conditioned phonon state is $|0\rangle, |1\rangle$, or $|2\rangle$, the cat state fidelity is very high, but otherwise it is usually low. This is due to the phonon-number probability distribution of a cat-state. Recall from Chapter II that a three-component cat state has either the form

$$\begin{aligned}
|\psi\rangle &= \frac{\exp(-|\alpha|^2/2)}{\sqrt{3}} \sum_{n=0}^{\infty} \frac{\alpha^n}{\sqrt{n!}} |n\rangle \\
&+ \frac{\exp(-|\alpha|^2/2)}{\sqrt{3}} \sum_{n=0}^{\infty} \frac{\alpha^n \exp(in2\pi/3)}{\sqrt{n!}} |n\rangle \\
&+ \frac{\exp(-|\alpha|^2/2)}{\sqrt{3}} \sum_{n=0}^{\infty} \frac{\alpha^n \exp(-in2\pi/3)}{\sqrt{n!}} |n\rangle \\
&= \frac{\exp(-|\alpha|^2/2)}{\sqrt{3}} \sum_{n=0}^{\infty} \frac{\alpha^n (1 + \exp(in2\pi/3) + \exp(-in2\pi/3))}{\sqrt{n!}} |n\rangle,
\end{aligned} \tag{3.17}$$

or a phase-shifted version of it, and that due to cancellation in the phases, the only nonzero-amplitude states in the superposition are either $|0\rangle, |3\rangle, |6\rangle\dots$ or $|1\rangle, |4\rangle, |7\rangle\dots$ or $|2\rangle, |5\rangle, |8\rangle\dots$ depending on which of these forms the cat state takes. For any cat state with high enough α that its highest-amplitude state is a relatively high $|k\rangle$, the states $|k \pm 3\rangle$ also have relatively high amplitude, because for that value of α , $\alpha^k/\sqrt{k!}$ is not that different from $\alpha^{k\pm 3}/\sqrt{(k \pm 3)!}$. In contrast, for small α , the first number state is dominant. As shown in Figure 3.15, the ratio of the second-lowest number state amplitude to that of the lowest number state is much less than unity for $\alpha \approx 1$ or even greater, depending on which type of cat state it is.

To summarize, whether a conditioned phonon state has high fidelity with a model squeezed state depends on how much second-order Stokes scattering is probable given the measured photon numbers, and whether the state has high fidelity with a model cat state depends not only on the amount of second-order Stokes scattering but on which number state in the superposition has the highest amplitude.

The number of second-order Stokes processes that are likely to have occurred can be partly deduced from Δ_{SAS}, n_1 , and n_{total} , which is why these are three of the four variables studied in the previous section. (The fourth variable is n_{max} , where

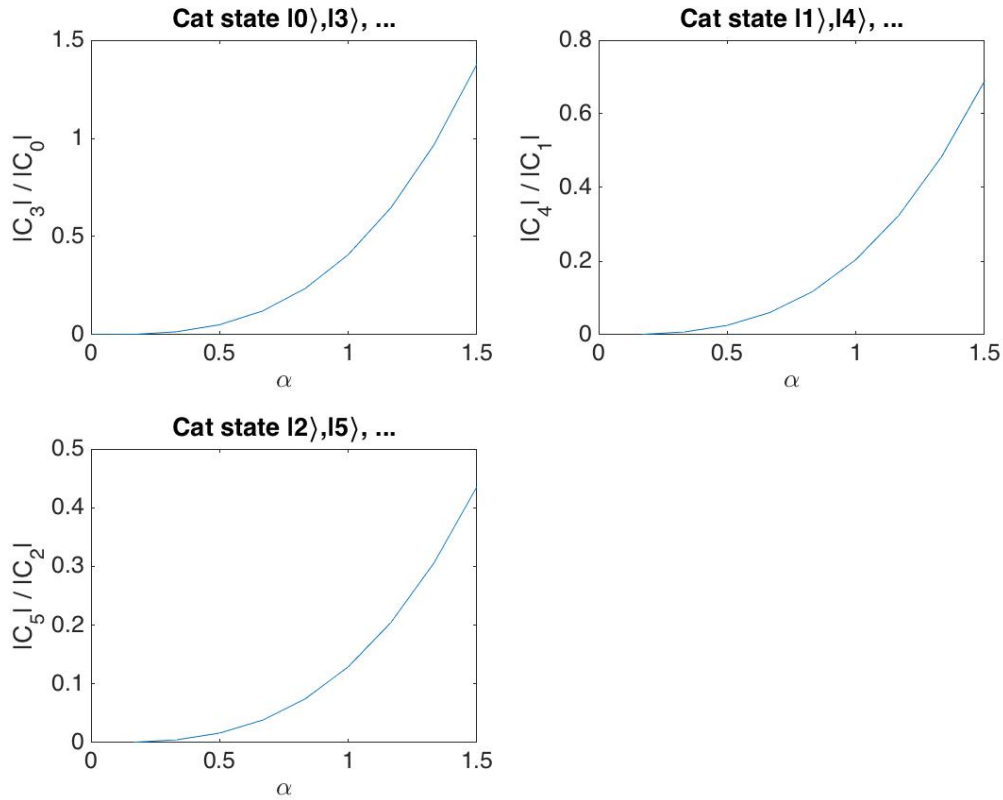


FIGURE 3.15. Ratio between second and first number state amplitudes in the three varieties of three-component cat states.

$|n_{max}\rangle$ is the highest-amplitude state in the conditioned phonon state, the significance of which has just been explained.) Because every photon produced by second-order Stokes scattering has to end up in the red-anti-Stokes mode, n_1 is the maximum number of second-order Stokes processes possible. As discussed previously, Δ_{SAS} is the difference between the number of photons in the Stokes modes and the number of photons in the anti-Stokes modes. This number is clearly not independent of n_1 . For very high Δ_{SAS} , the total number of anti-Stokes photons must be low and therefore n_1 must be low. For example, when $\Delta_{SAS} = 15$, that means that there are 15 more Stokes photons than there are anti-Stokes photons. There can only be eight photons in each mode, however, so the maximum number of Stokes photons is 16, and therefore

the number of anti-Stokes photons can be no more than one. The lower Δ_{SAS} is (as long as it is nonnegative), the broader the range of possible n_1 values. This is why high squeezing fidelity is possible for all nonnegative Δ_{SAS} , but the range of possible fidelities includes lower and lower fidelities for lower Δ_{SAS} .

The correlation with n_1 is not the only significance of Δ_{SAS} , however. If Δ_{SAS} is negative, then the total number of Stokes photons is less than the total number of anti-Stokes photons, and so first-order scattering alone cannot create enough phonons to account for the photon numbers. Therefore each phonon number state in the conditioned phonon state superposition must be created by some combination of first-, second-, and third-order scattering. For this reason, $|n_{max}\rangle$ for these states is usually, but not always, $|\Delta_{SAS} \pmod{3}\rangle$. The number of possible second-order Stokes scattering processes increases as Δ_{SAS} becomes more negative. By the argument outlined above, we might expect that to result in low squeezed-state fidelities for very negative Δ_{SAS} . In fact, we see in Figure 3.6 that the squeezing fidelity does not monotonically increase as Δ_{SAS} gets more negative—but for the most negative Δ_{SAS} values, the squeezed-state fidelity is very high. Both of these observations are explained by the fact that the more negative Δ_{SAS} is, the greater the number of higher-order processes that are required to produce the state at all. For example, when $\Delta_{SAS} = -15$, at least five higher-order processes are required to produce any phonon number state. Additional second-order processes do increase the amplitude of the $|n_{max} + 3\rangle$ state, but the probability of additional processes beyond the necessary five is so low that the ratio of the amplitudes of $|n_{max} + 3\rangle$ and $|n_{max}\rangle$ are still consistent with a squeezed state. The relative probability of $|n_{max} + 3\rangle$ to $|n_{max}\rangle$ decreases with each additional required higher-order process. Each higher-order process provides three phonons, so the number of required processes increases only every three negative

values of Δ_{SAS} . This is why the possible squeezing fidelities for negative Δ_{SAS} can be interpreted as tending to decrease but being drastically increased every three values.

As described above, a low-amplitude cat state (with α as high as ≈ 1.3 in some cases) has $n_{max} = 0, 1, 2$ and resembles a squeezed state. For this reason, $\Delta_{SAS} \leq 2$ almost always predicts high cat-state fidelity. Most of the exceptions to this rule are intermediate states in which $n_{max} \neq \Delta_{SAS}$. No state with $\Delta_{SAS} > 2$ has high cat-state fidelity, because these states generally have $n_{max} > 2$ and not enough second-order Stokes scattering to constitute a cat state at those phonon numbers.

Among states with high cat-state fidelities, high fidelities with the greatest α amplitude-states are possible when $\Delta_{SAS} \pmod{3} = 2$. As shown in Figure 3.15, this is because the three-component cat states that can achieve the necessary amplitude distribution at highest α are those that are superpositions of $|2\rangle, |5\rangle, |8\rangle$ etc. The highest cat-state amplitudes also tend to occur for high n_1, n_{total} , and Δ_{SAS} , because high values of those numbers are signifiers of high amounts of second-order Stokes scattering. For states with high squeezed-state fidelities, the maximum possible squeezing gain decreases monotonically from $\Delta_{SAS} = 3$ on up. This is because the probability of third-order Stokes scattering decreases as Δ_{SAS} increases. Consider for example a state in which there are eight blue-Stokes photons and zero red-anti-Stokes photons. The overall probability of having eight first-order Stokes processes and one or more third-order Stokes processes is relatively low, because it is improbable that the third-order scattered photons would all have left the blue pump and been deposited directly into the red pump with zero of them staying in the red-anti-Stokes mode. The low amplitude of the phonon number state $|\Delta_{SAS} + 3\rangle$ leads to high fidelity only with low-gain squeezed states.

The significance of n_{total} is primarily its correlation with Δ_{SAS} . For up to eight photons per optical mode, n_{total} is between 0 and 32. At the middle of this range, the number of possible Δ_{SAS} values is greatest, and that number decreases at the maximum and minimum of n_{total} . That's why the lowest cat-state fidelities are found near $n_{total} \approx 14 - 18$. The minimum squeezed-state fidelities, in contrast, decrease as n_{total} increases toward the ≈ 16 and then never increases again. Their failure to increase is a consequence of the relatively low squeezed-state fidelities that are possible for $\Delta_{SAS} = -3, 1, 2$.

3.4.7. Phase probability distribution of conditioned phonon states

In some contexts, including the creation of a partially phase-stable comb, it is less useful to know whether a conditioned phonon state is more like a squeezed state or a cat state and more useful to know the strength of the threefold-symmetric dependence of the amplitude of the phonon mode on its phase. Qualitatively, this is akin to asking how distinct the triangular shape of the conditioned phonon state in phase space is. As shown in Figure 3.16, the strength of the three-phase dependence varies significantly from state to state. Physically, it corresponds to how strongly correlated the phonon phase is to the three preferred values of 0 and $\pm 2\pi/3$.

The strength of the correlation between the phonon-mode phase and the three preferred values is naturally characterized by the phase probability distribution obtained from the positive operator-valued measure constructed with the canonical phase states [45]:

$$P(\theta) = \frac{1}{2\pi} \left| \sum_{n=0}^{\infty} \langle \psi | n \rangle \exp(in\theta) \right|^2 \quad (3.18)$$

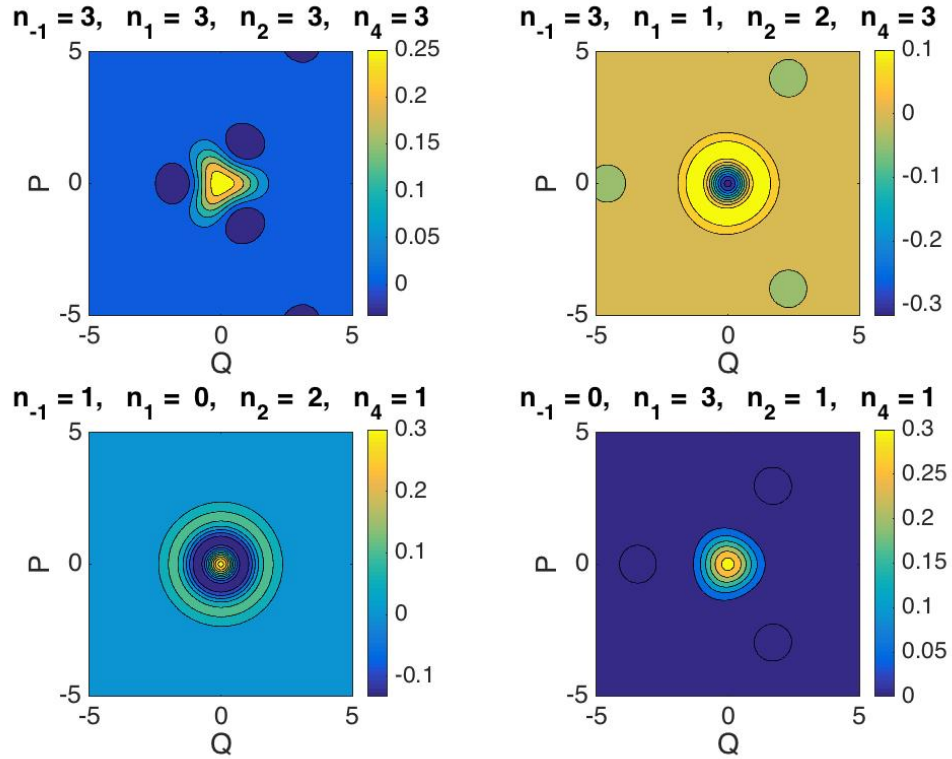


FIGURE 3.16. Wigner distributions for some example conditioned phonon states.

The phase distributions for each of the four conditioned states from Figure 3.16 are shown in Figure 3.17. For each of these distributions, the function $P(\theta)$ has three maxima and three minima, reflecting the three phase-space directions of growth at the preferred phases 0 and $\pm 2\pi/3$. (In the conditioned state obtained by measuring $n_{-1} = 1, n_1 = 0, n_2 = 2, n_4 = 1$, there is an overall phase shift of π and so the directions of growth are instead $\pi, \pi \pm 2\pi/3$.) The different ranges needed on the vertical axes to show the four distributions indicate the different modulation depths of the curves, reflecting the different distinctness of their triangular shapes in Figure 3.16.

For the conditioned states shown in Figure 3.16, the probability that the outcome of a phase measurement would be one of the three preferred phases is higher than

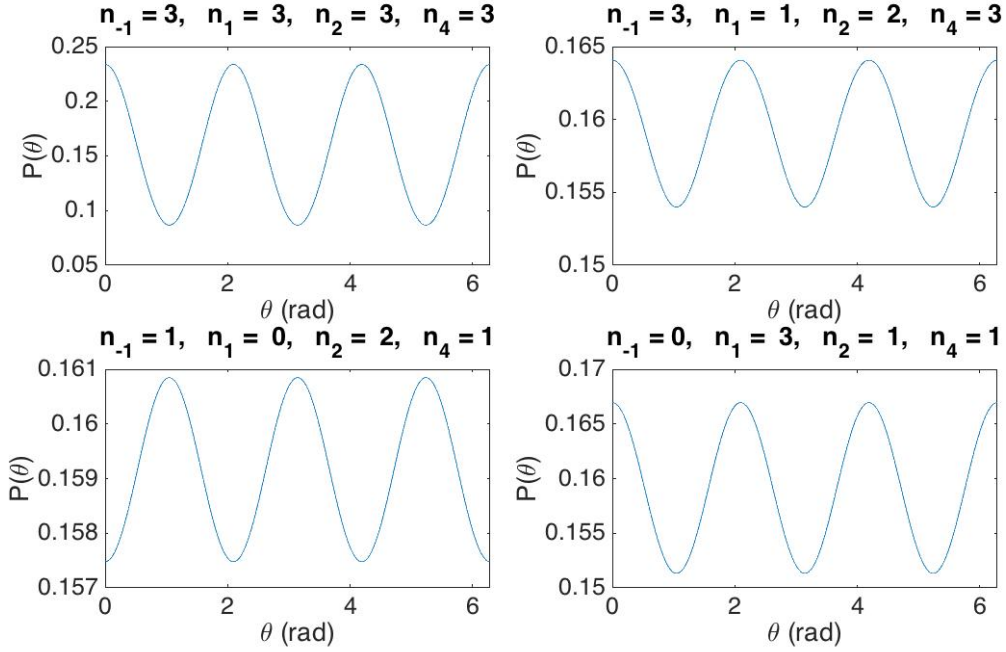


FIGURE 3.17. Canonical phase probability distributions for some example conditioned phonon states.

the probability that it would not be, but the probability that it would not be is still substantial. For some other states, however, $P(\theta)$ is even more sharply peaked at 0 and $\pm 2\pi/3$. An example is the conditioned phonon state created by measuring 14 photons in each sideband. Its Wigner distribution and phase probability distribution are shown in Figure 3.18.

In this phase probability distribution, the probability of phases between the preferred ones at 0 and $\pm 2\pi/3$ actually goes to zero, and the peaks at the preferred phases are narrower. We can guess this from the Wigner distribution, where the alternating positive and negative fringes along the anti-preferred phases indicate that the total amplitude along those directions will cancel, and the peaks at the preferred phases indicate increased amplitude. In general, this type of phase probability distribution appears to happen primarily for conditioned states that are comparable

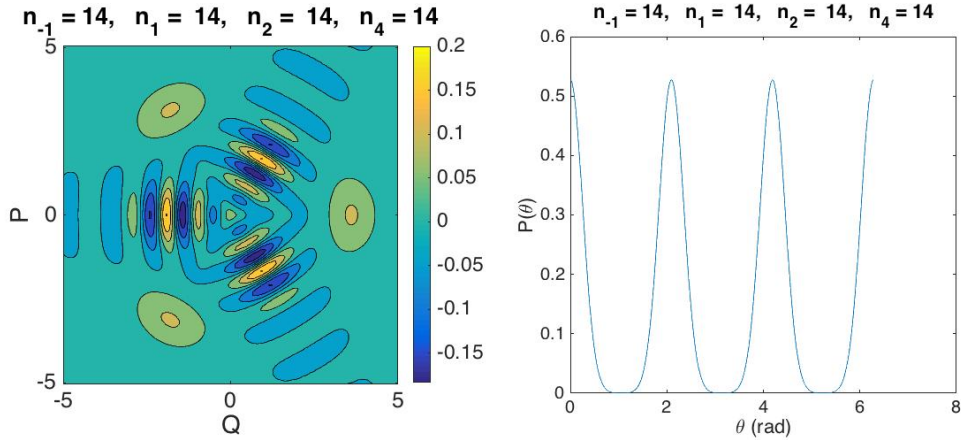


FIGURE 3.18. Wigner distribution and canonical phase probability distribution for the conditioned phonon state corresponding to 14 photons in each optical mode.

to large-amplitude cat states. (The one in Figure 3.18 has 0.972 fidelity with a cat state with $\alpha = 2.557$.) The probability that the outcome of a phase measurement on these states will be very close to the preferred phase values is very high.

3.5. Effects of varied pump amplitudes

In the previous section, we considered the behavior of the dual-pumped Raman comb at $t = 0.015$ and $A_0 = A_3 = 60$. Now we consider the effects of varying pump amplitudes while keeping the time fixed. As is evident in Equation 3.1, not all terms of the Hamiltonian are scaled by a change in the pump amplitudes. The term that couples the red-anti-Stokes mode to the blue-Stokes mode is unaffected by that change. This is an interesting contrast to the generalized squeezing Hamiltonian discussed in Chapter II, which scales each term equally with pump amplitude in the same way they scale with time.

In order to compare the set of conditioned phonon states at several different pump amplitudes, we focus on cat-state fidelity, the cat-state amplitude of cat-like states, and the probability to obtain a cat state with amplitude $\alpha \geq 1.5$. We count

a conditioned phonon state as a cat state if the conditioned state has at least 0.99 fidelity with the desired state.

The first case we consider is the original one in the previous section, where $t = 0.015$ and $A_0 = A_3 = 60$. For now we keep the time fixed at $t = 0.015$ for all cases. Again we consider no more than eight photons per mode.

The second case we consider is reducing both pump amplitudes to $A_0 = A_3 = 20$. The probability distributions for the phonon and photon numbers are shown in Figure 3.19. The average phonon and photon numbers are much lower than in the original $A_0 = A_3 = 60$ case at the same time.

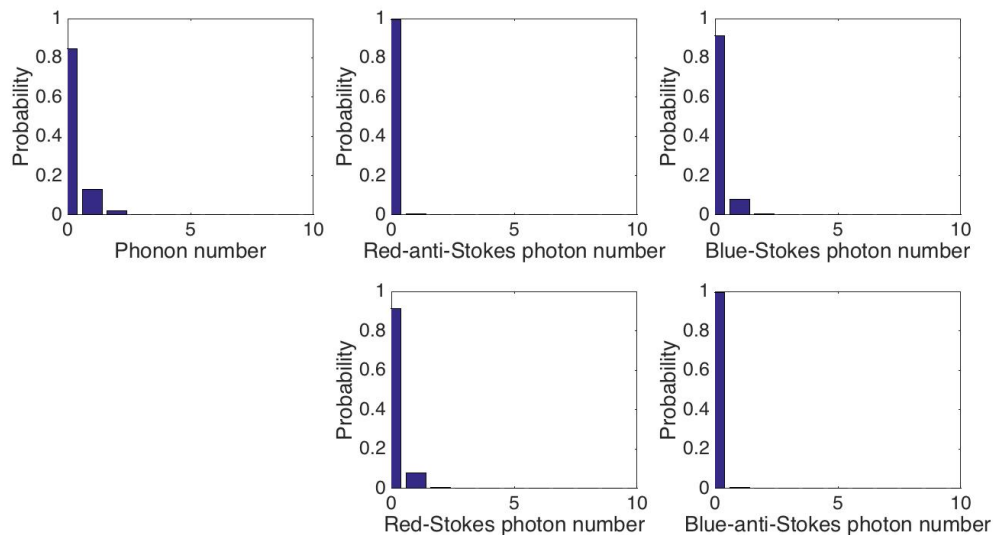


FIGURE 3.19. Probability distributions of photon and phonon number at time $t = 0.015$ with pump amplitudes $A_0 = A_3 = 20$.

In the third case, the red pump is weak but the blue pump is strong ($A_0 = 20, A_3 = 60$). The fourth and final case is the opposite, with a strong red pump and weak blue pump ($A_0 = 60, A_3 = 20$). The probability distributions for these two cases are shown in Figures 3.20 and 3.21.

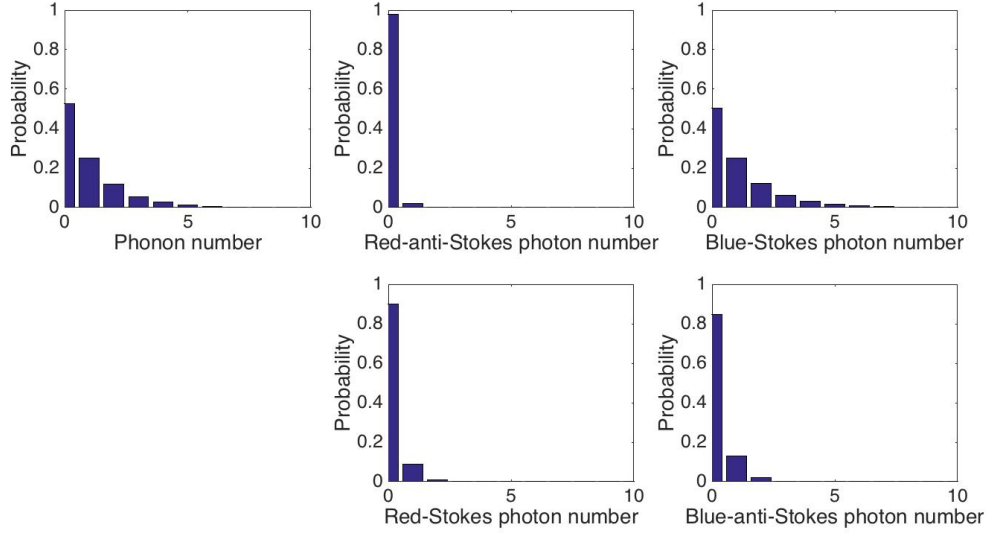


FIGURE 3.20. Probability distributions of photon and phonon number at time $t = 0.015$ with pump amplitudes $A_0 = 20$, $A_3 = 60$.

In Figure 3.22, we show the cat-state fidelity for conditioned phonon states in each case plotted against Δ_{SAS} . We also show the cat-state amplitude for conditioned phonon states that have at least 0.99 fidelity with cat states. (These states may also have high fidelities with squeezed states.)

Let us first compare the case where the pumps are equal and strong (top row of Figure 3.22) to the case where the pumps are equal and weak (second row of Figure 3.22). For both these cases, 0.99 cat-state fidelity occurs only from $\Delta_{SAS} < 3$, but the cat-state fidelities at slightly higher Δ_{SAS} are greater when the pumps are weak than when they are strong. Additionally, for the highest Δ_{SAS} values, the weak pumps produce higher cat-state fidelities than the strong pumps. We attribute these differences to the fact that decreasing the pump amplitudes essentially decreases the probability of second-order scattering relative to first-order scattering. This effect can be seen in the Hamiltonian in Equation 3.1, in which every term is proportional to a pump amplitude except for the term that couples the blue-Stokes and red-anti-Stokes

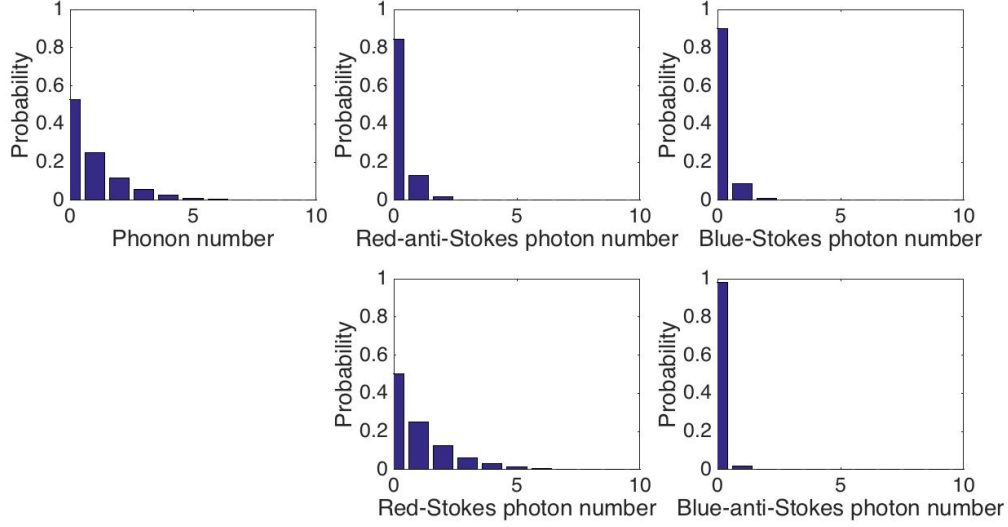


FIGURE 3.21. Probability distributions of photon and phonon number at time $t = 0.015$ with pump amplitudes $A_0 = 60$, $A_3 = 20$.

modes. The smaller the difference in probability between second- and first-order scattering, the more cat-like the conditioned phonon states will be. As an illustration, we show in Figures 3.23, 3.24, 3.25, and 3.26 the Wigner distributions of the phonon state conditioned on measuring three photons in each optical mode in each of the four cases considered here.

From the Wigner distributions in Figures 3.23, 3.24, 3.25, and 3.26 as well as the plots in Figure 3.22, we observe that the cat-state behavior of the case where both pumps are strong is relatively similar to the case where the red pump is strong and the blue pump is weak, whereas the case where both pumps are weak is more similar to the case where the red pump is weak and blue pump is strong. We infer that the strong-red-pump behavior resembles the strong-equal-pump behavior because a strong red pump and weak blue pump together reduce the ratio of second-order Stokes scattering to first-order scattering. The strong red pump increases first-order scattering, and the weak blue pump tends to reduce it. But all photons that undergo second-order Stokes

	Probability of any cat state	Probability of cat state with $ \alpha \geq 1.5$
Strong equal pumps	0.7637	1.4890×10^{-6}
Weak equal pumps	0.9965	1.4170×10^{-12}
Weak red, strong blue	0.8938	5.2919×10^{-7}
Strong red, weak blue	0.8937	1.9278×10^{-16}

TABLE 3.1. Probabilities of obtaining phonon cat states from dual-pumped combs with different pump amplitudes

scattering must originate in the blue pump, so fewer blue pump photons means less second-order Stokes scattering. The result is a relatively small amount of second-order scattering compared to first-order scattering. The weak-red-pump behavior resembles the weak-equal-pump behavior because the strong blue pump increases both first- and second-order scattering, but the weak red pump reduces first-order scattering, leading to a somewhat high ratio of second- to first-order scattering.

We have explained the possibility of high-fidelity high-amplitude cat states in terms of the relative probabilities of first-order scattering and second-order Stokes scattering. The overall probability of high-amplitude cat states, however, depends primarily on the blue pump amplitude, as shown in Table 3.1. Using a blue pump of amplitude $A_3 = 20$ rather than $A_3 = 60$ reduces the overall probability of a high-amplitude cat state by many orders of magnitude.

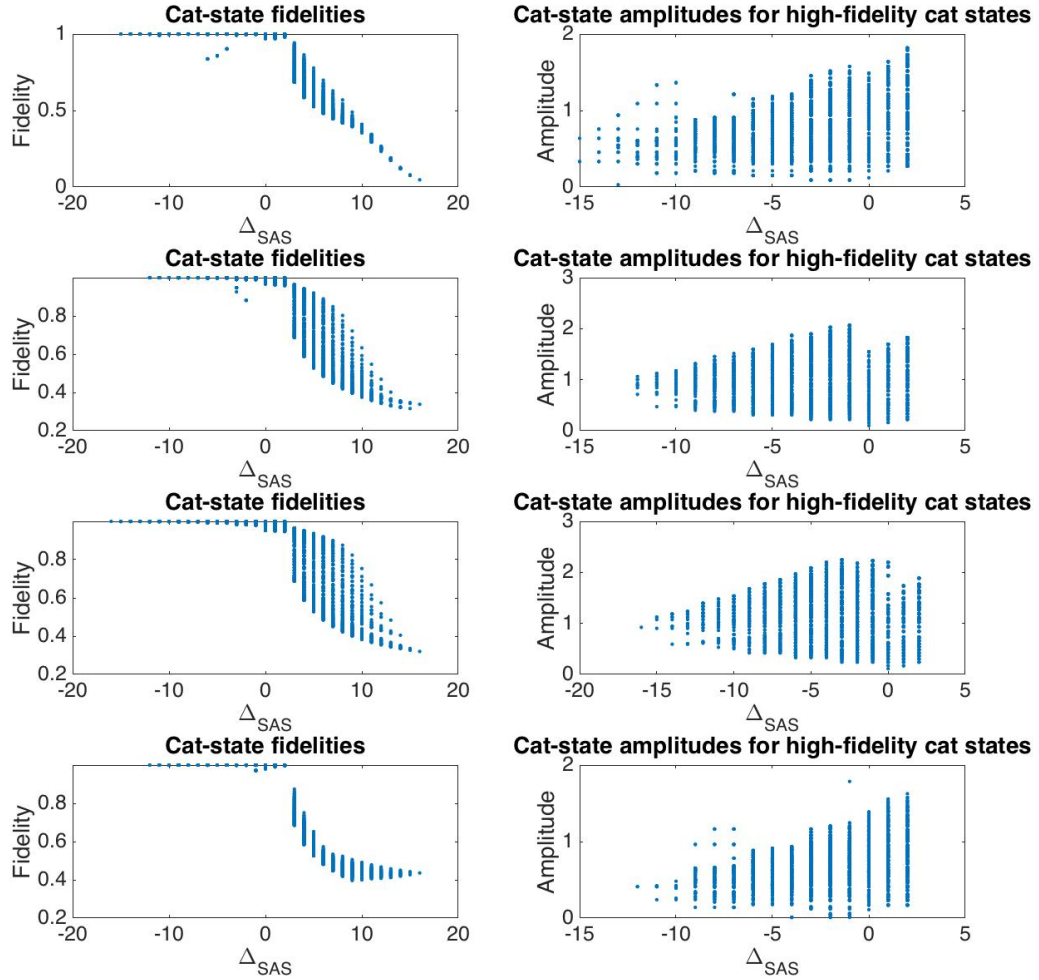


FIGURE 3.22. Cat-state fidelity for conditioned phonon states with different pump amplitudes, and cat-state amplitudes for states with high cat-state fidelity. Top row: $A_0 = A_3 = 60$; Second row: $A_0 = A_3 = 20$; Third row: $A_0 = 20, A_3 = 60$; Bottom row: $A_0 = 60, A_3 = 20$.

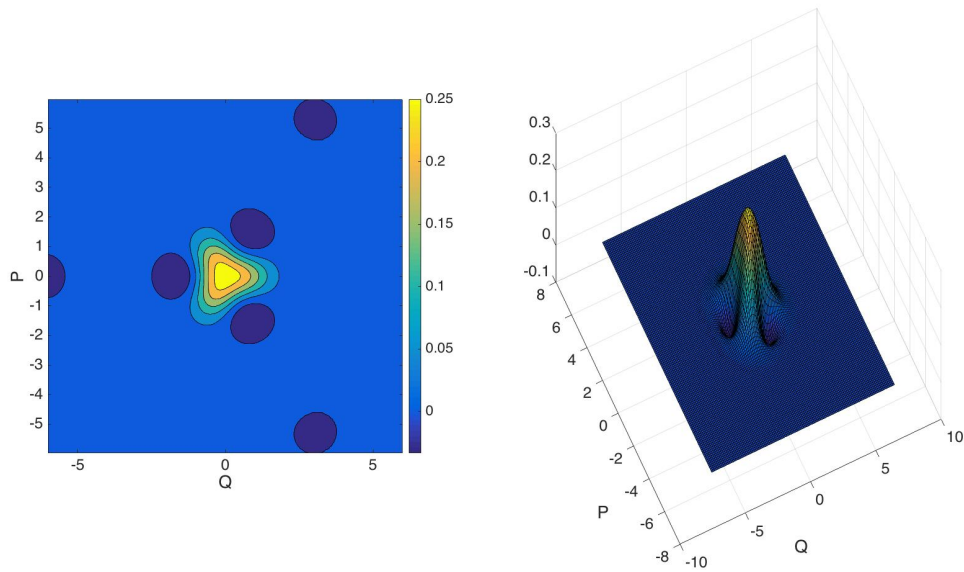


FIGURE 3.23. Wigner distribution for the phonon state conditioned on measuring three photons in each optical mode, with strong equal pumps $A_0 = A_3 = 60$.

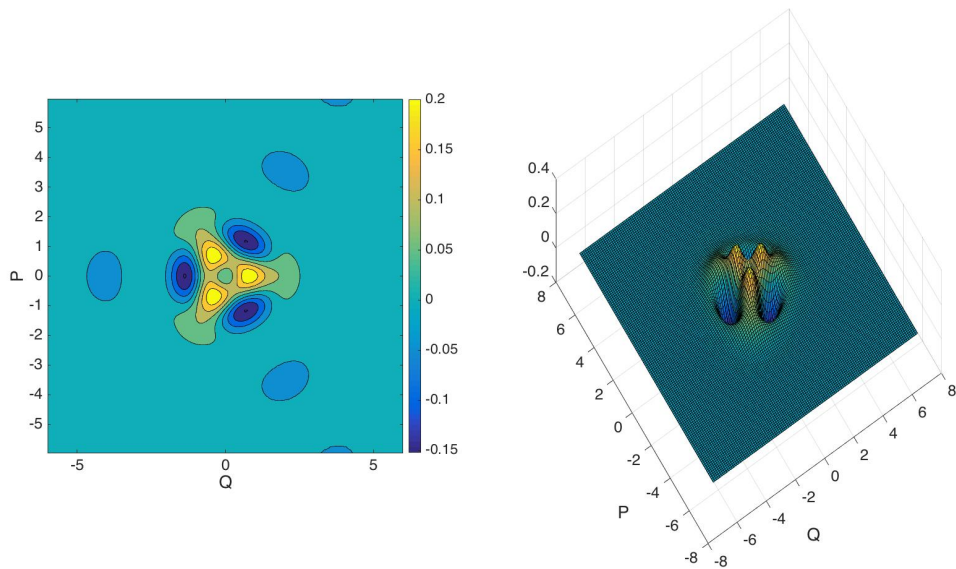


FIGURE 3.24. Wigner distribution for the phonon state conditioned on measuring three photons in each optical mode, with weak equal pumps $A_0 = A_3 = 20$.

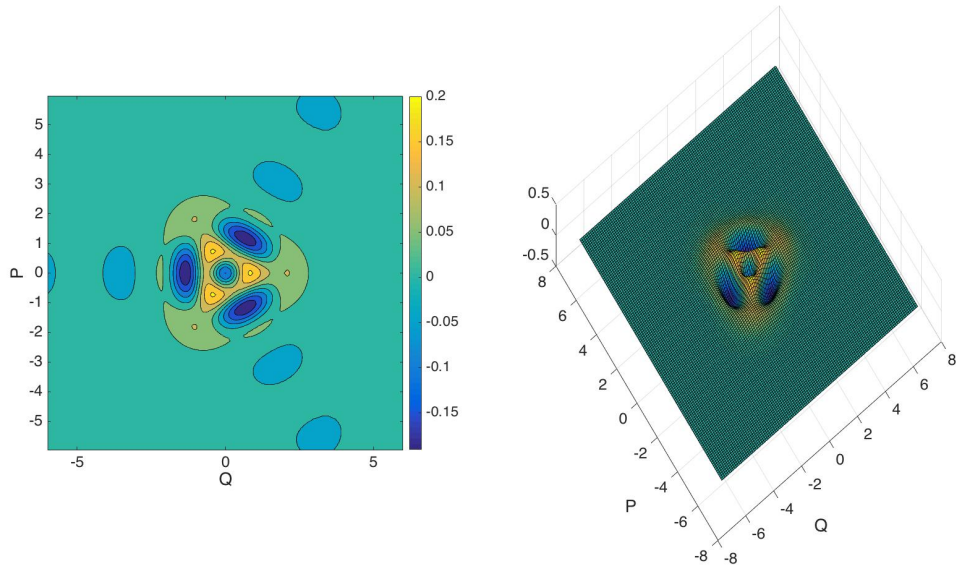


FIGURE 3.25. Wigner distribution for the phonon state conditioned on measuring three photons in each optical mode, with weak red and strong blue pumps $A_0 = 20, A_3 = 60$.

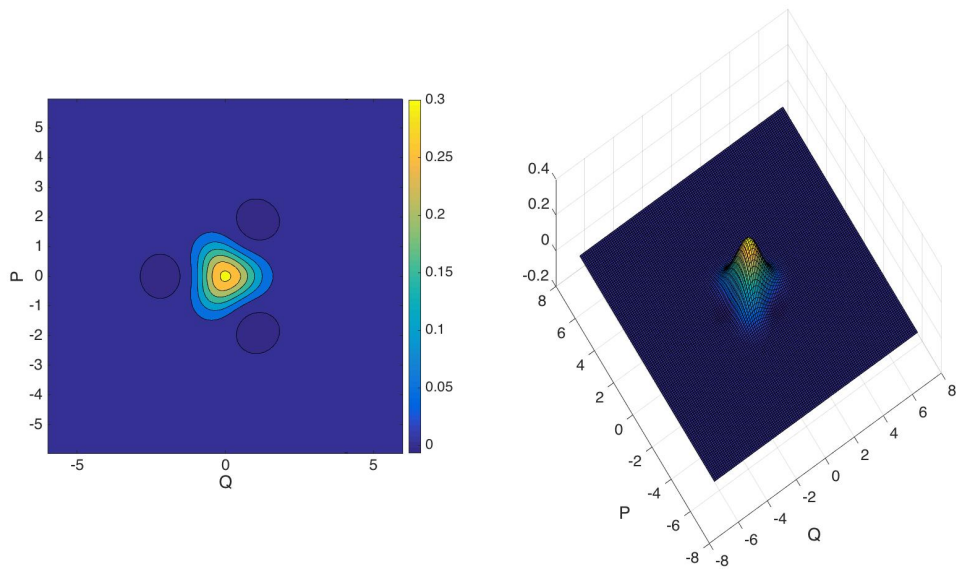


FIGURE 3.26. Wigner distribution for the phonon state conditioned on measuring three photons in each optical mode, with strong red and weak blue pumps $A_0 = 60, A_3 = 20$.

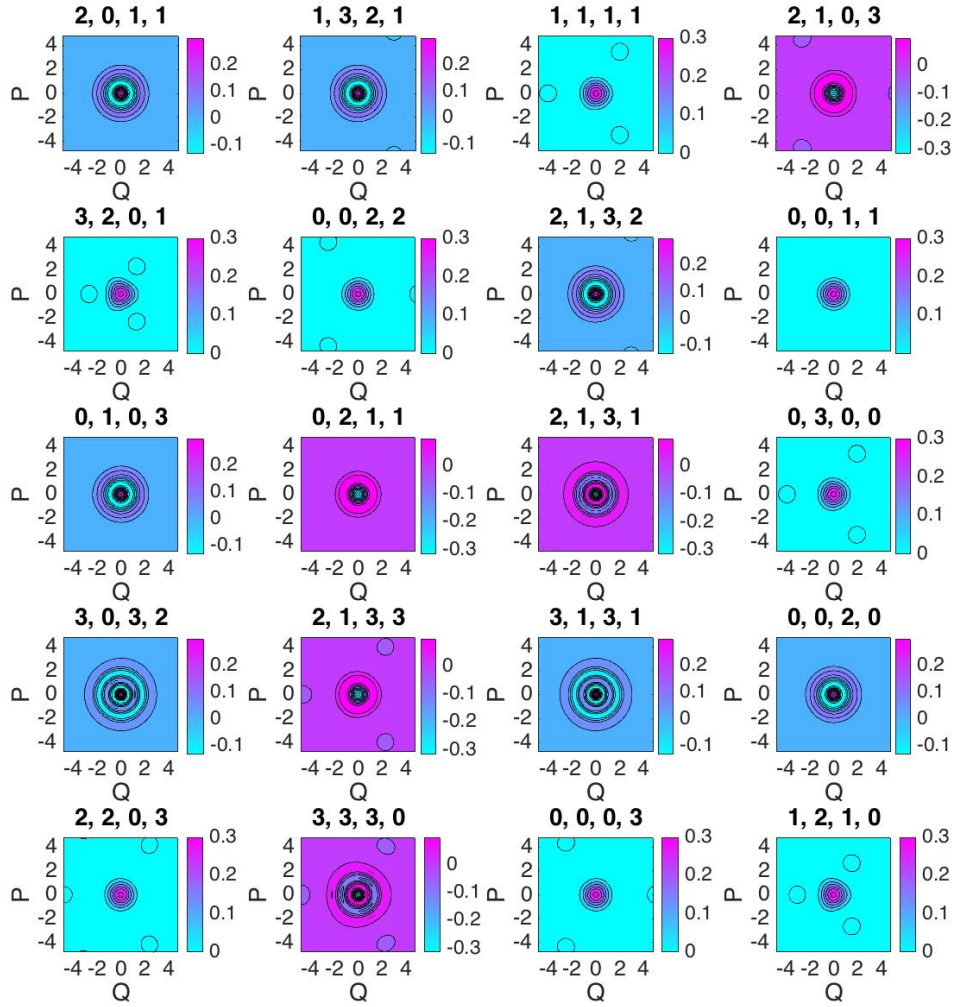


FIGURE 3.27. Wigner distributions for an arbitrary subset of conditioned phonon states (part 1). Each distribution is labeled by four integers which correspond to $n_{-1}^{meas}, n_1^{meas}, n_2^{meas}, n_4^{meas}$.

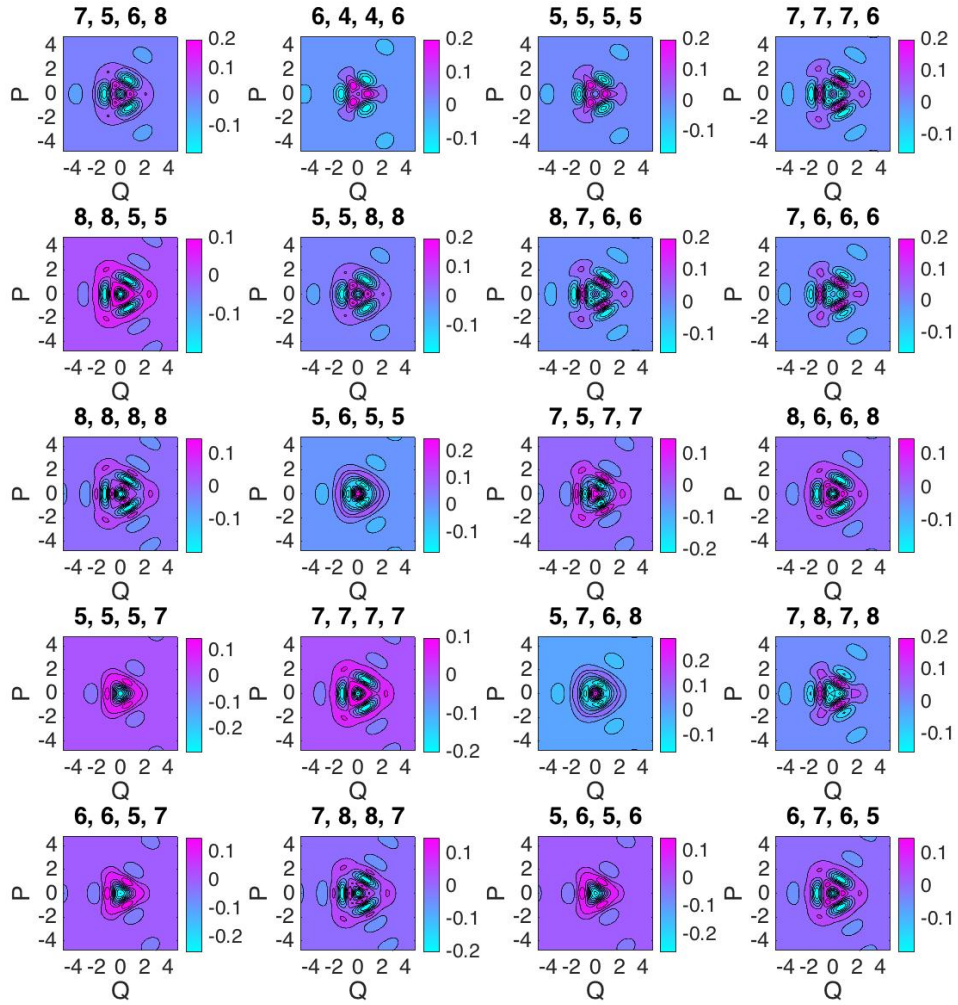


FIGURE 3.28. Wigner distributions for an arbitrary subset of conditioned phonon states (part 2). Each distribution is labeled by four integers which correspond to $n_{-1}^{meas}, n_1^{meas}, n_2^{meas}, n_4^{meas}$.

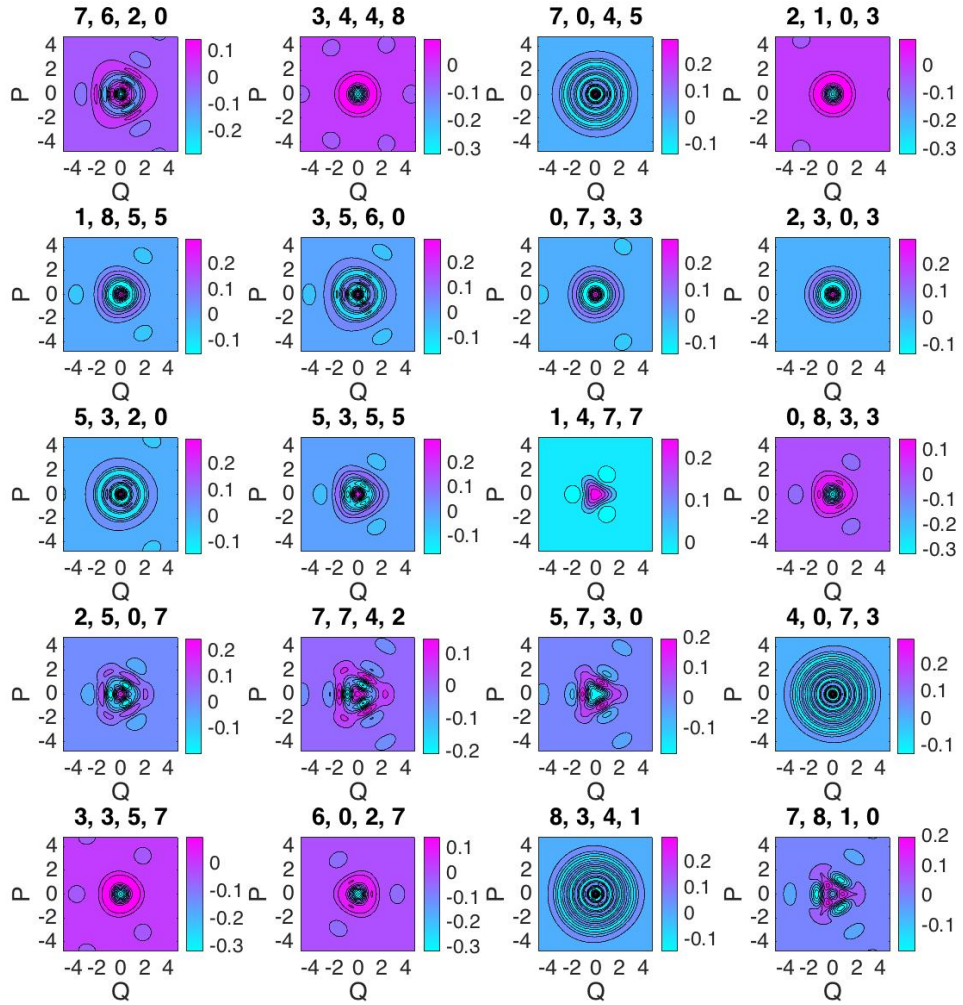


FIGURE 3.29. Wigner distributions for an arbitrary subset of conditioned phonon states (part 3). Each distribution is labeled by four integers which correspond to $n_{-1}^{meas}, n_1^{meas}, n_2^{meas}, n_4^{meas}$.

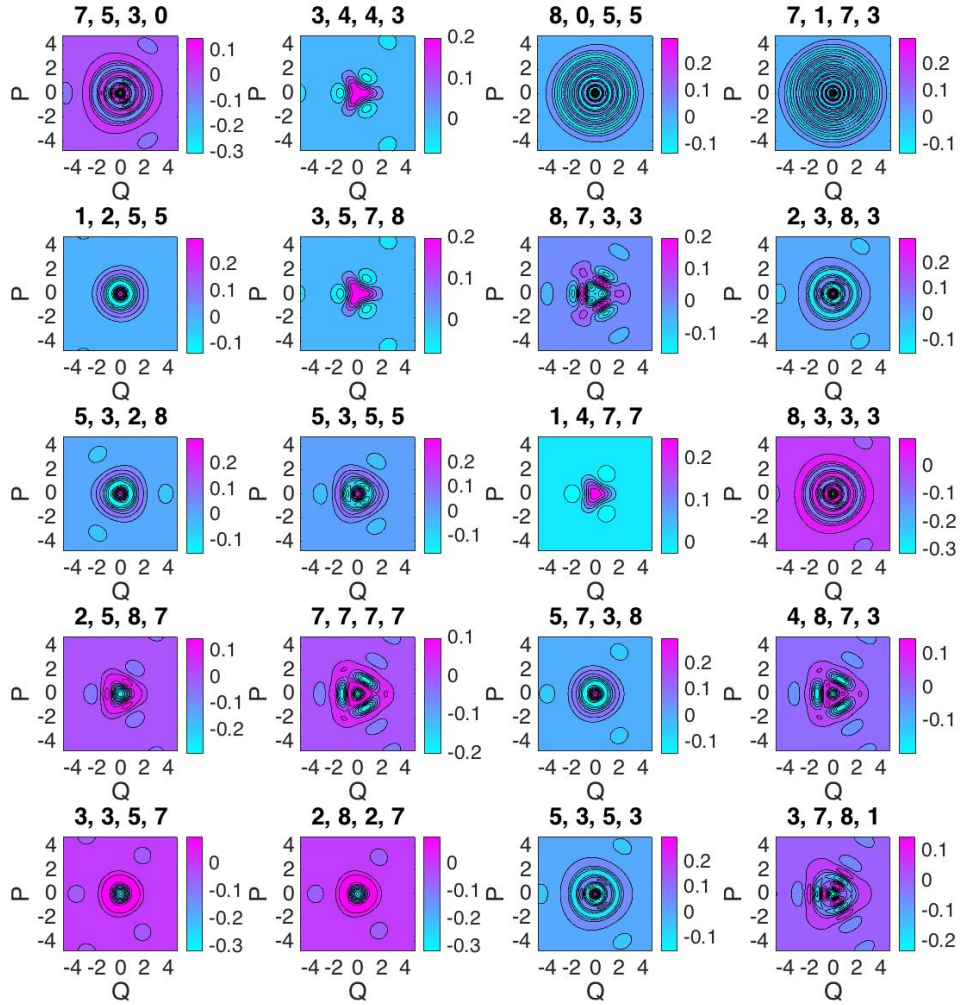


FIGURE 3.30. Wigner distributions for an arbitrary subset of conditioned phonon states (part 4). Each distribution is labeled by four integers which correspond to $n_{-1}^{meas}, n_1^{meas}, n_2^{meas}, n_4^{meas}$.

CHAPTER IV

SEMICLASSICAL THEORY

In this chapter we present a rough semiclassical model of the dual-pumped Raman optical frequency comb. This approach complements the quantum description of the comb, the results of which were featured in Chapter III. One big advantage of the semiclassical model is that it can model somewhat larger numbers of photons and phonons than can the quantum model, because the semiclassical model does not require a basis state for each possible number in each of the five modes. The behavior of the semiclassical model is relevant to the prospects of using the dual-pumped comb in a traditional frequency comb application, such as frequency metrology or ultrashort pulse synthesis.

The semiclassical model of the dual-pumped Raman comb presented here should be considered a toy model. In particular its propensity toward instabilities like those found in generalized squeezed states [17] has not been thoroughly explored. The purpose of the semiclassical model here is to provide confidence in the results of the quantum model and to suggest that interesting phase behavior at macroscopic light levels is in principle possible. It is also worth noting that the results of semiclassical simulations provided us with the initial motivations to study the more theoretically challenging exact quantum solutions presented in Chapter III.

4.1. Semiclassical Maxwell-Bloch equations

In the semiclassical picture, the four optical modes and single phonon mode of the dual-pumped comb are modeled by Maxwell-Bloch equations originally developed by Wu et al [10] for a single-pumped comb with spatial propagation:

$$\begin{aligned} \left(\frac{\partial}{\partial z} + \frac{1}{c} \frac{\partial}{\partial t} \right) E_k^{(-)}(z, t) &= -i\alpha_{2,k+1} E_{k+1}^{(-)}(z, t) \exp(-i\Delta\beta_{k+1}z) P^\dagger(z, t) \\ &\quad - i\alpha_{2,k}^* E_{k-1}^{(-)}(z, t) \exp(i\Delta\beta_k z) P(z, t) \end{aligned} \quad (4.1)$$

and

$$\frac{\partial P^\dagger(z, t)}{\partial t} = i \sum_k \alpha_{1,k} E_k^{(+)}(z, t) E_{k-1}^{(-)}(z, t) \exp(i\Delta\beta_k z). \quad (4.2)$$

In these equations, P is a collective vibration raising operator, $E_k^{(-)}$ is the negative-frequency part of the k th optical mode's electric field, $\alpha_{1,k}$ and $\alpha_{2,k}$ are frequency-dependent coupling coefficients, and $\Delta\beta_k$ are frequency-dependent phase mismatches between optical mode wave vectors. In [10], Equations 4.1 and 4.2 are derived rigorously with $P(z, t)$ defined in terms of the molecular raising operator and $E_k^{(-)}(z, t)$ defined in terms of the photon creation operator. The electric field and collective vibration raising operators obey the commutation relations

$$\begin{aligned} [E_k^{(+)}(z, t), E_j^{(-)}(z', t')] &= \delta_{kj} \frac{2\pi\hbar\omega_k}{A} \delta(z - z' - c(t - t')) \\ [P^\dagger(z, t)P(z', t')] &= \frac{1}{NA} \delta(z - z'). \end{aligned} \quad (4.3)$$

We therefore associate $P(z, t)$ with the phonon creation operator b^\dagger and $E_k^{(-)}(z, t)$ with a photon creation operator a_k^\dagger used in the quantum theory of the previous chapter. For our crude model, we ignore the scaling terms $\alpha_{1,k}$, $\alpha_{2,k}$, c . These terms were set to unity in the quantum model, so setting them to unity here as well enables a better comparison between the two approaches. Furthermore, because we are modeling the

comb in a cavity, we omit the spatial propagation terms in Equations 4.1 and 4.2. (That includes the phase mismatch terms $\Delta\beta z$. A more realistic cavity model would include an analogue to the phase mismatch terms in the form of cavity dispersion that detunes the optical modes from their ideal frequencies. As in the quantum model, however, all such detunings are here set to zero.) Our toy semiclassical model of a cavity-based comb is then

$$\begin{aligned}\frac{\partial E_k^{(-)}(t)}{\partial t} &= -iE_{k+1}^{(-)}(t)P^\dagger(t) - iE_{k-1}^{(-)}(t)P(t) \\ \frac{\partial P^\dagger(t)}{\partial t} &= i\sum_k E_k^{(+)}(t)E_{k-1}^{(-)}(t)\end{aligned}\tag{4.4}$$

and the dual-pumped comb with four optical modes $E_{-1}(t), E_1(t), E_2(t), E_4(t)$ and two constant pumps E_0 and E_3 is described by the model

$$\begin{aligned}\frac{\partial E_{-1}^{(-)}(t)}{\partial t} &= -iE_0^{(-)}P^\dagger(t) \\ \frac{\partial E_1^{(-)}(t)}{\partial t} &= -iE_2^{(-)}(t)P^\dagger(t) - iE_0^{(-)}P(t) \\ \frac{\partial E_2^{(-)}(t)}{\partial t} &= -iE_3^{(-)}P^\dagger(t) - iE_1^{(-)}(t)P(t) \\ \frac{\partial E_4^{(-)}(t)}{\partial t} &= -iE_3^{(-)}P(t) \\ \frac{\partial P^\dagger(t)}{\partial t} &= iE_0^{(+)}E_{-1}^{(-)}(t) + iE_1^{(+)}(t)E_0^{(-)} \\ &\quad + iE_2^{(+)}(t)E_1^{(-)}(t) + iE_3^{(+)}E_2^{(-)}(t) + iE_4^{(+)}(t)E_3^{(-)}.\end{aligned}\tag{4.5}$$

We can confirm that this set of equations corresponds to the quantum Hamiltonian from Chapter III by using the standard Heisenberg equation of motion. For instance,

$$\begin{aligned}
\frac{\partial b}{\partial t} &= i[H, b] & (4.6) \\
&= -i[b^\dagger, b]a_{-1}^\dagger A_0 - i[b^\dagger, b]A_0^\dagger a_1 - i[b^\dagger, b]a_1^\dagger a_2 - i[b^\dagger, \dagger]a_2^\dagger A_3 - i[b^\dagger, b]A_3^\dagger a_4 \\
&= ia_{-1}^\dagger A_0 + iA_0^\dagger a_1 + ia_1^\dagger a_2 + ia_2^\dagger A_3 + iA_3^\dagger a_4 \\
\rightarrow \frac{\partial P^\dagger}{\partial t} &= iE_0^{(+)} E_{-1}^{(-)}(t) + iE_1^{(+)}(t)E_0^{(-)} \\
&\quad + iE_2^{(+)}(t)E_1^{(-)}(t) + iE_3^{(+)} E_2^{(-)}(t) + iE_4^{(+)}(t)E_3^{(-)},
\end{aligned}$$

and a similar procedure for the optical modes shows that the equations of motion for their quantum operators correspond to Equations 4.5.

The set of coupled ordinary differential equations in 4.5 describe the deterministic time evolution of the complex amplitudes E_k and P^\dagger from their initial conditions at $t = 0$. Those initial conditions are the zero-point vacuum fluctuations of the optical and phonon modes. In the quantum model, the Wigner phase-space distribution of the vacuum state of a given mode is a Gaussian centered at the origin in phase space. In a semiclassical picture, the vacuum state of that mode is modeled as a random complex amplitude with real and imaginary components independently drawn from a normal distribution with zero mean and unit variance. Solving the equations once from a single set of random initial conditions models the outcome of a single measurement of the phonon and photon amplitudes. These amplitudes can be represented as a point in the phase space of each mode. In order to construct a full phase-space distribution akin to the Wigner distributions of Chapter III, we solve the equations many times,

with a new set of random initial conditions on each trial, and plot the ensemble of points in phase space¹. It is convenient to think of each point in phase space (or each trial of solving the coupled equations) as corresponding to one pulse from the pump lasers that create the comb. We will use this description throughout the rest of the chapter, referring to each trial as a “shot” from the pump lasers.

4.2. Semiclassical results

The phase space distributions in Figure 4.1 show the amplitudes of the phonon modes and all four optical modes after 15,000 independent shots. Here the pump amplitudes are set to $E_0 = E_3 = 60$ and the time is $t = 0.015$, corresponding to the parameters used throughout most of the quantum theory results. Note that these results show the unconditioned states of the phonon and optical modes. These distributions all appear approximately Gaussian, with no preferential growth along any particular phase. The width of the phonon mode and the E_2 mode (the blue-Stokes mode) distributions are larger than the others.

Next we increase the time to $t = 0.045$, producing the distributions shown in Figure 4.2. At this time, the modes E_1 and E_2 (the red-anti-Stokes and blue-Stokes modes, respectively) have grown preferentially along the phases 0 , $2\pi/3$, and $-2\pi/3$. The phonon mode distribution is still Gaussian and appears to be the smallest distribution of the five.

Finally we increase the time to $t = 0.070$, producing the distributions shown in Figure 4.3. These distributions all grow preferentially along three phases, though the phonon mode and the E_4 mode (the blue-anti-Stokes mode) are rotated relative to the others. The three-phase preference of the blue-anti-Stokes and red-Stokes modes

¹The phase-space distributions in Chapter I were obtained by this method.

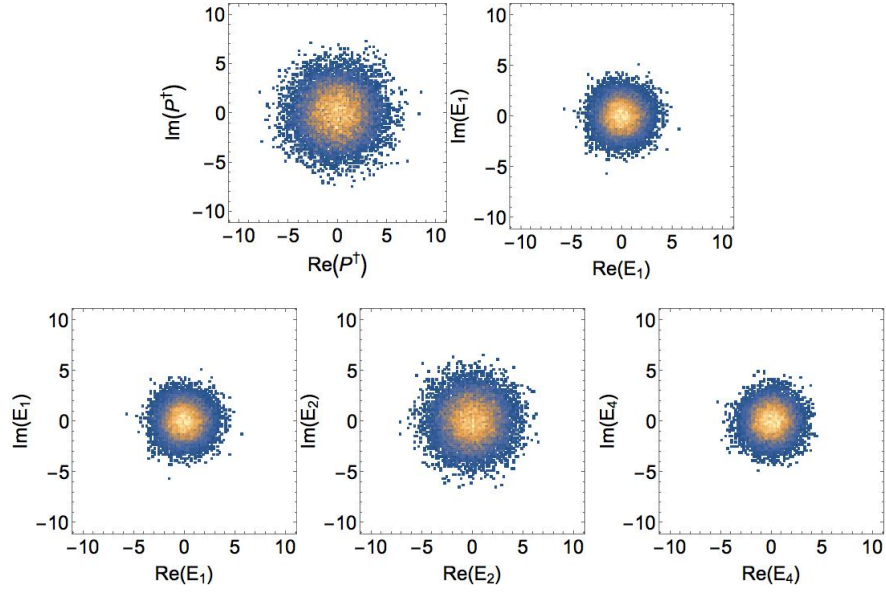


FIGURE 4.1. Semiclassical phase-space distributions for phonon mode and optical modes at $t = 0.015$.

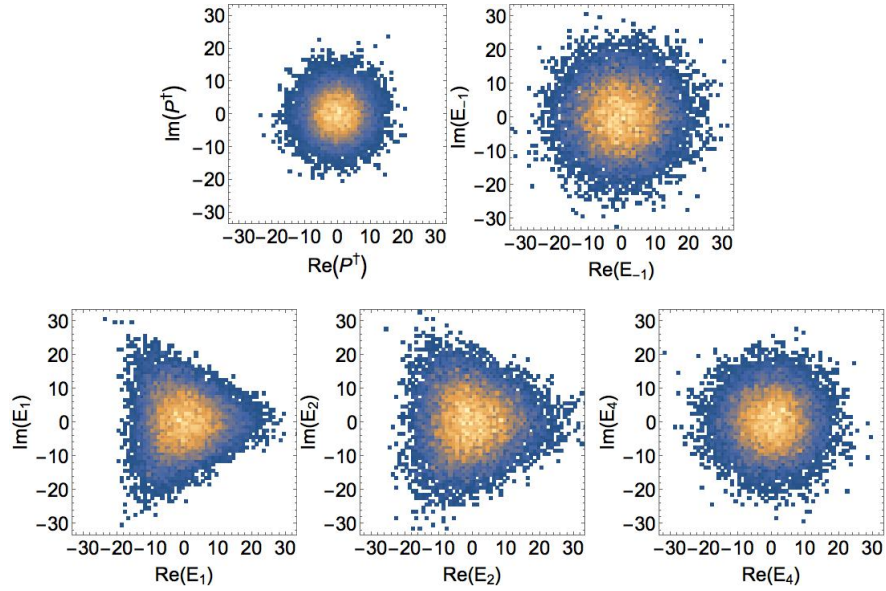


FIGURE 4.2. Semiclassical phase-space distributions for phonon mode and optical modes at $t = 0.045$.

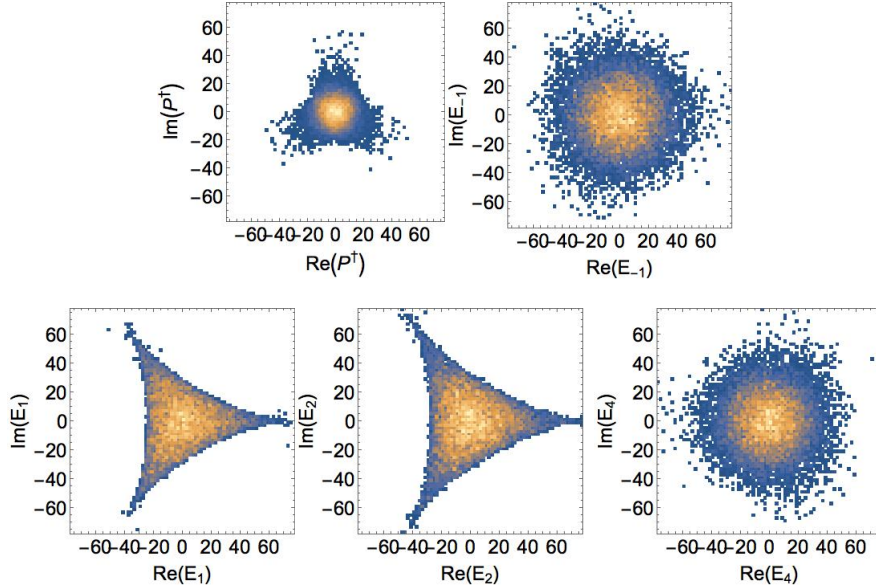


FIGURE 4.3. Semiclassical phase-space distributions for phonon mode and optical modes at $t = 0.070$.

is weaker than the others. The distributions of the E_1 and E_2 mode (the red-anti-Stokes and blue-Stokes modes) are extremely sharp. As noted by Braunstein and McLachlan in their work on generalized squeezing [17], these sharp distributions are characteristic to many classical systems but absent in their quantum counterparts due to mechanisms such as quantum diffusion.

4.3. Interpretation in context of spontaneous phase correlations

It is remarkable that the phonon and optical modes in the semiclassical case show strong preferential growth along three phases even when not conditioned on any photon number measurement. In the quantum model, which was limited to shorter times than the semiclassical model, the unconditioned phonon mode showed only a very weak three-phase preference. It is possible that if the quantum model were extended to longer times, the unconditioned phonon mode would show a stronger

three-phase preference. Some of the conditioned phonon states, on the other hand, did show a strong three-phase preference even at short times. In Chapter III, we showed that the strong three-phase preference of those conditioned phonon states can be explained in terms of their number-state representations. In the semiclassical approach, the state cannot be represented in the number basis and so another explanation for the strong three-phase symmetry must be sought. We instead interpret the semiclassical three-phase preference in light of the spontaneous phase correlations identified in other work [10], [12] and briefly mentioned in Chapter I. As shown in [10], if the optical fields and phonon operator are written as

$$E_k^{(-)} = |E_k^{(-)}| \exp(-i\theta_k) \quad (4.7)$$

$$P = |P| \exp(-i\phi),$$

then the time evolution of the phonon mode according to Equation 4.4 is

$$i|P| \frac{\partial \phi}{\partial t} + \frac{\partial |P|}{\partial t} = \sum_k |E_k^{(+)}| |E_{k-1}^{(-)}| \exp(i\theta_k - i\theta_{k-1} - i\phi). \quad (4.8)$$

Splitting the righthand side of Equation 4.8 into its real and imaginary components produces two real time-evolution equations for the amplitude and the phase of the phonon:

$$\frac{\partial |P|}{\partial t} = \sum_k |E_k^{(+)}| |E_{k-1}^{(-)}| \cos(\theta_k - \theta_{k-1} - \phi) \quad (4.9)$$

$$\frac{\partial \phi}{\partial t} = \sum_k |E_k^{(+)}| |E_{k-1}^{(-)}| \sin(\theta_k - \theta_{k-1} - \phi).$$

As pointed out in [10], the first equation shows that the amplitude of the phonon mode is greatest when $\phi = \theta_k - \theta_{k-1}$. If the pump, which has fixed phase, is at the $k = 0$ mode, then this relation is equivalent to the phase relation

$$\theta_k \approx \theta_0 + k\phi_{phonon} \quad (4.10)$$

introduced in Chapter I. The second equation in 4.9 shows that the phonon phase becomes constant in time as it approaches the maximal-growth value $\phi = \theta_k - \theta_{k-1}$, which is consistent with the known theory of stimulated Raman scattering in the transient high-gain regime [8], [13].

As described in Chapter I, in a single-pumped Raman comb, any value of ϕ is equally likely to become the maximal-growth phase on a given shot, but in a dual-pumped Raman comb where the two pumps are separated in frequency by $j\omega_{phonon}$, there are only j possible maximal-growth phase values:

$$\phi_{phonon} \approx \frac{1}{j}(\theta_j - \theta_0) + \frac{2\pi M}{j} \quad (4.11)$$

where M represents any integer. The idea of using a second pump to restrict the number of possible maximal-growth phases was first introduced in [10], but in that work it was incorrectly predicted that the second pump would produce only one maximal-growth phase. Essentially, the factor of 2π in Equation 4.11 was overlooked. Even imposing j values of the maximal-growth phase, however, constitutes some phase-stability in the comb. Remarkably, this phase stability arises spontaneously, with no injected coherence (unless $j = 1$, which corresponds to classically driving the medium, as in [14], [15], [16]). In light of the quantum model explored in Chapter

III, this macroscopic phase stability, which can be predicted by a semiclassical model, appears to be a consequence of the quantum state of the phonon mode.

CHAPTER V

CONCLUSION

In this dissertation we have explored the quantum phonon states that are produced by Raman scattering in a dual-pumped Raman optical frequency comb in a cavity. This study was motivated by earlier work which showed that the optical modes produced in a single-pumped Raman frequency comb spontaneously become phase-correlated through their coupling with each other and with the phonon mode [10], [12]. The phase correlation in the single-pumped comb occurs because the optical modes grow preferentially with a phase that is determined by the random phase of the phonon mode. The phase of the phonon mode, however, arises independently upon each pulse of the pump laser and is uniform-randomly distributed. Based on the single-pumped comb theory, we predicted in the present study that the addition of a second pump, phase-locked to the first pump and shifted from it by three times the phonon frequency, would create three phases along which the phonon mode would preferentially grow. The three-phase symmetry of the phonon mode is suggestive of a quantum three-boson-squeezing process, leading us to an in-depth study of the quantum state of the phonon mode in the dual-pumped Raman comb.

Our numerical investigation, based on near-exact solutions of the high-dimensional Schrödinger equation, showed that the dual-pumped comb does create a three-phase symmetry in the phonon mode. At short times, the extent of the preferential growth of the mode along those three phases is very slight because relatively little of the higher-order scattering that couples the action of the two pumps has occurred. By conditioning on the number of photons measured in each optical mode, however, we can produce conditioned phonon states with far more

pronounced three-phase preferences. Conditioning on the photon numbers in each optical mode effectively identifies the set of Raman processes that could have produced that combination of photon numbers. For any combination, the set of associated Raman processes includes first-order scattering from the two pumps and higher-order scattering that adds phonon numbers in multiples of three. The conditioned phonon state is therefore a superposition of phonon number states occurring in multiples of three. That result can be predicted from the rotational symmetry of the dual-pumped comb Hamiltonian, and it directly implies the three-phase symmetry of the phonon states. The set of higher-order Raman processes includes second-order scattering, in which a photon scatters from a pump mode into an optical mode and then into the next optical mode, as well as third-order scattering, in which a photon scatters from a pump mode through the next two optical modes and into the other pump mode. Because the pumps are not quantized, the effect of third-order scattering is to simultaneously create or annihilate three phonons with no net change to the photon numbers in the optical modes. This process is effectively triple phonon generation, which leads to a three-phonon squeezing process on the phonon state created by first-order scattering. The effect of second-order scattering, however, is to increase the probability amplitude in higher-order phonon states. As a result, large amounts of second-order scattering tend to make the conditioned phonon state more like a Schrödinger-cat state. Comparing the phase probability distributions of the cat-like states and the three-phonon-squeezed states shows that the three-phase preference is most distinct for the cat-like states, because the phonon mode in a cat state grows very little at phases other than the three preferred ones.

After concluding our quantum description of the dual-pumped comb, we briefly explored a semiclassical toy model. The semiclassical model suffers from some

instabilities to which the three-boson-squeezing process is known to be prone, and no attempt is made here to rigorously analyze or remove them. For our purposes, the semiclassical model simply suggests that the three-phase preference of the unconditioned phonon mode becomes more distinct at greater times and photon numbers than can currently be modeled in the quantum simulation. Additionally, the semiclassical model predicts that the optical modes will grow preferentially along three phases as well, which constitutes a spontaneous partial phase-locking that could be useful for a frequency comb.

Future work on the dual-pumped Raman frequency comb should explore the role of deleterious effects such as cavity dispersion, dephasing, and loss, which are ignored in our model. The complete absence of phase mismatch is known to suppress stimulated Stokes and anti-Stokes scattering driven by a single pump [10], [46], [47], [48]. The inclusion of phase mismatch in our model via cavity dispersion is likely to impact the strength of the three-phase preference observed in the optical and phonon modes. Cavity dispersion could also detune the optical mode frequencies from the ideal comb frequencies that are separated by exactly the phonon frequency. The vital second- and third-order processes would suffer as a result. In choosing a physical system in which to implement the dual-pumped comb, minimizing these detunings is key. Another requirement is the two phase-locked pump lasers whose frequency can be separated by exactly three times the phonon frequency. The phase difference between the two pumps must be constant from shot to shot in order for the three phases of preferred growth to retain the same values, which is highly desirable in an experiment. In the context of creating a partially phase-stabilized comb [10], it was pointed out that a Ti:sapphire laser (tuned to a particular wavelength near 802 nm) and its second harmonic (produced by a

nonlinear-optical crystal) would be phase-locked and separated in frequency by three times the vibrational Raman shift of molecular hydrogen gas. An additional hurdle is identifying a mechanism by which the phonon quantum states can be measured and accessed if they are to be used in a quantum information network.

APPENDIX A

WIGNER FUNCTION DERIVATION

The conditioned phonon states discussed in Chapter III are superpositions of number states. Here we derive the Wigner distribution for such a state.

The Wigner distribution for any pure state is

$$W(Q, P) = \frac{1}{2\pi} \int_{-\infty}^{\infty} dQ' \exp(-iPQ') \psi(Q + Q'/2) \psi^*(Q - Q'/2) \quad (\text{A.1})$$

so for a superposition of number states:

$$|\psi\rangle = \sum_N C_N |N\rangle, \quad (\text{A.2})$$

the Wigner distribution can be calculated as

$$\begin{aligned} W(Q, P) &= \frac{1}{2\pi} e^{-Q^2} \int_{-\infty}^{\infty} dQ' \exp(-iPQ') e^{-(Q'/2)^2} \\ &\times \sum_N \left(C_N \frac{1}{\sqrt{2^N N! \sqrt{\pi}}} H_N(Q + Q'/2) \right) \\ &\times \sum_{N'} \left(C_{N'}^* \frac{1}{\sqrt{2^{N'} N'! \sqrt{\pi}}} H_{N'}(Q - Q'/2) \right) \end{aligned} \quad (\text{A.3})$$

where H_N is the Hermite polynomial.

The integral can be evaluated numerically by a Fourier transform, but here we derive an analytical solution. We first obtain a solution for the general case where C_N are complex, and then find an even simpler solution for the case where C_N are all real.

A.1. Complex amplitudes C_N

We evaluate the integral by transforming it to match a sum of two integrals with known analytical solutions [49]:

$$\begin{aligned} \int_{-\infty}^{\infty} dx \sin bx H_n(x) H_{n+2m+1}(x) e^{-x^2} & \quad (\text{A.4}) \\ & = 2^{n+\frac{1}{2}} (-1)^m \sqrt{\frac{\pi}{2}} n! b^{2m+1} e^{-\frac{b^2}{4}} L_n^{2m+1}\left(\frac{b^2}{2}\right), b > 0 \end{aligned}$$

$$\begin{aligned} \int_{-\infty}^{\infty} dx \cos bx H_n(x) H_{n+2m}(x) e^{-x^2} & \quad (\text{A.5}) \\ & = 2^{n+\frac{1}{2}} (-1)^m \sqrt{\frac{\pi}{2}} n! b^{2m} e^{-\frac{b^2}{4}} L_n^{2m}\left(\frac{b^2}{2}\right), b > 0 \end{aligned}$$

(There is an error in [49]: the result they give for the integral in Equation A.4 should be divided by $\sqrt{2}$.)

Note the parity of the functions on the left-hand sides of these equations. In the sine integral (Equation A.4), the orders of the two Hermite polynomials (n and $n + 2m + 1$) have been expressed such that the Hermite polynomials always have opposite parity. If they had the same parity, the integrand would be odd and the integral would be zero. The opposite is true for the cosine integral: if the Hermite polynomial orders are the same parity, the integral is equal to the right-hand side of Equation A.5, but if they are the same parity, the integral is equal to zero.

The Hermite polynomials in Equation A.3 can be translated to match those in Equations A.4- A.5 by using the following identity [50]:

$$H_n(x+y) = \sum_{k=0}^n \binom{n}{k} H_k(x) (2y)^{(n-k)}. \quad (\text{A.6})$$

That is,

$$\begin{aligned} H_N(Q + Q'/2) &= \sum_{k=0}^N \binom{N}{k} H_k\left(\frac{Q'}{2}\right) (2Q)^{(N-k)} \\ H_{N'}(Q - Q'/2) &= \sum_{j=0}^{N'} \binom{N'}{j} H_j\left(\frac{-Q'}{2}\right) (2Q)^{(N'-j)} \\ &= \sum_{j=0}^{N'} \binom{N'}{j} (-1)^j H_j\left(\frac{Q'}{2}\right) (2Q)^{(N'-j)}. \end{aligned} \quad (\text{A.7})$$

Insert this into the Wigner distribution:

$$\begin{aligned} W(Q, P) &= \frac{1}{2\pi} e^{-Q^2} \int_{-\infty}^{\infty} dQ' \exp(-iPQ') e^{-(Q'/2)^2} \\ &\times \sum_N \left(C_N \frac{1}{\sqrt{2^N N! \sqrt{\pi}}} \left(\sum_{k=0}^N \binom{N}{k} H_k\left(\frac{Q'}{2}\right) (2Q)^{(N-k)} \right) \right) \\ &\times \sum_{N'} \left(C_{N'}^* \frac{1}{\sqrt{2^{N'} N'! \sqrt{\pi}}} \left(\sum_{j=0}^{N'} \binom{N'}{j} (-1)^j H_j\left(\frac{Q'}{2}\right) (2Q)^{(N'-j)} \right) \right), \end{aligned} \quad (\text{A.8})$$

simplify by defining

$$\begin{aligned} f_{N,k}(Q) &= C_N \frac{1}{\sqrt{2^N N! \sqrt{\pi}}} \binom{N}{k} (2Q)^{(N-k)} \\ g_{N',j}(Q) &= C_{N'}^* \frac{1}{\sqrt{2^{N'} N'! \sqrt{\pi}}} \binom{N'}{j} (-1)^j (2Q)^{(N'-j)}, \end{aligned} \quad (\text{A.9})$$

and then

$$\begin{aligned}
W(Q, P) &= \frac{1}{2\pi} e^{-Q^2} \int_{-\infty}^{\infty} dQ' \exp(-iPQ') e^{-(Q'/2)^2} \tag{A.10} \\
&\times \sum_N \sum_{k=0}^N \left(f_{N,k}(Q) H_k \left(\frac{Q'}{2} \right) \right) \times \sum_{N'} \sum_{j=0}^{N'} \left(g_{N',j}(Q) H_j \left(\frac{Q'}{2} \right) \right) \\
&= \frac{1}{2\pi} e^{-Q^2} \int_{-\infty}^{\infty} dQ' \exp(-iPQ') e^{-(Q'/2)^2} \\
&\times \sum_N \sum_{k=0}^N \sum_{N'} \sum_{j=0}^{N'} \left(f_{N,k}(Q) H_k \left(\frac{Q'}{2} \right) g_{N',j}(Q) H_j \left(\frac{Q'}{2} \right) \right) \\
&= \frac{1}{2\pi} e^{-Q^2} \sum_N \sum_{k=0}^N \sum_{N'} \sum_{j=0}^{N'} f_{N,k}(Q) g_{N',j}(Q) \\
&\times \left(\int_{-\infty}^{\infty} dQ' \cos(PQ') e^{-(Q'/2)^2} H_k \left(\frac{Q'}{2} \right) H_j \left(\frac{Q'}{2} \right) \right. \\
&\quad \left. - i \int_{-\infty}^{\infty} dQ' \sin(PQ') e^{-(Q'/2)^2} H_k \left(\frac{Q'}{2} \right) H_j \left(\frac{Q'}{2} \right) \right).
\end{aligned}$$

At this point we can use the closed-form integrals in Equations A.4 and A.5 to obtain an analytical solution for the Wigner distribution. However, for a state where the amplitudes C_N are all real, as in the conditional phonon states studied in Chapter III, we can simplify the expression further. In the remainder of this appendix, we take C_N to be real.

A.2. Real amplitudes $C_N = C_N^*$

Consider the sine integral in Equation A.4. It is zero unless j and k have opposite parity. But for any pair of j and k with opposite parity, then at each point in Q , the product $f(Q)_{N,k} g(Q)_{N',j} = -f(Q)_{N',j} g(Q)_{N,k}$, as shown here:

$$\begin{aligned}
f(Q)_{N,k}g(Q)_{N',j} &= C_N \frac{1}{\sqrt{2^N N! \sqrt{\pi}}} \binom{N}{k} (2Q)^{(N-k)} \\
&\times C_{N'} \frac{1}{\sqrt{2^{N'} N'! \sqrt{\pi}}} \binom{N'}{j} (-1)^j (2Q)^{(N'-j)} \\
f(Q)_{N',j}g(Q)_{N,k} &= C_{N'} \frac{1}{\sqrt{2^{N'} N'! \sqrt{\pi}}} \binom{N'}{j} (2Q)^{(N'-j)} \\
&\times C_N \frac{1}{\sqrt{2^N N! \sqrt{\pi}}} \binom{N}{k} (-1)^k (2Q)^{(N-k)} \\
&= f(Q)_{N,k}g(Q)_{N',j} (-1)^{j-k}.
\end{aligned} \tag{A.11}$$

(This is not the case if C_N is not real.)

Furthermore, the value of the integrals do not change when j and k are exchanged. Therefore when j and k have opposite parity, each term in the sum over j, k, N, N' is canceled by another term in that sum, and the net effect is that terms where j and k have opposite parity do not contribute to the sums at all. Because the sine integral is also zero when j and k have the same parity, it can never contribute to $W(Q, P)$. We can omit it entirely and only include the cosine integral, and we only need to evaluate it for j and k pairs with the same parity.

$$\begin{aligned}
W(Q, P) &= \frac{1}{2\pi} e^{-Q^2} \sum_N \sum_{k=0}^N \sum_{N'} \sum_{j=0}^{N'} f_{N,k}(Q) g_{N',j}(Q) \\
&\times \left[\int_{-\infty}^{\infty} dQ' \cos(PQ') e^{-(Q'/2)^2} H_k \left(\frac{Q'}{2} \right) H_j \left(\frac{Q'}{2} \right) \right]; \text{ (j,k same parity)}.
\end{aligned} \tag{A.12}$$

Finally we can use Equation A.5 to evaluate the integral and obtain a relatively simple expression for the Wigner distribution for a superposition of number states with real amplitudes C_N :

$$\begin{aligned}
W(Q, P) &= \sum_N^{all} \sum_{k=0; \text{same parity as } j}^N \sum_{N'}^{all} \sum_{j=0}^{N'} \frac{1}{2\pi} \exp(-Q^2) \\
&\times C_N \frac{1}{\sqrt{2^N N! \sqrt{\pi}}} \binom{N}{k} (2Q)^{(N-k)} \\
&\times C_{N'} \frac{1}{\sqrt{2^{N'} N'! \sqrt{\pi}}} \binom{N'}{j} (-1)^j (2Q)^{(N'-j)} \\
&\times i^{(j-k)} \sqrt{\pi} 2^{(k+1)} k! (2P)^{(j-k)} \exp(-P^2) L_k^{(j-k)}(2P^2).
\end{aligned} \tag{A.13}$$

Note that because j and k are the same parity, $j - k$ is always even. Therefore the term $i^{(j-k)}$ is always real and the whole Wigner distribution is real, as it must be.

APPENDIX B

PROOFS OF CONDITIONED STATE SYMMETRY

B.1. Rotational invariance of Hamiltonian and state

Suppose we have a Hamiltonian H that is invariant under a unitary rotational operator $R(\phi)$. (It is possible that the invariance holds only for certain values of ϕ .) When H acts on the vacuum state, it produces a time-dependent state $|\psi(t)\rangle$:

$$|\psi(t)\rangle = \exp(-iHt)|\text{vacuum}\rangle \quad (\text{B.1})$$

Then the rotated state is

$$\begin{aligned} R(\phi)|\psi(t)\rangle &= R(\phi) \exp(-iHt)|\text{vacuum}\rangle \\ &= R(\phi) \exp(-iHt)R^\dagger(\phi)R(\phi)|\text{vacuum}\rangle \\ &= R(\phi) \exp(-iHt)R^\dagger(\phi)|\text{vacuum}\rangle \end{aligned} \quad (\text{B.2})$$

where we have used the fact that the vacuum state is invariant under rotation. (In fact we could have started with any rotationally-invariant state.) Now we expand the time evolution operator:

$$\begin{aligned} R(\phi)|\psi(t)\rangle &= R(\phi)[1 - iHt + \frac{1}{2}(iHt)^2 + \dots]R^\dagger(\phi)|\text{vacuum}\rangle \\ &= [R(\phi)R^\dagger(\phi) - iR(\phi)HR^\dagger(\phi)t - \frac{1}{2}R(\phi)HR(\phi)R^\dagger(\phi)HR^\dagger(\phi)t^2 + \dots]|\text{vacuum}\rangle. \end{aligned} \quad (\text{B.3})$$

Because $R(\phi)$ is unitary, and because the Hamiltonian is invariant under this rotation (that is, $R^\dagger(\phi)HR(\phi) = H$),

$$R(\phi)|\psi(t)\rangle = [1 - iR(\phi)HR^\dagger(\phi)t - \frac{1}{2}R(\phi)HR^\dagger(\phi)R(\phi)HR^\dagger(\phi)t^2 + \dots]|\text{vacuum}\rangle. \quad (\text{B.4})$$

Now consider that $R(\phi)HR^\dagger(\phi) = (R^\dagger(\phi)H^\dagger R(\phi))^\dagger = (R^\dagger(\phi)HR(\phi))^\dagger$, and because we have already shown that the Hamiltonian is invariant under this rotation, $(R^\dagger(\phi)HR(\phi))^\dagger = H^\dagger = H$. Then

$$\begin{aligned} R(\phi)|\psi(t)\rangle &= [1 - iHt - \frac{1}{2}HHt^2 + \dots]|\text{vacuum}\rangle & (\text{B.5}) \\ &= \exp(-iHt)|\text{vacuum}\rangle \\ &= |\psi(t)\rangle. \end{aligned}$$

That is, given a Hamiltonian that is invariant under the phase rotation $R(\phi)$, the state $|\psi(t)\rangle$ is also invariant under that rotation (provided the initial state was also invariant under the rotation).

B.2. Invariance of conditioned phonon states

As shown in Chapter III, the Hamiltonian describing the dual-pumped Raman optical frequency comb is invariant under a specific rotation $R(\phi)$, provided $\phi = \pm 2\pi/3$.¹ This rotation operator is a generalization of the usual single-mode rotation [51],

¹This fact was suggested to us by Steven van Enk.

$$R(\phi)_{single-mode} = \exp(-i\phi\hat{n}), \quad (\text{B.6})$$

where

$$\begin{aligned} R(\phi)_{single-mode}|n\rangle &= \exp(-i\phi\hat{n})|n\rangle \\ &= \exp(-i\phi n)|n\rangle, \end{aligned} \quad (\text{B.7})$$

because the number states $|n\rangle$ are eigenstates of the number operator \hat{n} with eigenvalues n .

The rotational operator we consider for the Raman comb Hamiltonian has a different rotation for each of the five modes:

$$\begin{aligned} R(\phi) &= \exp(-i\phi\hat{N}) \exp\left(-i \sum_k k\phi\hat{n}_k\right) \\ R(\phi)|Nn_{-1}n_1n_2n_4\rangle &= \exp(-i\phi N) \exp\left(-i \sum_k k\phi n_k\right)|Nn_{-1}n_1n_2n_4\rangle, \end{aligned} \quad (\text{B.8})$$

where the Hamiltonian is rotationally invariant when $\phi = \pm 2\pi/3$.

We have shown in Equation B.5 that the invariance of a Hamiltonian under a rotation $R(\phi)$ implies that the state produced by the time evolution of that Hamiltonian on the vacuum state will also be rotationally invariant. The dual-pumped comb Hamiltonian from Chapter III is shown in that chapter to be invariant under the rotation defined by Equation B.8 when $\phi = \pm 2\pi/3$. Therefore the states $|\psi(N, n_{-1}, n_1, n_2, n_4)\rangle$ generated from the vacuum by that Hamiltonian are also rotationally invariant. We show here that the invariance of that five-mode state

implies that the conditioned phonon state created by projecting $|\psi(N, n_{-1}, n_1, n_2, n_4)\rangle$ onto number states $|n_{-1}^{meas} n_1^{meas} n_2^{meas} n_4^{meas}\rangle$ is also invariant:

$$\begin{aligned}
|\psi_{cond}(N)\rangle &= \sum_N C_{N n_{-1}^{meas} n_1^{meas} n_2^{meas} n_4^{meas}} |N\rangle \tag{B.9} \\
&= \langle n_{-1}^{meas} n_1^{meas} n_2^{meas} n_4^{meas} | \psi(N, n_{-1}, n_1, n_2, n_4)\rangle \\
&= \langle n_{-1}^{meas} n_1^{meas} n_2^{meas} n_4^{meas} | R(\phi) | \psi(N, n_{-1}, n_1, n_2, n_4)\rangle \\
&= \langle n_{-1}^{meas} n_1^{meas} n_2^{meas} n_4^{meas} | \exp(-i\phi\hat{N}) \exp(-i\sum_k k\phi\hat{n}_k) | \psi(N, n_{-1}, n_1, n_2, n_4)\rangle \\
&= \exp(i\sum_k k\phi n_k^{meas}) \langle n_{-1}^{meas} n_1^{meas} n_2^{meas} n_4^{meas} | \exp(-i\phi\hat{N}) | \psi(N, n_{-1}, n_1, n_2, n_4)\rangle \\
&= \exp(i\sum_k k\phi n_k^{meas}) \exp(-i\phi\hat{N}) \sum_N C_{N n_{-1}^{meas} n_1^{meas} n_2^{meas} n_4^{meas}} |N\rangle \\
&= \exp(i\sum_k k\phi n_k^{meas}) \sum_N \exp(-i\phi N) C_{N n_{-1}^{meas} n_1^{meas} n_2^{meas} n_4^{meas}} |N\rangle.
\end{aligned}$$

The factor $\exp(-i\sum_k k\phi n_k^{meas})$ is just an overall phase shift and can be disregarded. But in order for the equality in Equation B.9 to hold, the factor $\exp(-i\phi N)$ must be the same for each value of N . So it is necessary that $-\phi N = 2\pi M + \delta$, where M is an integer and δ is some constant offset that is independent of N . Because $\phi = \pm 2\pi/3$, we find that N is restricted to $N = 3M + 3\delta/2\pi$. Then because N must be an integer, the offset δ can only be $\delta = 2\pi J/3$, where J is some integer. That is, $N = 3M + J$. So N occurs in multiples of three, but does not necessarily start at zero. It can follow the pattern $N = 0, 3, 6, \dots$ or $N = 1, 4, 7, \dots$ or $N = 2, 5, 8, \dots$. These patterns are exactly as found in the near-exact numerical solutions of the Schrödinger equation from Chapter III.

B.3. Phase-space symmetry of conditioned phonon states

As we have just found, the conditional phonon state has the form

$$|\psi\rangle = \sum_{M=0}^{\infty} C_{J+3M} |J+3M\rangle, J = 0, 1, 2. \quad (\text{B.10})$$

This general form also describes the three-photon squeezed vacuum and three-component cat states discussed in Chapter II. The Husimi Q distribution [20] of a state that can be expressed as Equation B.10 is

$$\begin{aligned} Q(\alpha) &= \frac{1}{\pi} |\langle \alpha | \psi \rangle|^2 \quad (\text{B.11}) \\ &= \frac{1}{\pi} |\langle n | \exp(-|\alpha|^2/2) \sum_{n=0}^{\infty} \frac{\alpha^n}{\sqrt{n!}} \sum_M C_{J+3M} |J+3M\rangle|^2 \\ &= \frac{1}{\pi} |\exp(-|\alpha|^2/2) \sum_{n=0}^{\infty} \delta_{n,J+3M} \frac{\alpha^n}{\sqrt{n!}} \sum_M C_{J+3M}|^2 \\ &= \frac{1}{\pi} |\exp(-|\alpha|^2/2) \sum_{M=0}^{\infty} \frac{|\alpha|^{J+3M} \exp(i\theta)^{J+3M}}{\sqrt{(J+3M)!}} \sum_M C_{J+3M}|^2 \\ &= \frac{1}{\pi} \exp(-|\alpha|^2) \left| \sum_{M=0}^{\infty} \frac{|\alpha|^{J+3M} \exp(i(J+3M)\theta)}{\sqrt{(J+3M)!}} \sum_M C_{J+3M} \right|^2 \\ &= \frac{1}{\pi} \exp(-|\alpha|^2) |\exp(iJ\theta) \sum_{M=0}^{\infty} \frac{|\alpha|^{J+3M} \exp(i3M\theta)}{\sqrt{(J+3M)!}} \sum_M C_{J+3M}|^2 \\ &= \frac{1}{\pi} \exp(-|\alpha|^2) \left| \sum_{M=0}^{\infty} \frac{|\alpha|^{J+3M} \exp(i3M\theta)}{\sqrt{(J+3M)!}} \sum_M C_{J+3M} \right|^2, \end{aligned}$$

where $|\alpha\rangle$ is a coherent state with complex amplitude. The phase factor $\exp(i3M\theta)$ maps onto itself with any rotation of $\pm 2\pi/3$:

$$\exp(i3M(\theta \pm 2\pi/3)) = \exp(i3M\theta \pm i2\pi M) = \exp(i3M\theta). \quad (\text{B.12})$$

So the conditional phonon state (or any number state superposition of this form) maps onto itself with a rotation of $2\pi/3$ —it is threefold symmetric in phase space.

Note that as a result of this phase-space symmetry, the overall phase factor identified in Equation B.9, which is an integer multiple of $2\pi/3$, has no effect on the conditioned phonon state phase-space distribution.

Thus we have shown that the invariance of the Hamiltonian under rotation by $R(\phi)$ with $\phi = \pm 2\pi/3$ implies that the conditional phonon state is a superposition of number states that occur in multiples of three, which in turn implies that that state is threefold symmetric in phase space. More generally, we can see that if the Hamiltonian were invariant when ϕ is an integer multiple of $2\pi/k$, then the conditional phonon state would be a superposition of multiples of k and would be k -fold symmetric in phase space.

APPENDIX C

NUMERICAL METHODS

In this Appendix we give some details on the numerical methods used to obtain the results of the quantum and semiclassical simulations presented in Chapters III and IV.

C.1. Numerical methods: quantum theory

The primary numerical challenge in the quantum theory is the size of the dual-pumped Raman comb Hamiltonian when expressed in a number-state basis. With four optical modes and one phonon mode, there are five dynamical modes to be modeled. Each mode is represented in the number basis and requires $n_{max} + 1$ basis states, where n_{max} is the highest number of photons or phonons modeled in a single mode. (Then $n_{max} + 1$ basis states are required because the $|0\rangle$ basis state is necessary.) The number n_{max} limits the time and pump amplitudes that can be considered, because if there is non-negligible probability of having $n_{max} + 1$ photons or phonons in a given mode, the probability amplitudes of the state $|n_{max}\rangle$ and others will be incorrect¹. That limitation suggests that n_{max} should be as high as possible. Unfortunately the size of the Hamiltonian matrix is $(n_{max} + 1)^5 \times (n_{max} + 1)^5$. For the results presented in Chapter III, $n_{max} = 25$ and so the Hamiltonian has

¹A non-obvious consequence of the limitation on n_{max} is that not all conditioned phonon states corresponding to photon numbers between 0 and n_{max} can be modeled. As described in Chapter III, measuring the photon numbers n_{-1}, n_1, n_2, n_4 tends to produce conditioned phonon states with highest amplitudes in states near $(n_{-1} + n_2) - (n_1 + n_4)$. So the conditioned phonon states corresponding to $(n_{-1} + n_2) - (n_1 + n_4) \approx n_{max}$ are not modeled successfully, because their amplitudes in states that are higher than $|n_{max}\rangle$ may be comparable to their amplitudes in $|n_{max}\rangle$ or $|n_{max} - 3\rangle$, and so their superposition is unphysically truncated. Conditioned phonon states with this problem occur only with low probability, however, because the overall probability of $|n_{max}\rangle$ is low.

141,167,095,653,376 matrix elements. Of these, only 109,005,000 are not identically zero. The matrix elements are given by

$$\begin{aligned}
& \langle N'n'_{-1}n'_1n'_2n'_4|H|Nn_{-1}n_1n_2n_4\rangle & (C.1) \\
& = -iA_0\sqrt{N+1}\sqrt{n_{-1}+1}\delta_{N',N+1}\delta_{n'_1,n_1}\delta_{n'_2,n_2}\delta_{n'_{-1},n_{-1}+1}\delta_{n'_4,n_4} \\
& - iA_0^\dagger\sqrt{N+1}\sqrt{n_1}\delta_{N',N+1}\delta_{n'_1,n_1-1}\delta_{n'_2,n_2}\delta_{n'_{-1},n_{-1}}\delta_{n'_4,n_4} \\
& - i\sqrt{N+1}\sqrt{n_1+1}\sqrt{n_2}\delta_{N',N+1}\delta_{n'_1,n_1+1}\delta_{n'_2,n_2-1}\delta_{n'_{-1},n_{-1}}\delta_{n'_4,n_4} \\
& - iA_3\sqrt{N+1}\sqrt{n_2+1}\delta_{N',N+1}\delta_{n'_1,n_1}\delta_{n'_2,n_2+1}\delta_{n'_{-1},n_{-1}}\delta_{n'_4,n_4} \\
& - iA_3^\dagger\sqrt{N+1}\sqrt{n_4}\delta_{N',N+1}\delta_{n'_1,n_1}\delta_{n'_2,n_2}\delta_{n'_{-1},n_{-1}}\delta_{n'_4,n_4-1} \\
& + iA_0^\dagger\sqrt{N}\sqrt{n_{-1}}\delta_{N',N-1}\delta_{n'_1,n_1}\delta_{n'_2,n_2}\delta_{n'_{-1},n_{-1}-1}\delta_{n'_4,n_4} \\
& + iA_0\sqrt{N}\sqrt{n_1+1}\delta_{N',N-1}\delta_{n'_1,n_1+1}\delta_{n'_2,n_2}\delta_{n'_{-1},n_{-1}}\delta_{n'_4,n_4} \\
& + i\sqrt{N}\sqrt{n_2+1}\sqrt{n_1}\delta_{N',N-1}\delta_{n'_1,n_1-1}\delta_{n'_2,n_2+1}\delta_{n'_{-1},n_{-1}}\delta_{n'_4,n_4} \\
& + iA_3^\dagger\sqrt{N}\sqrt{n_2}\delta_{N',N-1}\delta_{n'_1,n_1}\delta_{n'_2,n_2-1}\delta_{n'_{-1},n_{-1}}\delta_{n'_4,n_4} \\
& + iA_3\sqrt{N}\sqrt{n_4+1}\delta_{N',N-1}\delta_{n'_1,n_1}\delta_{n'_2,n_2}\delta_{n'_{-1},n_{-1}}\delta_{n'_4,n_4+1}.
\end{aligned}$$

They are computed in a Fortran 90 program that loops over the unprimed values of $n_{-1,1,2,4}$ and only the primed values that are within ± 1 of the unprimed values. The outermost loop is enclosed in an OpenMP parallel loop. The computed values and their (*row, column*) indices in the 2-D Hamiltonian matrix are written to text files immediately upon computing rather than stored in a huge array. These files define the Hamiltonian as a sparse matrix.

Due to the large size of the Hamiltonian matrix, computing the matrix exponential in the time evolution operator $\exp(-iHt)$ is challenging. We use a

freely available software package called Expokit [52], which is capable of efficiently evaluating the product of that matrix exponential with a vector (in this case representing the initial condition of the state) even for large sparse matrices such as our Hamiltonian. Expokit takes advantage of the fact that the product of a matrix exponential and a vector is the analytic solution to the following ordinary differential equation:

$$\begin{aligned} \frac{dw(t)}{dt} &= Aw(t) & (C.2) \\ w(0) &= v \\ \rightarrow w(t) &= \exp(tA)v \end{aligned}$$

For large sparse matrices, Expokit uses Krylov subspace projection methods [53] to reduce the dimensionality of the problem, and then uses Padé approximations [25] to obtain the solution.

Most of the remaining computations in the quantum theory are performed in Matlab. An exception is the exact form of the conditioned phonon state Wigner distributions given in Appendix A, which are performed in Fortran 90 for increased speed. In some cases the Wigner distributions were instead calculated with fast Fourier Transforms using Matlab code adapted from [54].

C.2. Numerical methods: semiclassical theory

The semiclassical work described in Chapter IV was performed in Mathematica. The random initial conditions were created using Mathematica's *RandomReal* and *NormalDistribution* functions. The set of coupled differential equations was solved

by Mathematica's *NDSolve* function. The solutions to these equations at a given time are complex amplitudes for each of the four optical modes and for the phonon mode. Each amplitude can be represented as a single point in phase space, and so in order to obtain a full picture of the phase space behavior of the semiclassical system, the differential equations are solved 15,000 times in independent trials. The 15,000 complex amplitudes obtained for each mode can then be put together to show the histograms and phase space distributions shown in Chapter IV. We emphasize again that the stability properties of the semiclassical model are not thoroughly explored in this work.

REFERENCES CITED

- [1] H. Kimble, “The quantum internet,” *Nature*, vol. 453, pp. 1023–1030, 2008.
- [2] M. Aspelmeyer, T. Kippenberg, and F. Marquardt, “Cavity optomechanics,” *Reviews of Modern Physics*, vol. 86, no. 1391, 2014.
- [3] K. Lee, M. Sprague, B. Sussman, J. Nunn, N. Langford, X.-M. Jin, T. Champion, P. Michelberger, K. Reim, D. England, D. Jaksch, and I. Walmsley, “Entangling macroscopic diamonds at room temperature,” *Science*, vol. 334, no. 6060, 2011.
- [4] K. Lee, B. Sussman, M. Sprague, P. Michelberger, K. Reim, J. Nunn, N. Langford, P. Bustard, D. Jaksch, and I. Walmsley, “Macroscopic non-classical states and terahertz quantum processing in room-temperature diamond,” *Nature Photonics*, vol. 6, pp. 41–44, 2011.
- [5] X. Hu, *Quantum fluctuations in condensed matter systems: squeezed states in phonons and Josephson junctions*. PhD thesis, The University of Michigan, 1996.
- [6] F. Couny, F. Benabid, P. Roberts, P. Light, and M. Raymer, “Generation and photonic guidance of multi-octave optical-frequency combs,” *Science*, vol. 318, p. 1118, 2007.
- [7] J. Ye and S. Cundiff, *Femtosecond optical frequency comb technology: principle, operation, and application*. Springer, 2005.
- [8] M. Raymer and J. Mostowski, “Stimulated Raman scattering: unified treatment of spontaneous initiation and spatial propagation,” *Physical Review A*, vol. 24, no. 4, 1981.
- [9] M. Raymer and I. Walmsley, “The quantum coherence properties of stimulated Raman scattering,” *Progress in Optics*, vol. XXVIII, no. 180, 1990.
- [10] C. Wu, M. Raymer, Y. Wang, and F. Benabid, “Quantum theory of phase correlations in optical frequency combs generated by stimulated Raman scattering,” *Physical Review A*, vol. 82, no. 053834, 2010.
- [11] S. Kuo, D. Smithey, and M. Raymer, “Spatial interference of macroscopic light fields from independent Raman sources,” *Physical Review A*, vol. 43, no. 7, 1991.
- [12] Y. Wang, C. Wu, F. Couny, M. Raymer, and F. Benabid, “Quantum-fluctuation-initiated coherence in multioctave Raman optical frequency combs,” *Physical Review Letters*, vol. 105, no. 12, 2010.

- [13] M. Belsley, D. Smithey, K. Wedding, and M. Raymer, “Observation of extreme sensitivity to induced molecular coherence in stimulated Raman scattering,” *Physical Review A*, vol. 48, no. 2, 1993.
- [14] T. Suzuki, M. Hirai, and M. Katsuragawa, “Octave-spanning Raman comb with carrier envelope offset control,” *Physical Review Letters*, vol. 101, no. 24, 2008.
- [15] H.-S. Chan, Z.-M. Hsieh, W.-H. Liang, A. Kung, C.-K. Lee, C.-J. Lai, R.-P. Pan, and L.-H. Peng, “Synthesis and measurement of ultrafast waveforms from five discrete optical harmonics,” *Science*, vol. 331, no. 6021, 2011.
- [16] A. Sokolov, D. Walker, D. Yavuz, G. Yin, and S. Harris, “Raman generation by phased and antiphased molecular states,” *Physical Review Letters*, vol. 85, no. 3, 2000.
- [17] S. L. Braunstein and R. I. McLachlan, “Generalized squeezing,” *Physical Review A*, vol. 35, no. 4, 1987.
- [18] L.-A. Wu, M. Xiao, and H. Kimble, “Squeezed states of light from an optical parametric oscillator,” *Journal of the Optical Society of America B*, vol. 4, no. 10, pp. 1465–1475, 1987.
- [19] E. Wigner, “On the quantum correction for thermodynamic equilibrium,” *Physical Review*, vol. 40, p. 749, 1932.
- [20] W. Vogel and D.-G. Welsch, *Quantum Optics*. Wiley-VCH, 3rd ed., 2006.
- [21] G. Grynberg, A. Aspect, and C. Fabre, *Introduction to Quantum Optics: From the Semi-classical Approach to Quantized Light*. Cambridge University Press, 2010.
- [22] E. Polzik, J. Carri, and H. Kimble, “Spectroscopy with squeezed light,” *Physical Review Letters*, vol. 68, no. 20, pp. 3020–3023, 1992.
- [23] J. A. et al, “Enhanced sensitivity of the LIGO gravitational wave detector by using squeezed states of light,” *Nature Photonics*, vol. 7, pp. 613–619, 2013.
- [24] R. A. Fisher, M. M. Nieto, and V. D. Sandberg, “Impossibility of naively generalizing squeezed coherent states,” *Physical Review D*, vol. 29, no. 6, 1984.
- [25] J. G.A. Baker, *Essentials of Padé Approximants in Theoretical Physics*. New York: Academic Press, 1975.
- [26] G. B. Arfken and H. J. Weber, *Mathematical Methods for Physicists*. Elsevier Academic Press, sixth ed., 2005.
- [27] M. Hillery, “Photon number divergence in the quantum theory of n -photon down conversion,” *Physical Review A*, vol. 42, no. 1, 1990.

- [28] P. Elyutin and D. Klyshko, “Three-photon squeezing: exploding solutions and possible experiments,” *Physics Letters A*, vol. 149, no. 5,6, 1990.
- [29] M. Hillery, M. Zubairy, and K. Wodkiewicz, “Squeezing in higher order nonlinear optical processes,” *Physics Letters*, vol. 103A, no. 5, 1984.
- [30] K. Banaszek and P. L. Knight, “Quantum interference in three-photon down-conversion,” *Physical Review A*, vol. 55, no. 3, 1997.
- [31] M. Brune, E. Hagley, J. Dreyer, X. Maitre, A. Maali, C. Wunderlich, J. Raimond, and S. Haroche, “Observing the progressive decoherence of the “meter” in a quantum measurement,” *Physical Review Letters*, vol. 77, no. 24, 1996.
- [32] E. Schrödinger, “Die gegenwärtige situation in der quantenmechanik,” *Die Naturwissenschaften*, vol. 23, pp. 807–812; 823–828; 844–849, 1935.
- [33] D. L. et al, “Creation of a six-atom ‘Schrödinger cat’ state,” *Nature*, vol. 438, pp. 639–642, 2005.
- [34] C. Monroe, D. Meekhof, B. King, and D. Wineland, “A “Schrödinger cat” superposition state of an atom,” *Science*, vol. 272, no. 5265, pp. 1131–1136, 1996.
- [35] A. Ourjoumtsev, H. Jeong, R. Tualle-Brouri, and P. Grangier, “Generation of optical ‘Schrödinger cats’ from photon number states,” *Nature*, vol. 448, pp. 784–786, 2007.
- [36] G. K. et al, “Observation of quantum state collapse and revival due to single-photon Kerr effect,” *Nature*, vol. 495, pp. 205–209, 2013.
- [37] W. Schleich, M. Pernigo, and F. L. Kien, “Nonclassical state from two pseudoclassical states,” *Physical Review A*, vol. 44, no. 3, 1991.
- [38] R. J. Glauber, “Coherent and incoherent states of the radiation field,” *Physical Review*, vol. 131, no. 6, 1963.
- [39] A. Ourjoumtsev, R. Tualle-Brouri, J. Laurat, and P. Grangier, “Generating optical Schrödinger kittens for quantum information processing,” *Science*, vol. 312, pp. 83–86, 2006.
- [40] J. Neergaard-Nielsen, B. Nielsen, C. Hettich, K. Molmer, and E. Polzik, “Generation of a superposition of odd photon number states for quantum information networks,” *Physical Review Letters*, vol. 97, p. 083604, 2006.
- [41] K. Wakui, H. Takahashi, A. Furusawa, and M. Sasaki, “Controllable generation of highly nonclassical states from nearly pure squeezed vacua,” *Optics Express*, vol. 15, pp. 3568–3574, 2007.

- [42] V. Dodonov, I. Malkin, and V. Man'ko, "Even and odd coherent states and excitations of a singular oscillator," *Physica*, vol. 72, no. 3, pp. 597–615, 1974.
- [43] R. Jozsa, "Fidelity for mixed quantum states," *Journal of Modern Optics*, vol. 41, no. 12, 1994.
- [44] C. Hong, Z. Ou, and L. Mandel, "Measurement of subpicosecond time intervals between two photons by interference," *Physical Review Letters*, vol. 59, no. 18, pp. 2044–2046, 1987.
- [45] U. Leonhardt, J. Vaccaro, B. Bohmer, and H. Paul, "Canonical and measured phase distributions," *Physical Review A*, vol. 51, no. 84, 1995.
- [46] S. Bauerschmidt, D. Novoa, and P. S. J. Russell, "Dramatic Raman gain suppression in the vicinity of the zero dispersion point in a gas-filled hollow-core photonic crystal fiber," *Physical Review Letters*, vol. 115, no. 24, 2015.
- [47] N. Bloembergen and Y. Shen, "Coupling between vibrations and light waves in Raman laser media," *Physical Review Letters*, vol. 12, no. 18, 1964.
- [48] M. Duncan, R. Mahon, J. Reintjes, and L. Tankersley, "Parametric Raman gain suppression in D_2 and H_2 ," *Optics Letters*, vol. 11, 1986.
- [49] I. Gradshteyn and I. Ryzhik, *Table of Integrals, Series, and Products*. Academic Press, Inc., fifth ed., 1994.
- [50] E. W. Weisstein, "'Hermite Polynomial.'" From MathWorld—A Wolfram Web Resource. <http://mathworld.wolfram.com/hermitepolynomial.html>."
- [51] U. Leonhardt, *Measuring the Quantum State of Light*. Cambridge University Press, 2005.
- [52] R. B. Sidje, "EXPOKIT. A software package for computing matrix exponentials," *ACM Trans. Math. Softw.*, vol. 24, no. 1, pp. 130–156, 1998.
- [53] Y. Saad, *Iterative methods for sparse linear systems*. Society for Industrial and Applied Mathematics, 2 ed., 2003.
- [54] D. A. Steck, "Quantum and atom optics, available online at <http://steck.us/teaching> (revision 0.11.5, 27 november 2016).."